



Michigan Technological University
Create the Future Digital Commons @ Michigan Tech

Dissertations, Master's Theses and Master's
Reports - Open

Dissertations, Master's Theses and Master's
Reports

2012

Development of one-dimensional and two-dimensional computational tools that simulate steady internal condensing flows in terrestrial and zero-gravity environments

Soumya Asimkumar Mitra
Michigan Technological University

Follow this and additional works at: <https://digitalcommons.mtu.edu/etds>

 Part of the [Mechanical Engineering Commons](#)

Copyright 2012 Soumya Asimkumar Mitra

Recommended Citation

Mitra, Soumya Asimkumar, "Development of one-dimensional and two-dimensional computational tools that simulate steady internal condensing flows in terrestrial and zero-gravity environments", Dissertation, Michigan Technological University, 2012.
<https://doi.org/10.37099/mtu.dc.etds/387>

Follow this and additional works at: <https://digitalcommons.mtu.edu/etds>

 Part of the [Mechanical Engineering Commons](#)

DEVELOPMENT OF ONE-DIMENSIONAL AND TWO-DIMENSIONAL
COMPUTATIONAL TOOLS THAT SIMULATE STEADY INTERNAL
CONDENSING FLOWS IN TERRESTRIAL AND ZERO-GRAVITY
ENVIRONMENTS

By

Soumya Asimkumar Mitra

A DISSERTATION

Submitted in partial fulfillment of the requirements for the degree of

DOCTOR OF PHILOSOPHY

(Mechanical Engineering-Engineering Mechanics)

MICHIGAN TECHNOLOGICAL UNIVERSITY

2012

Copyright © 2012 by Soumya Mitra

This dissertation, “Development of one-dimensional and two-dimensional computational tools that simulate steady internal condensing flows in terrestrial and zero-gravity environments,” is hereby approved in partial fulfillment of the requirements for the Degree of DOCTOR OF PHILOSOPHY IN MECHANICAL ENGINEERING-ENGINEERING MECHANICS.

Department of Mechanical Engineering-Engineering Mechanics

Signatures:

Dissertation Advisor

Dr. Amitabh Narain

Committee Member

Dr. Jeffrey Allen

Committee Member

Dr. Fernando Ponta

Committee Member

Dr. Ranjit Pati

Department Chair

Dr. William W. Predebon

Date

“To my parents”

Table of Contents

List of Figures	6
List of Tables	9
Preface.....	10
Acknowledgement	11
Nomenclature	13
Abstract	16
1. Condensing Flow Research Issues and Investigative Tools.....	18
1.1 Introduction	18
1.2 Other Research Issues	23
1.3 Background Literature	25
1.4 Development of Computational Tools	26
1.5 Need for the New Tools	29
2 Mathematical Model for Steady Internal Condensing Flows.....	32
2.1 Full Two Dimensional Condensing Flow Governing Equations	36
2.1.1 Interior Equations.....	36
2.1.2 Interface Conditions.....	36
2.1.3 Boundary Conditions	38
2.2 Quasi One Dimensional (1-D) Governing Equations	40
3 Computational Methodology.....	45
3.1 Two-Dimensional Computational Algorithm	45
3.2 One-dimensional Solution Technique	50
4. Results and Discussion.....	56
4.1 Accuracy of Computational Tools	56
4.1.1 Accuracy of the Two-Dimensional Computational Tool.....	56
4.1.2 Accuracy of the One-Dimensional Computational Tool	62
4.2 Validation of the Computational Tools and Synthesis of Experimental Results with Results Obtained from the Computational Tools	67
4.2.1. Comparisons of Experimental Results with Computationally Obtained Results for Gravity Dominated Condensing Flows in a Vertical Tube and an Inclined Channels.....	67
4.2.2 Comparisons of Experimental Results with Computationally Obtained Results for Shear Driven Condensing Flows in a Horizontal Channel	83

4.3 Differences between Gravity Driven and Shear Driven Condensing Flows	90
4.4 The 1-D approach's ability to handle different condensing-surface thermal boundary conditions for different methods of cooling	94
4.5 Similarity and differences in shear driven flows (0g and transverse gravity) and gravity driven flows, with an assessment of their impact on the investigation of length of annularity	97
4.5.1 Similarity and differences between 0g and transverse gravity	97
4.5.2 Investigation for estimating the length of annular regime	99
4.5.3 Impact of inclination on condensing flow in tilted channels	105
5. Computational results that define the transition zone between entirely gravity driven and entirely shear/pressure driven annular/stratified condensing flows	110
5.1 Summarized Correlations	123
6. Computational results for condensing flows in micrometer scale ducts	125
7. Conclusions and future research.....	130
7.1 Conclusions	130
7.3 Aiding thermal system development	133
References.....	134
Appendix A1 - Definition of coefficients for 1-D internal condensing flow	138
Appendix A.2 – Copyright Permission.....	141
Appendix A.3	145

List of Figures

Figure 2.1: A schematic of a representation of internal condensing flow problem in a channel.	33
Figure 2.2: A schematic describing a representative internal condensing flow problem in a vertical tube.	34
Figure 2.3: With the help of a representative film profile, the figure shows the boundary conditions for the liquid and the vapor domains present in an internal condensing flow.	39
Figure 4.1: Sample convergence plot of interfacial mass-flux terms for a representative internal condensing flow problem.	57
Figure 4.2: (a) For a flow of FC-72 in a vertical channel, the figure shows the cross-sectional condensate velocity profile, $u_1(x,y)$ at $x = 0.06$ m for different refinement levels of the mesh. (b) For a flow of FC-72 in a vertical channel, the figure shows the cross-sectional vapor velocity profile, $u_2(x,y)$ at $x = 0.06$ m for different refinement levels of the mesh.	61
Figure 4.3: For different refinement levels chosen for the vapor domain meshing, the figure shows film thickness profiles obtained from the solution of the complete condensing flow problem.	62
Figure 4.4: The figure compares steady/quasi-steady solutions for a vertical channel. The solutions are obtained by 2-D (FORTRAN code as well as COMSOL/MATLAB platform based code) and 1-D techniques for the flow of R-113 vapor with inlet speed of $U = 0.41$ m/s, $\Delta T = 5$ °C, $h = 0.004$ m, and $g_x = 9.8$ m/s ²	64
Figure 4.5: The figure compares steady/quasi-steady solutions obtained by 2-D (FORTRAN code as well as COMSOL/MATLAB platform based code) and 1-D techniques for a channel under 0g conditions.	65
Figure 4.6: The figure compares steady/quasi-steady solutions obtained by 2-D (FORTRAN code) and 1-D techniques for a flow through a vertical cylinder. ...	66
Figure 4.7: (a) The photograph of a condenser test-section. (b) The test-section schematic (diameters in (a) and (b) are not to the same scale). The condensing surface covers the zone $x_0 \leq x \leq x_{10}$	69
Figure 4.8: The schematic of the flow loop for achieving steady flows for partial or full condensation cases.	70
Figure 4.9: The comparison of theoretically and computationally obtained values of x_{FC} as a function of M_{in} . Here the dashed lines indicate the simulation results and the solid lines indicate the experimental results.	75
Figure 4.10: The comparison of theoretically and computationally obtained values of x_{FC} as a function of ΔT	76
Figure 4.11: Comparison of experimentally and computationally obtained values of average heat transfer coefficients for fully condensing flows.	77
Figure 4.12: The figure graphically presents the nature of agreement between theoretically and experimentally Lu et al. 1995 obtained values of average heat-transfer coefficient.	82
Figure 4.13: Side views of: (a) test-section, and (b) instrumented condensing plate	84
Figure 4.14: Condensing-surface temperature T_w versus distance x for case # 4 in Table 4.5.	86

Figure 4.15: Liquid film thickness $\Delta(x)$ versus x for case # 4 in Table 4.5.	87
Figure 4.16: Condensing-surface heat-flux q''_w variations with x for case # 4 in Table 4.5.	88
Figure 4.17: Cross-sectional liquid mass flow rate \dot{M}_L and the vapor mass flow rate \dot{M}_V for case # 4 in Table 4.5.	89
Figure 4.18: Figure shows film thickness versus x variation and the y -variations of the x -component of the velocity profile (at $x = 20$) for gravity driven 1g and shear driven 0g flows inside a tube.	91
Figure 4.19: For the cases shown in Fig. 4.18, this figure shows the non-dimensional interfacial pressure variations with downstream distance.	92
Figure 4.20: For a flow of FC-72 vapor inside a vertical tube condenser with average inlet speed $U = 7$ m/s, diameter $D = 0.002$ m, the figure shows the profiles of (i) vapor to condensing-surface temperature variations (curve A), and (ii) condensing-surface heat-flux variations (curve B).....	95
Figure 4.21: For the cases shown in Fig. 4.20, the non-dimensional film thickness profile predictions resulting from the solutions of the problems for variable wall temperature difference (curve A) and variable heat flux profile (curve B) as prescriptions for condensing-surface thermal boundary condition.....	96
Figure 4.22: Film thickness comparisons for shear driven flows in the presence ($gy = -9.81$ m/s ²) and the absence ($gy = 0$ m/s ²) of transverse gravity.....	98
Figure 4.23: The figure shows the pressure variation at $x = 0.15$ m for a flow as in Fig. 4.22, in the presence ($gy = -9.81$ m/s ²) and the absence ($gy = 0$ m/s ²) of transverse gravity.	99
Figure 4.24: For the flow of FC72 vapor in a horizontal channel with channel height = 2 mm, the figure shows the film thickness and condensate interfacial velocity along the length of the condenser. The case is simulated for inlet mass flow rate = 0.4 g/s and $\Delta T = 17.45$ °C.....	102
Figure 4.25: For the flow in Fig. 4.24, the figure shows interfacial stress on the interface along the length of the condenser.	103
Figure 4.26: The figure shows pressure gradient along the length of the condenser.....	104
Figure 4.27: Streamline plot of velocity magnitude for the flow in Fig. 4.24.	105
Figure 4.28: Figure shows comparisons of film thickness for a horizontal channel flow and a channel with 2° inclination. The flow condition is same as that of Fig. 4.24.	106
Figure 4.29: Figure shows comparisons of condensate interfacial velocity for a horizontal channel flow and a channel with 2° inclination. The flow condition is same as that of Fig. 4.24.	107
Figure 4.30: Streamline of velocity magnitude for a channel with 2° inclination.	109
Figure 5.1: Figure shows the variation in film thickness ratio $(\delta(x^\#)/\delta_{ps}(x^\#))$ and $(\delta_{Nu}(x^\#)/\delta_{ps}(x^\#))$ at $x^\# = 80$ with variations in G_p . The solutions are obtained for flow of FC-72 vapor with inlet speed of $U = 0.7$ m/s, $\Delta T = 7.5^\circ\text{C}$, and diameter $D = 6.6$ mm.	112
Figure 5.2: The figure yields a division of (x, Re_{in}, G_p) space that marks a gravity dominated zone, a shear dominated zone, and a transition zone between them. The	

flow of FC-72 vapor inside the tube has $Ja/Pr_1 = 0.004$, $(\rho_2/\rho_1) = 0.0148$ and $(\mu_2/\mu_1) = 0.0241$	113
Figure 5.3: The figure shows the 4 % rule and a distance x^* by which the flows are categorized with respect to the pure shear (0g) film thickness profile $\delta_{ps}(x)$	116
Figure 5.4: The figure shows the 4 % rule and a distance x^{**} by which the flows are categorized with respect to gravity dominated film thickness profile $\delta_{Nu}(x)$	117
Figure 5.5: The figure is a projection of Fig. 5.2 in $(Re_{in} - G_p)$ plane and it also marks a gravity dominated zone, a shear dominated zone, and a transition zone between them.....	118
Figure 5.6: The figure suggests the boundaries in $(Ja/Pr_1, Re_{in}, G_p)$ space that marks a gravity dominated zone, a shear dominated zone, and a transition zones between them. The flow of FC-72 vapor has $(\rho_2/\rho_1) = 0.0148$ and $(\mu_2/\mu_1) = 0.0241$	122
Figure 5.7: The figure is a projection of Fig. 5.6 in $(Re_{in} - G_p)$ plane.....	122
Figure 6.1: For the same inlet speed U and gravity (g_x) , as tube diameter $D \rightarrow 0$, the parameter Re_{in} and G_p vary along the representative curve C . The curve C intersects zone B of Fig. 5.5 when a certain diameter D_{cr} is reached.	125
Figure 6.2: For the flow of FC-72 vapor with $U = 3$ m/s and $\Delta T = 3$ °C, the figure shows solutions for 1g and 0g cases for diameter $D_1 = 2$ mm and $D_2 = 0.2$ mm. For $D_1 > D_{cr}$ (≈ 0.3 mm), the figure shows two distinct solutions for 1g and 0g cases. For $D_2 < D_{cr}$ (≈ 0.3 mm), the solutions for both 1g and 0g cases are seen to have become nearly identical.	126
Figure 6.3: As the tube diameter becomes sub mm- to μ m-scale, the figure shows (for the FC-72 flow in Fig. 6.2) a significant rise in pressure drop ($\Delta P = P_{in} - P_{exit}$) across the condenser. The pressure drop also increases with increase in inlet mass flow rates M_{in}	127

List of Tables

Table 1.1: Summary of the problems solved using the three computational tools and a list of current and former doctoral students responsible for their development.....	29
Table 4.1: Grid quality statistics for different refinement levels for liquid and vapor domain.....	60
Table 4.2: Representative experimentally measured data Kurita et al. 2011 and some key calculated and computed variables for natural fully condensing steady flows.....	71
Table 4.3: Comparison of experimental results of Lu et al. 1995 for FC-72 vapor with computationally obtained results for an inclined channel with 1° inclination.....	81
Table 4.4: Comparison of experimental results of Lu et al. 1995 for R113 vapor with computationally obtained results for an inclined channel with 1° inclination.....	82
Table 4.5: Representative experimental runs for annular condensation.....	90

Preface

This dissertation titled “Development of one-dimensional and two-dimensional computational tools that simulate steady internal condensing flows in terrestrial and zero-gravity environments,” presents the computational predictive capabilities (computational tools) developed for the dissertation as well as key simulation results. A one-dimensional (1-D) engineering tool and a two-dimensional (2-D) scientific tool were developed. The equations, computational approach, and the results obtained from the one-dimensional tool along with the transition maps were developed by me and my advisor Dr. Amitabh Narain with contributions from R. R. Naik, S. D. Kulkarni and have been presented in Mitra et al. 2009; Mitra et al. 2011. Parts of these papers have been reproduced in Chapters 2 - 6 with the kind permission from Elsevier. The one-dimensional tool, being computationally efficient and reasonably accurate, has been extensively used to compare and synthesize with experimental results in vertical tubes Kurita et al. 2011 and horizontal channels Kivisalu et al. 2011. These comparisons with the 1-D tool are reproduced in Chapter 4 with the kind permission from Elsevier to demonstrate the validity of the tool.

The accurate 2-D numerical simulations tool that has been developed here is based on the algorithm used for the earlier simulation tool implemented on FORTRAN Liang et al. 2004; Narain et al. 2004. The new simulation tool uses commercial software ‘COMSOL MULTIPHYSICS’ to solve the single phase domains and uses MATLAB for implementing and improving the algorithm developed to solve the interface equations. The two dimensional steady tool has been developed by me, my advisor, Dr. Amitabh Narain and fellow graduate student R. R. Naik and is presented in Mitra et al. 2011. Parts of this paper have been reproduced in Chapters 2 and 3. The permissions to republish the contents of the published papers have been acquired (see Appendix A2). The Appendix A3 is included in this dissertation from Narain et al. 2004 for the ease of understanding. This section is quoted from the Appendix of the paper as the same definitions apply to this theory as well.

Acknowledgement

I would like to thank my advisor, Prof. Amitabh Narain for his engagement and guidance towards completing the research reported in this dissertation. I would like to express my sincere gratitude to him for the countless hours he has devoted towards guiding me and the research group towards proper understanding of the subject. His technical knowledge and experience has been pivotal in the development of the two computational tools and the interpretation of the results. I also want to thank him for the encouragement he has shown towards pursuit of practical training and hands-on experience through constant interactions with the experimental team. I have learnt many things through various discussions with him which will help me grow professionally and as a person.

I would like to express my gratitude to my committee members, Dr. Jeffrey Allen, Dr. Ponta, and Dr. Pati for their advice and support throughout my research.

I would also like to thank Shantanu Kulkarni, for sharing his valuable experience with the FORTRAN code, and guiding me with different aspects of the reported research. I am also thankful to Ranjeeth Naik. In our group, his enthusiasm and aptitude for coding has no parallel. The long interactions, discussions and code writing sessions were enjoyable because of the above friends and mentors. I would also like to thank the experimental team of Michael Kivisalu, Jorge Kurita, Nook Gorgitrattanagul, and Andrew Rice for their inputs and assistance in editing several research documents that we produced over years.

I especially thank my parents. Their sacrifice, motivation, unconditional love and care have inspired me to pursue this degree. I would also like to thank my wife, Madhura, for her

love and understanding. My parents and Madhura have always supported me in good times and bad. They have given me the energy and drive that is invariably needed to overcome difficult times as well as for sharing the joy of success. This work would have been impossible without my family's support.

I would also like to thank my friends who made my life inside and outside the school very enjoyable. It is impossible to thank all of them here, however, they know that I owe them a big 'thank you.' Anand, Shantanu, Gayatri, Vikram, Akshay, Aniket, Aditya Utturkar, Aditya Kulkarni, Animish, Nikhil, Maanas, Nachiket, and Sameer have always been there for me.

I would also like to thank Michigan Technological University and my advisor for financially supporting me during my research. I would also like to extend a warm thanks to all the friends who have made Houghton a second home.

Soumya Mitra

Nomenclature

Δp	$p_{in} - p_{exit}$, kPa
ΔT	$T_{sat}(p) - \bar{T}_w$, °C
ζ	Non-dimensional pressure gradient $d\pi/dx$
θ	Non-dimensional temperature
μ_1	Viscosity of liquid, kg/(m-s)
μ_2	Viscosity of vapor, kg/(m-s)
π_e	Non-dimensional exit pressure
ρ_1	Density of liquid, kg/m ³
ρ_2	Density of vapor, kg/m ³
Δ	Physical value of condensate thickness, m
δ	Non-dimensional value of condensate thickness
C_{p1}	Specific heat of the liquid condensate, J/(kg-K)
D	Inner diameter of tubular test-section, m
Fr_x	Froude number $U^2/g_x L_c$
Fr_y	Froude number $U^2/g_y L_c$
h	Channel gap, m
Ja	Condensate liquid Jakob number, $C_{p1} \cdot \Delta T / h_{fg}(p_{in})$
k_1	Conductivity of condensate liquid, W/(m-K)
L	Length of the test-section, m
L_C	Characteristic length, $L_C = D$ (diameter) for tubes and $L_C = h$ (gap height) for channels, m

\dot{M}_{in}	Vapor flow rate at test-section inlet, g/s or kg/s
\dot{M}_L	Liquid flow rate at test-section exit, g/s or kg/s
p_{exit}	Pressure at the test-section exit, kPa
p_{in}	Pressure at the test-section inlet, kPa
Pr_1	Condensate liquid Prandtl number, $\mu_1 \cdot C_{p1} / k_1$
\dot{Q}_{total}	Net heat rate out of the test-section, W
Re_{in}	Inlet vapor Reynolds number, $\rho_2 U L_c / \mu_2$
\bar{T}_w	Mean condensing surface temperature, °C
t	Non-dimensional time
t	Physical time, s
$T_{sat}(p)$	Saturation temperature at pressure p , °C
U	Average inlet vapor velocity in the x-direction, m/s
u_f	Non-dimensional interfacial velocity in the x-direction
u_l	Physical velocity in the x-direction, m/s
v	Non-dimensional velocity in the y-direction
v_l	Physical velocity in the y-direction, m/s
x_{FC}	Non-dimensional x_{FC} .
x, y	Physical distances along and perpendicular to the condensing surface, m
x_{FC}	Approximate length needed for full condensation (estimated by computations), m.
x, y	Non-dimensional distances along and perpendicular to the condensing surface

Subscripts

comp	Obtained from computations
E	Test-section exit
Expt	Obtained from experiments
I	I = 1 for liquid and I = 2 for vapor
in	Test-section inlet
Na	Natural exit condition
Nu	Nusselt solution
ps	Pure shear case

Abstract

This dissertation presents an effective quasi one-dimensional (1-D) computational simulation tool and a full two-dimensional (2-D) computational simulation methodology for steady annular/stratified internal condensing flows of pure vapor. These simulation tools are used to investigate internal condensing flows in both gravity as well as shear driven environments. Through accurate numerical simulations of the full two dimensional governing equations, results for laminar/laminar condensing flows inside mm-scale ducts are presented. The methodology has been developed using MATLAB/COMSOL platform and is currently capable of simulating film-wise condensation for steady (and unsteady flows). Moreover, a novel 1-D solution technique, capable of simulating condensing flows inside rectangular and circular ducts with different thermal boundary conditions is also presented.

The results obtained from the 2-D scientific tool and 1-D engineering tool, are validated and synthesized with experimental results for gravity dominated flows inside vertical tube and inclined channel; and, also, for shear/pressure driven flows inside horizontal channels. Furthermore, these simulation tools are employed to demonstrate key differences of physics between gravity dominated and shear/pressure driven flows. A transition map that distinguishes shear driven, gravity driven, and “mixed” driven flow zones within the non-dimensional parameter space that govern these duct flows is presented along with the film thickness and heat transfer correlations that are valid in these zones. It has also been shown that internal condensing flows in a micro-meter scale duct experiences shear driven flow, even in different gravitational environments.

The full 2-D steady computational tool has been employed to investigate the length of annularity. The result for a shear driven flow in a horizontal channel shows that in absence of any noise or pressure fluctuation at the inlet, the onset of non-annularity is partly due to insufficient shear at the liquid-vapor interface. This result is being further corroborated/investigated by R. R. Naik with the help of the unsteady simulation tool. The condensing flow results and flow physics understanding developed through these simulation tools will be instrumental in reliable design of modern micro-scale and space-based thermal systems.

1. Condensing Flow Research Issues and Investigative Tools

1.1 Introduction

For high power electronic cooling needs, and other thermal management systems (ground based micro-scale or space/aircraft based applications), the authors in Lasance et al. 2005; Wilson 2009 compare various available technologies with potential for meeting the high heat flux removal requirements. Among the available technologies, they conclude that the use of phase-change flows (flow boiling and flow condensation) has the best potential. It is a well-known fact that the vapor compression cycle and Rankine cycle exploit phase-change heat transfer in the flow boiler and flow condenser that play a pivotal role in their respective closed flow loop. Reliable design and effective integration of condensers/boilers in the traditional macro-scale as well as in modern micro-scale, or space-based thermal systems require good *flow prediction capabilities* and proper *flow control strategies*.

The research group at Michigan Technological University, under the guidance of Prof. Amitabh Narain, has extensively studied, through experiments Narain et al. 2007; Kurita et al. 2011(Kurita et al. 2011; Narain et al. 2007; Narain et al. 2009; Kivisalu et al. 2011), and computations (Kulkarni et al. 2010; Mitra et al. 2011; Liang et al. 2004; Narain et al. 2004; Phan et al. 2007), flow condensation for reliable and effective operations of these modern thermal systems. Recent investigations in A. Narain et al. 2012 have given new insights and quantitative results that would lead to effective shear/pressure driven operations of a flow boiler as well. However, the investigations undertaken for this dissertation focuses on flow condensation.

For this dissertation, the internal condensing flows are classified into ‘gravity dominated or driven flows’ and ‘shear/pressure driven flows’ based on the forces primarily responsible for the flow of condensate. The condensing flow, in the traditional macro-scale thermal systems that employ condensers in the vertical or inclined orientation, is assisted by gravity. In fact, large-scale horizontal condensers are also significantly assisted by gravity if the inlet vapor flow rate is not large as to make the flow perfectly annular. Hence, most of the macro-scale flows in terrestrial applications are termed ‘*gravity dominated or gravity driven flows*’. However, the condensing flows, in modern micro-scale systems, zero gravity applications, and certain horizontal channel flow condensers, are driven by the pressure difference across the condenser or the interfacial shear forces on the condensate. Hence, these flows are termed ‘*shear/pressure driven flows*.’

The authors in Lasance et al. 2005 and Wilson 2009 highlight issues of non-repeatability and unpredictable behavior with regard to the micro-scale phase-change thermal systems. For an effective integration of condensers in micro-scale thermal systems one has to overcome difficulties in *attaining* and *maintaining* shear/pressure driven quasi-steady condensing flows with repeatable performance. They also emphasize on the need to design a new system that must deviate from traditional (air-conditioners, refrigerators, etc.) macro-scale two-phase system designs to fully exploit the potential of pumped two-phase flow systems. Even though use of these active pumping strategies in a two-phase system is necessary, they induce undesirable flow transients. In the absence of the development of flow control strategies and predictive tools, new designs may

continue to suffer from *non-repeatable* and *unpredictable* performances at enormous research and development (R & D) costs to the sponsors of the new system design.

Therefore, there is a need to investigate issues pertaining to attainability and fluctuation sensitivity (reported in Kivisalu et al. 2011) of steady/quasi-steady flows in different flow regimes such as, annular/stratified, plug/slug, bubbly, misty, etc. Among these regimes, particular interest is in understanding the difference between attainability and controllability of annular/stratified (or film wise condensation) flows under gravity or shear driven conditions. These annular/stratified flows have high thermal efficiencies compared to the other non-annular regimes that are possible. Hence, in this dissertation, these annular flows are rigorously studied (i.e. by a synthesis of computations and experiments): (i) to develop predictive abilities, (ii) to understand the difference between shear and gravity driven flows, (iii) to demarcate a general non-dimensional parameter space into zones based on where shear/pressure or gravitational forces are the dominant driving force, and (iv) to investigate the length of annular zone of shear/pressure driven internal condensing flows.

For shear or gravity driven annular/stratified internal partially condensing flows with a given inlet vapor mass flow rate and a known vapor to wall temperature difference, our earlier established computational and experimental results (Narain et al. 2009; Narain et al. 2004; Narain et al. 2007; Phan et al. 2006) have been corrected (also see Kurita et al. 2011; Mitra et al. 2011; Kivisalu et al. 2011) to state that there exists a *unique* annular/stratified steady solution and a unique steady exit condition of the strictly steady equations. The multiple quasi-steady computational solutions that were reported to exist in (Narain et al. 2009; Narain et al. 2004; Narain et al. 2007; Phan et al. 2006) were

erroneous and in a revised understanding of these experimental situations shown in Kivisalu et al. 2011, they arise from flows which exhibit “boundary condition sensitivity.” As far as computational solutions are concerned, the steady, or low amplitude quasi-steady solutions, are unique. Here and henceforth, the unique steady solutions for the steady “parabolic” boundary conditions, namely, the steady *inlet* conditions (vapor mass flow rate, pressure, and temperature) and thermal boundary condition for the condensing-surface (i.e. known uniform or non-uniform spatial variations for the condensing surface’s temperature or heat-flux values) are termed “*natural*” solutions. The value of an appropriate exit parameter (exit pressure, or exit liquid mass flow rate, or exit vapor mass flow rate) obtained from the “natural” solution is termed “natural” exit condition for the flow.

To enhance the predictive abilities towards better understanding of the condensing flows, a new one-dimensional (1-D) computational tool (Mitra et al. 2011; Mitra et al. 2009) and the new two-dimensional (2-D) computational tool (Mitra et al. 2011) have been developed and are presented here. Firstly, the governing equations, computational approach, accuracy and validation of the computational tools are presented. The results obtained from the computational tools are compared and synthesized with the experimental results obtained for (i) gravity driven flows inside vertical tube Kurita et al. 2011 and inclined channel experiments of Lu et al. 1995; and (ii) shear/pressure driven condensing flows inside a horizontal channel reported in Kivisalu et al. 2011 and Nook 2011. Thereafter, these tools are employed to better understand and characterize the “natural” gravity dominated and shear/pressure driven flows.

Key differences between purely shear driven and gravity dominated (and driven)

annular flows inside tubes and channels are presented in this dissertation. A map that partitions the parameter space (for annular/stratified flows) into strongly gravity driven, shear driven, and “mixed” driven regions is also presented here. Using this synthesis usable correlations and flow regime maps have been developed and presented here. It is also shown that shear driven cases occur in horizontal channels, 0g and - as shown here - in μm scale ducts in terrestrial environments.

The 1-D computational methodology presented here has an ability to find “natural” solutions for uniform or non-uniform prescriptions for temperature or heat flux boundary conditions for the condensing-surface. This capability is very useful in solving conjugate heat transfer problems involving condensers.

The full 2-D steady computational tool developed here is employed to extensively investigate shear/pressure driven condensing flows inside a channel. Similarities and differences between shear/pressure driven flows with presence and absence of transverse gravity is presented here. Detailed investigation of the length of annularity for shear/pressure driven flows is also presented. It is shown that in the aft portions of the flow, the interfacial viscous force per unit volume and pressure force per unit volume, which are responsible for driving these flows become smaller. Hence, the flows become extremely susceptible to ever-present noise which breaks the annularity of these flows. Since, the frontal portion of the thin annular regime has high thermal efficiency compared to other flow morphologies observed for shear/pressure driven flows, it is important to predict the length of annularity for a given operating condition and to devise condenser operation that can exploit this fact.

It has been shown through condensing flow experiments (Kivisalu et al. 2011) in a horizontal channel that the flows are extremely sensitive to pressure and mass flow rate fluctuations at the inlet of the condenser. It has also been shown in Kivisalu et al. 2011 that by suitably controlling these fluctuations the heat transfer can be enhanced significantly ($> 300\%$).

The solutions of the unsteady governing equations – both for gravity dominated and shear dominated flow zones are important in understanding various issues of the flows' sensitivities and insensitivities, to noise and fluctuations at the condenser's boundary. The steady results presented here facilitate ongoing investigations.

The development of the new computational tools have led to better understanding of the condensing flow physics, and, also, it has provided a platform for further enhancements in the simulation capabilities (e.g., compressibility effects investigations, non-annular regime investigations, etc.)

1.2 Other Research Issues:

Flow Sensitivity of Shear Driven Flow

A fundamental experimental investigation of a shear/pressure driven internal condensing flow's quasi-steady pressure-difference sensitivity to the amplitude and frequency of pressure fluctuations (and flow pulsations) at the inlet of the condenser is presented in Kivisalu et al. 2011, and Kivisalu et al. 2011. Inadvertently or deliberately, such imposed fluctuations frequently occur in closed flow loops in which the condensing flow is primarily shear driven and devices like turbines or reciprocating compressors introduce significant pressure pulsations to the vapor supplied to the condenser. For the

fluctuation case reported in Kivisalu et al. 2011, pressure pulsations of the order of 100 Pa induce large pulsations in the inlet mass flow rates. Therefore the analysis of the fluctuation sensitivity is important to a meaningful assessment of such a shear driven condenser's performance in any closed flow loop facility. Comparison of the heat-flux measurements at certain representative location in the condensing flow show (in Kivisalu et al. 2011), for different levels of inlet pressure/mass flow rate fluctuations (frequencies and amplitude), heat flux enhancements of around 300% is achieved. To simulate the impact of inlet mass flow rate and pressure fluctuations, a very robust and versatile computational tool is needed. The 2-D computational tool developed for the dissertation facilitates the successful completion of such unsteady flow situations.

Annular Flow Boiling

Nucleate boiling is often desirable for enhancing heat-transfer in the presence of gravity (in the direction of the flow or the transverse direction). Because of the presence of transverse gravity, nucleate boiling continues to enhance heat-transfer in the mm-scale experiments (with relatively low interfacial shear) reported here. However, nucleate boiling is not desirable in the absence of buoyancy – as in space applications or micro-scale device applications (where interfacial shear values are very high). This is because absence of buoyancy is not conducive to vapor bubble detachment and leads to complex flow regimes that degrade heat transfer and/or cause device and system level instabilities.

Therefore, experiments reported in A. Narain et al. 2012 were conducted (by M. Kivisalu and Nook G.) on a horizontal channel to achieve annular mode of flow boiling by using suitable techniques. This is to see if, by this method one can suppress nucleate

boiling in favor of predominantly annular boiling in which heat is conducted across a thin film (as in the annular condensation).

The experiments in Kivisalu et al. 2011 deal with flow condensation of FC-72 in a 2 mm gap horizontal channel of 1 m length and flow boiling of FC-72 in a 1.6 mm gap horizontal channel of 0.74 m length. For both boiling and condensing flow experiments, annularity of the respective flows is ensured by choice of an appropriate rate of *through flow* of vapor that does not actively participate in phase-change and has a flow rate which lies within a well defined range. The *through flow* of vapor is shown to ensure stability, annularity (by effectively suppressing nucleation in the case of flow boiling), and predictability. This fact is demonstrated by relevant flow visualization videos whose schematic and still pictures are also shown in Kivisalu et al. 2011. The 1-D condensing flow tool developed here is a key engineering tool that has been successfully implemented for the flow boiling situation as well.

1.3 Background Literature

Relevant background knowledge for the general area of condensing flows can be roughly categorized as: (i) excellent available knowledge with regard to exact and approximate model equations for the flows and conditions at the interface (Delhay 1974; Carey 2008, etc.); (ii) classical solutions for *external* film condensation flows over vertical, horizontal, and inclined walls (Nusselt 1916; Sparrow et al. 1959; Koh 1962; etc.) and their subsequent modifications and extensions (Rohsenow 1956; Chen 1961, etc.); (iii) experimental data and correlation for heat transfer rates for the various *external* condensing flow regimes (Labuntsov 1957, etc.) as well as *internal* condensing flow

regimes (Carpenter et al. 1951; Cavallini et al. 2003; Shah 1979, etc.); (iv) flow regime maps for internal condensing flows (Carey 2008, etc.); (v) analytical, semi-empirical, and theoretical studies for internal condensing flows (Shekrila.I et al. 1973; Narain 1996, etc.); (vi) relevant experimental and integral-analysis based investigations of a special category of complete condensation flows with transients and flow oscillations (Wedekind et al. 1989; Wedekind et al. 1989, etc.); (vii) relevant results on shear driven flows (Rose 1998; Schlichting et al. 2000), and (viii) relevant experiemtnal results for gravity driven external Nusselt problem (Incropera et al. 2002).

1.4 Development of Computational Tools

For better understanding of the issues related to phase-change flows of condensation and boiling, two new computational tools were developed. A new one-dimensional (1-D) computational tool and a new version of an earlier two-dimensional (2-D) computational tool has been implemented on the COMSOL/MATLAB platform. Therefore, there are three computational tools available to simulate condensing flow problems.

1. Full 2-D CFD steady/unsteady scientific tool implemented on FORTRAN platform. This code is 100 % home grown and has lower computational sophistication with respect to the commercially available single phase CFD simulation tools.
2. Full 2-D CFD steady/unsteady scientific tool implemented on COMSOL/MATLAB platform. This tool implemented here exploits the commercially available (COMSOL) single phase simulation capabilities and couples it with algorithm and data manipulations performed on MATLAB.
3. Quasi 1-D steady engineering tool.

Full 2-D CFD steady/unsteady scientific tool implemented on FORTRAN platform

The full 2-D CFD scientific tool on the FORTRAN platform was earlier developed and some of its results for gravity driven flows have been validated by comparison with condensing flow experiments. The tool has already been used to simulate internal and external, steady and unsteady condensing flow problems (see, Narain et al. 2007; Narain et al. 2008). The computational methodology has also been used to investigate classical analytical solutions for vertical (see Phan et al. 2007) and horizontal condensing flow situations (see Kulkarni et al. 2010). Table 1.1 outlines the problems solved and students responsible for the development of the tool's capabilities. Yet this tool was deemed inadequate for shear driven flows because it lacked the sophistication and accuracy needed for some fine meshing and resolution of the interface.

Full 2-D CFD steady/unsteady scientific tool implemented on COMSOL/MATLAB platform

Due to limitations in the earlier 2-D code implemented on FORTRAN, a new 2-D computational tool has been developed. The computational tool presented in this paper has been developed by implementing the well tested algorithm (see Narain et al. 2004) for solving two-phase condensing flow problems (see Table 1.1) as an iterative scheme (using COMSOL and subroutines written in MATLAB) based on modeling the flow as “sharp interface problem.” Accurate numerical solutions of the full governing equations are presented here for steady and unsteady laminar/laminar film condensation flows

inside a channel. This computational tool can be directly used to investigate the issues of annular/stratified condensing flows' heat transfer rates, flow realizability, stability, noise sensitivity, and boundary condition sensitivity.

Quasi 1-D steady engineering tool

The 1-D tool, though more approximate, is computationally more efficient and versatile over a larger parameter zone. It has been developed as an independent tool as well as a tool that supports and improves the efficacy of the associated 2-D approaches. This new “quasi” 1-D technique presented and implemented here is different from the other 1-D tools (Dobran et al. 1980; Narain 1996; Chen et al. 2009, etc.) that are available in the literature. This 1-D tool avoids the use of average flow variables and/or empirical models (such as friction factor models for the interface, pressure gradient models, etc) used in Dobran et al. 1980; Narain 1996; Chen et al. 2009 by keeping the method close to the exact solution technique for laminar vapor and laminar liquid flows (with smooth or nearly smooth wavy interface). Because of the absence of empirical/semi-empirical models in this approach and the associated formulation, the results from this computationally efficient 1-D technique are shown to be in agreement with the results obtained from the full 2-D CFD technique as well as numerous relevant experimental runs (Kurita et al. 2011; Gorgitrattanagul et al. 2011; and Lu et al. 1995) for which the modeling assumptions hold.

Table 1.1
Summary of the problems solved using the three computational tools and a list of current and former doctoral students responsible for their development.

Code	Code Development	Investigations	Students
2-D CFD code implemented on FORTRAN platform	Development of steady/unsteady internal condensing flow codes	1. Investigation of the effect of gravity, shear, surface tension, noise-sensitivity on the internal condensing flows. 2. Study the attainability of steady/unsteady solutions.	Q. Liu (1999), G. Yu (2001), Q. Liang (2003), L. Phan (2006), S. Kulkarni (2010).
	Development of steady/unsteady external condensing flow codes	1. Comparison with classical gravity driven and shear driven analytical solutions. 2. Stability analysis	L. Phan (2006), S. Kulkarni (2010).
2-D CFD code implemented on COMSOL/MA TLAB platform	Development of steady/unsteady internal condensing flow codes for macro-scale application	1. Impact of transverse gravity, noise-sensitivity and surface tension. 2. Length of annular flow.	S. Mitra, R. R. Naik.
	Development of steady/unsteady internal condensing flow codes for micro-scale application	Investigate the impact of surface tension, disjoining pressures and thermal non-equilibrium, vapor compressibility.	R. R. Naik
1-D code	Development of steady internal condensing flows simulation tool	Demarcation of non-dimensional parameter space into gravity and shear driven zones.	S. Mitra, R. Naik, S. Kulkarni (2010).

1.5 Need for the New Tools

Limitations of Earlier Simulation Tool

The earlier simulation tool implementation on FORTRAN yielded results only for a short length of partially condensing flows (see Narain et al. 2009; Narain et al. 2007; Narain et al. 2008; Narain et al. 2007) under the assumptions of annular/stratified flows, incompressible vapor flow, and laminar vapor flow. Also the tool was not accurate for shear driven flow simulations. Towards satisfactorily addressing the issues related to length of annularity, complete condensation, noise-sensitivity in shear/pressure or gravity

driven flows, a more versatile computational tool was required. The solution technique (see Narain et al. 2004) for the earlier computational tool involved: (i) solving the mass, momentum and energy balance equations by SIMPLE technique Patankar 1980, (ii) developing an adaptive but simple meshing algorithm, (iii) solving the interface equations through subroutines written in FORTRAN. Therefore, the resulting tool, being huge, (because all the single-phase vapor and liquid domain solutions were obtained by this tool) and cumbersome. It can only be used to solve smaller domain problems and it took very long to solve the domain lengths of interest.

Also, the earlier tool assumes that the condensate position can be described as a film that is attached to the condensing surface. Also the interface location is described by a single-valued time-varying function. This approach can be used to simulate primarily annular/stratified condensing flows. For complete condensation cases with shear driven flows (as in horizontal condensers or zero gravity, see Kivisalu et al. 2011), even the annular flow is expected to operate under conditions of flow oscillations. However, the current computational approach is inherently unsuitable beyond a certain distance that defines the length of annular regime. As the flow transitions to non-annular regime, the long time evolutions of the interface would lead to wave break-up and/or plug-slug formations. These flow patterns are expected for fully condensing flows. Also the earlier simulation tool was not suitable for future investigation of vapor compressibility and vapor turbulence effects. Therefore, development of the much needed computational/modeling tool – on a COMSOL/MATLAB platform – was undertaken.

Initially, the same algorithm (see Narain et al. 2004) of the earlier code was implemented on the new COMSOL/MATLAB platform to solve only the

annular/stratified condensing flows. Eventually, the capabilities of the tool will be extended to solve non-annular flows by implementing the level-set technique Osher et al. 2003; Sussman et al. 1994. In the current implementation of the new tool, the individual domains of the condensing flow is solved by the in-built solvers in COMSOL, and the interface conditions are solved by subroutines written in MATLAB. Since for each individual single-phase domain, the meshing, and the numerical solution is handled by COMSOL's in-built finite element codes, our MATLAB-COMSOL combined code can handle much larger domains and the convergence is quicker. Moreover, once the new 2-D tool is further developed and validated for unsteady simulations, investigations of the impact of vapor turbulence and compressibility will be much easier to implement. Therefore, the condensing flow tool development on the COMSOL/MATLAB platform is thereforer much more versatile.

2 Mathematical Model for Steady Internal Condensing Flows

The 1-D governing equations presented in this chapter were previously published in Mitra et al. 2010^{*}, and Mitra et al. 2011[†]. The problem under consideration is of condensing flow inside a rectangular duct (see Fig. 2.1) at different inclinations with respect to gravity or cylindrical tube (see Fig. 2.2) that is along the gravity vector of different magnitude (including zero-gravity). The condensing flow is to be investigated for different operating conditions. Pure vapor of a refrigerant/fluid (FC-72, water, R113 etc.), at saturation temperature T_{sat} corresponding to the pressure at the inlet (p_{in}), enters the duct or tube at average speed U m/s as shown in Figs. 2.1 and 2.2. The thermal boundary condition of the condensing surface (lower plate for Fig. 2.1 or tube-walls for Fig. 2.2) is held at a temperature lower than the saturation temperature. Due to condensing surface being at a lower temperature compared to $T_{\text{sat}}(p_{\text{in}})$, film-wise condensation is assumed occur. The condensing surface is covered with condensate film as shown in Figs. 2.1 – 2.2. The simulation tool is developed to predict the configuration of the liquid-vapor interface, the flow variables for the liquid and the vapor phases at different operating conditions and gravity environments.

The two-dimensional (steady or unsteady) computational approach employed to investigate internal condensing flows in channels and tubes is based on the full governing equations described below.

^{*} The copyright permission for this paper can be found in Appendix A2.

[†] Some parts of the paper have been reproduced in this chapter by kind permission of Elsevier. The copyright permission is attached as separate document.

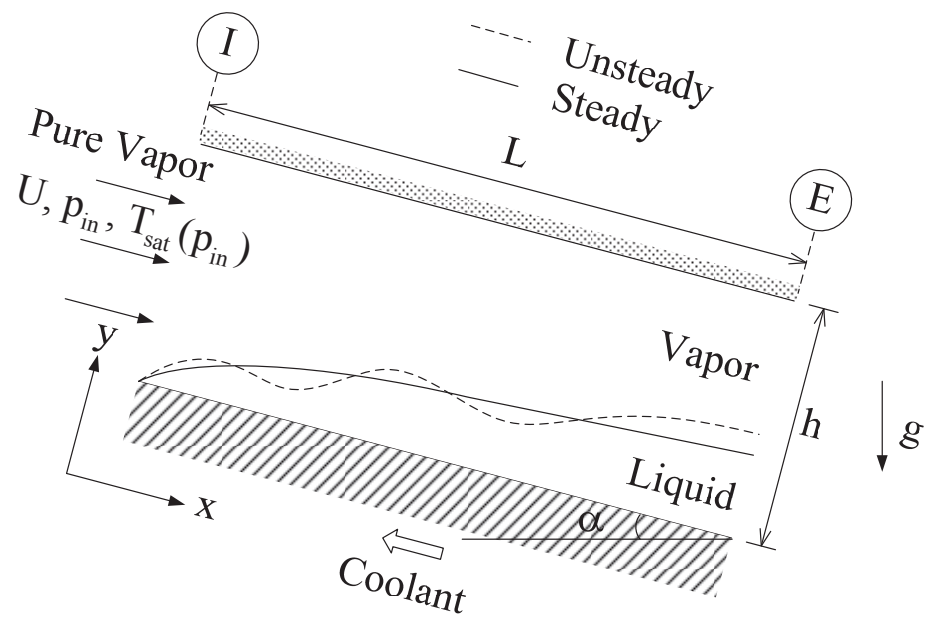


Figure 2.1: A schematic of a representation of internal condensing flow problem in a channel.

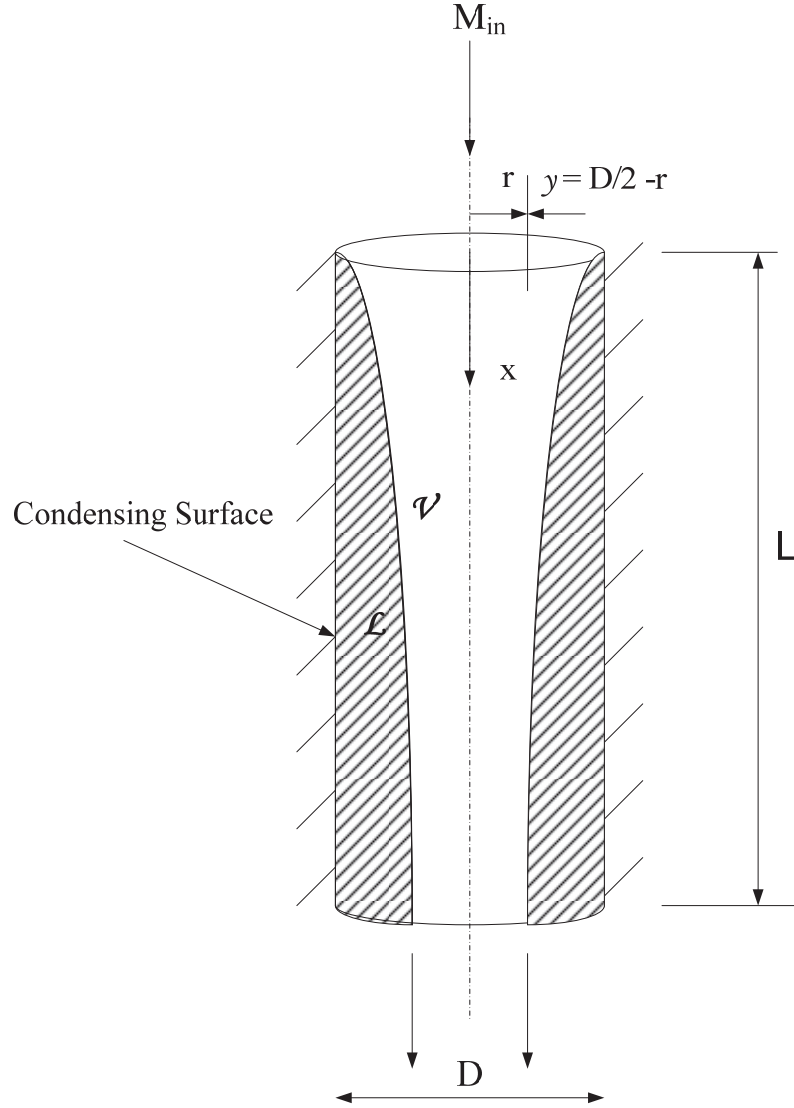


Figure 2.2: A schematic describing a representative internal condensing flow problem in a vertical tube.

The liquid and vapor phases in the flows of interest (see Figs. 2.1 – 2.2) are denoted by \mathcal{L} ($I = 1$) for liquid and \mathcal{V} ($I = 2$) for vapor. The fluid properties (density ρ , viscosity μ , specific heat C_p , and thermal conductivity k) with subscript I are assumed to take their representative constant values for each phase ($I = 1$ or 2). Let T_I be the temperature fields, p_I be the pressure fields, $T_{sat}(p)$ be the saturation temperature of the

vapor as a function of local pressure p , Δ be the film thickness, \dot{m} be the local interfacial mass flux, $T_w(x)$ ($< T_{\text{sat}}(p)$) be a known temperature variation of the condensing surface, and $\mathbf{v}_I = u_I \hat{\mathbf{i}} + v_I \hat{\mathbf{j}}$ be the velocity fields. Furthermore, the characteristic length L_c for the channel geometry is its channel gap ‘h’ shown in Fig. 2.1 and, for the tube geometry, L_c is the diameter D shown in Fig. 2.2. Let g_x and g_y be the components of gravity along x and y axes, $p_{\text{in}} \equiv p_0$ be the inlet pressure, $\Delta T(x) \equiv T_{\text{sat}}(p_{\text{in}}) - T_w(x)$ be a representative controlling temperature difference between the vapor and the bottom plate, $\Delta T \equiv T_{\text{sat}}(p_{\text{in}}) - \bar{T}_W$ be a reference temperature difference (where \bar{T}_W is the mean condenser surface temperature), h_{fg} be the heat of vaporization at local saturation temperature $T_{\text{sat}}(p)$ associated with local interfacial pressure p , and U be the average inlet vapor speed determined by the inlet mass flux. Let t represent the actual time and (x, y) represent the physical distances of a point with respect to the axes shown in Figs. 2.1 – 2.2 ($x=0$ is at the inlet, $y=0$ is at the condensing surface). For the tube flow in Fig. 2.2, the (x, r) axes are related to the (x, y) axes through $y = D/2 - r$. For the channel of height (or channel gap) ‘h’, $y = h$ is an isothermal slightly superheated non-condensing surface and, for the tube, $y = D/2$ (i.e. $r = 0$) is the center-line where symmetry condition holds for all flow variables of interest. Note that for both channel flow (Fig. 2.1) and in-tube (Fig. 2.2) flows, $y \equiv L_c \cdot y$ represents the distance from the condenser surface. We introduce a list of fundamental non-dimensional variables – viz. $(x, y, t, \delta, u_I, v_I, \pi_I, \theta_I, \dot{m})$ through the following definitions:

$$\begin{aligned} \{x, y, \Delta, u_I, \dot{m}\} &\equiv \{L_c \cdot x, L_c \cdot y, L_c \cdot \delta, U \cdot u_I, \rho_I \cdot U \cdot \dot{m}\} \\ \{v_I, T_I, p_I, t\} &\equiv \{U \cdot v_I, (\Delta T) \cdot \theta_I, p_0 + \rho_I U^2 \cdot \pi_I, (L_c / U) \cdot t\}. \end{aligned} \quad (2.1)$$

2.1 Full Two Dimensional Condensing Flow Governing Equations

2.1.1 Interior Equations

The non-dimensional differential forms of mass, momentum (x and y components), and energy equations for the 2-D flow for any point in the interior of either of the incompressible phases ($I = 1$ or 2) are the well-known equations:

$$\begin{aligned}\frac{\partial u_I}{\partial x} + \frac{\partial v_I}{\partial y} &= 0 \\ \frac{\partial u_I}{\partial t} + u_I \frac{\partial u_I}{\partial x} + v_I \frac{\partial u_I}{\partial y} &= -\left(\frac{\partial \pi_I}{\partial x}\right) + Fr_x^{-1} + \frac{1}{Re_I} \left(\frac{\partial^2 u_I}{\partial x^2} + \frac{\partial^2 u_I}{\partial y^2}\right) \\ \frac{\partial v_I}{\partial t} + u_I \frac{\partial v_I}{\partial x} + v_I \frac{\partial v_I}{\partial y} &= -\left(\frac{\partial \pi_I}{\partial y}\right) + Fr_y^{-1} + \frac{1}{Re_I} \left(\frac{\partial^2 v_I}{\partial x^2} + \frac{\partial^2 v_I}{\partial y^2}\right) \\ \frac{\partial \theta_I}{\partial t} + u_I \frac{\partial \theta_I}{\partial x} + v_I \frac{\partial \theta_I}{\partial y} &\approx \frac{1}{Re_I Pr_I} \left(\frac{\partial^2 \theta_I}{\partial x^2} + \frac{\partial^2 \theta_I}{\partial y^2}\right),\end{aligned}\tag{2.2}$$

where $Re_I \equiv \rho_I U \hat{h} / \mu_I$, $Pr_I \equiv \mu_I C_{pl} / k_I$, $Fr_x^{-1} \equiv g_x \hat{h} / U^2$ and $Fr_y^{-1} \equiv g_y \hat{h} / U^2$.

2.1.2 Interface Conditions

The nearly exact interface conditions for condensing flows are given in Narain et al. 2004, and Delhaye 1974. The following interface conditions have been also used to solve various condensing flow problems investigated, and are also available in Narain et al. 2004, Phan et al. 2006, Mitra et al. 2011. Utilizing a superscript “i” for values of flow variables at the interface $\phi \equiv y - \Delta(x, t) = 0$, non-dimensional forms of the interface conditions (see Narain et al. 2004) are given below.

The non-dimensional form of the requirement of continuity of tangential component of velocities becomes:

$$u_2^i = u_1^i - \delta_x (v_2^i - v_1^i),\tag{2.3}$$

where $\delta_x \equiv \partial \delta / \partial x$.

- The non-dimensional form of the normal component of momentum balance at the interface becomes:

$$\pi_1^i = \frac{\rho_2}{\rho_1} \pi_2^i - \frac{1}{We} \left(\frac{\delta_{xx}}{[1 + \delta_x^2]^{3/2}} \right) + \dot{m}^2 \left(\frac{\rho_1}{\rho_2} - 1 \right), \quad (2.4)$$

where $We \equiv \rho_1 U^2 h / \sigma$, and surface tension $\sigma = \sigma(T)$ where T is the interfacial temperature.

- The tangential component of momentum balance at the interface (see Eq. (A. 4) in Narain et al. 2004 and in Appendix A3) becomes:

$$\frac{\partial u_1}{\partial y} \Big|_i = \frac{\mu_2}{\mu_1} \frac{\partial u_2}{\partial y} \Big|_i + [t], \quad (2.5)$$

where the term $[t]$ in Eq. (2.5) is defined in Eq. (A.9) of Narain et al. 2004 and in Appendix A3. In Eq. (2.5), the left hand side approximately represents the non-dimensional value of tangential shear stress on the condensate (see Fig. 2.3) and the first term on the right hand side represents the tangential shear stress on the vapor.

- The non-dimensional form of non-zero interfacial mass fluxes \dot{m}_{LK} and \dot{m}_{VK} (defined in Eq. (A.5) of Narain et al. 2004 and in Appendix A3) impose kinematic constraints on the interfacial values of the liquid and vapor velocity fields and are given by:

$$\begin{aligned} \dot{m}_{LK} &\equiv \left[u_1^i (\partial \delta / \partial x) - (v_1^i - \partial \delta / \partial t) \right] / \sqrt{1 + (\partial \delta / \partial x)^2}, \text{ and} \\ \dot{m}_{VK} &\equiv (\rho_2 / \rho_1) \left[u_2^i (\partial \delta / \partial x) - (v_2^i - \partial \delta / \partial t) \right] / \sqrt{1 + (\partial \delta / \partial x)^2}. \end{aligned} \quad (2.6)$$

- The non-dimensional form of non-zero interfacial mass flux \dot{m}_{Energy} (as given by Eq. (A.6) of Narain et al. 2004 and in Appendix A3) represents the constraint imposed by net energy transfer across the interface and is given by:

$$\dot{m}_{Energy} \equiv Ja / (Re_1 Pr_1) \{ \partial \theta_1 / \partial n \Big|_i - (k_2 / k_1) \partial \theta_2 / \partial n \Big|_i \}, \quad (2.7)$$

where $Ja \equiv C_{p1}\Delta T / h_{fg}^0$, and $h_{fg}^0 \equiv h_{fg}(T_s(p_0)) \cong h_{fg}(T_s(p_2^i))$.

- The interfacial mass balance requires that the net mass flux (in kg/m²/s) at a point on the interface, as given by Eq. (A.7) of Narain et al. 2004 and in Appendix A3, be single-valued regardless of which physical process is used to obtain it. The non-dimensional form of this requirement becomes:

$$\dot{m}_{LK} = \dot{m}_{VK} = \dot{m}_{Energy} \equiv \dot{m}. \quad (2.8)$$

It should be noted that negligible interfacial thermal resistance and equilibrium thermodynamics on either side of the interface is assumed to hold for all x – values after a very small distance downstream of the origin.

- The non-dimensional thermodynamic restriction on interfacial temperatures (as given by Eq. (A.8) in Narain et al. 2004 and in Appendix A3) becomes:

$$\theta_1^i \cong \theta_2^i = T_s(p_2^i)/\Delta T \equiv \theta_s(\pi_2^i). \quad (2.9)$$

Within the vapor phase, for the refrigerants considered here, changes in absolute pressure relative to the inlet pressure are big enough to affect vapor motion but, at the same time, they are usually very small (except in micro-scale ducts) to affect saturation temperatures. Therefore, we have $\theta_s(\pi_2^i) \cong \theta_s(0)$.

2.1.3 Boundary Conditions

The problem posed by Eqs. (2.2) – (2.9) are computationally solved subject to the boundary conditions as shown on a representative film profile in Fig 2.3.

Top wall: The upper wall temperature $T_2(x, h, t) = T_{2@0} > T_{sat}(p_0)$ is at a superheated value close to saturation temperature to allow the assumption of a nearly constant saturation temperature for the vapor at all location. This is reasonable because interfacial

heat transfer effects of superheat (in the typical 5 – 10°C range) are negligible compared to the amount of latent heat released at the interface and conductive heat-transfer rate into the condensate.

Bottom wall: Besides the no-slip condition ($u_1(x, 0, t) = v_1(x, 0, t) = 0$) at the condensing surface, condensing-surface temperature ($T_1(x, 0, t) = T_w(x)$) is also prescribed, its non-dimensional form is written as

$$\theta_1(x, 0, t) = \theta_w(x) \equiv T_w(x) / \Delta T \quad (2.10)$$

Here Eq. (2.10) is known as steady temperature boundary condition for a known condensing surface temperature distribution $T_w(x)$.

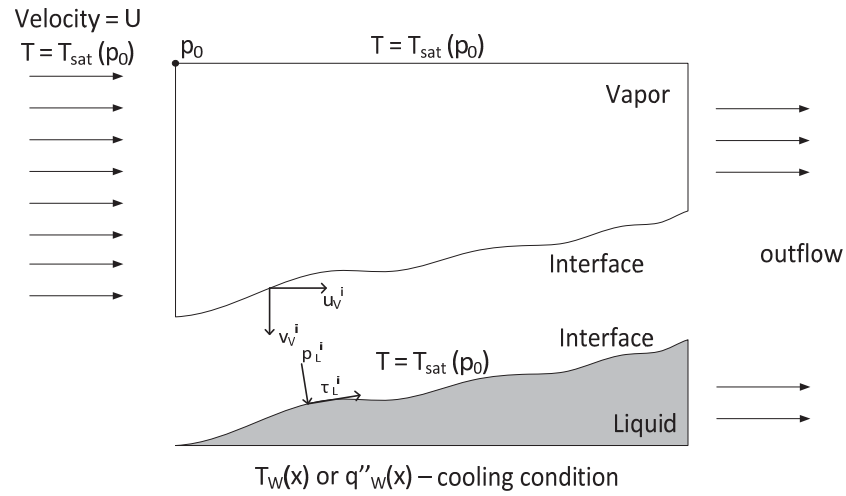


Figure 2.3: With the help of a representative film profile, the figure shows the boundary conditions for the liquid and the vapor domains present in an internal condensing flow.

Inlet Conditions: At the inlet $x = 0$, we have $u_2 = U$ and hence:

$$u_2(0, y, t) = 1, \quad \partial v_2 / \partial x|_{x=0} = 0. \quad (2.11)$$

Pressure is not prescribed across the inlet boundary but its value p_0 is specified at the corner point at the intersection of the inlet and the top wall. The inlet pressure $p_{in} (= p_0)$

appears indirectly through important thermodynamic properties such as $h_{fg}(p_2^i) \approx h_{fg}(p_0)$ and $T_{sat}(p_2^i) \approx T_{sat}(p_0)$. The algorithm used to solve the interior and interface equations is outlined in Chapter 3.

2.2 Quasi One Dimensional (1-D) Governing Equations

The nearly exact steady solutions for shear and gravity driven flows in Figs. 2.1 – 2.2 that have been obtained by the full 2-D approach for the steady 2-D governing equations given above, can also be obtained by a more approximate and efficient 1-D solution technique. The 1-D technique is different from most other 1-D tools (Dobran et al. 1980, Narain 1996, Chen et al. 2009, etc.) that use average flow variables and incorporate assumed empirical models (such as friction factor models for the interface, pressure gradient models, certain turbulence models, etc.) in the solution procedure. For laminar vapor and thin laminar condensate flows, the method reported here is called “quasi” 1-D because it is analytically exact except for thin film approximation and an approximate assumption regarding the nature of the cross-sectional variation (i.e. y-variation) of the vapor profile $u_2(x,y)$. In the 1-D solution technique such as this, integral forms of vapor phase momentum and mass balances are used to minimize the impact, that arise from the assumed nature of y-variation of the vapor velocity profile, on the predicted values of the one-dimensional variables of interest.

The differential form of the governing equations (see Eq. 2.2) for laminar condensate ($I = 1$) flows (x and y components of the momentum balance and the energy equation) are simplified under the assumptions of steady flows, boundary layer approximations

($\partial/\partial x \ll \partial/\partial y$ & $v_1 \ll u_1$), negligible inertia in the momentum equations, and negligible convection terms in the energy equation. These simplified equations are:

$$\begin{aligned}
0 &\cong u_1 \frac{\partial u_1}{\partial x} + v_1 \frac{\partial v_1}{\partial x} \cong \frac{1}{\text{Re}_1} \frac{\partial^2 u_1}{\partial x^2} - \frac{\partial \pi_1}{\partial x} + \text{Fr}_x^{-1} \\
&\quad - \frac{\partial \pi_1}{\partial y} + \text{Fr}_y^{-1} \cong 0, \text{ and} \\
0 &\cong \frac{1}{\text{Re}_1 \text{Pr}_1} \left(\frac{\partial^2 \theta_1}{\partial y^2} \right)
\end{aligned} \tag{2.12}$$

In Eq. (2.12) above, $\text{Re}_1 \equiv (\rho_1 U L_c)/\mu_1$, $\text{Fr}_x^{-1} \equiv g_x L_c / U^2$, $\text{Fr}_y^{-1} \equiv g_y L_c / U^2$, and $\text{Pr}_1 \equiv \mu_1 C_{pl}/k_1$. In addition to the approximation leading to Eq. (2.12), this formulation also assumes uniform cross-sectional pressure assumption for the vapor phase ($p_2 = p_2(x) = p_0 + \rho_2 U^2 \pi_2(x)$ with $\pi \equiv \pi_2(x)$ and $\pi(0) = 0$), negligible impact of vapor super heat, and negligible interfacial slope approximation ($\delta'(x)^2 \ll 1$). As a result, interface conditions given by Eqs. (2.3) - (2.9) are simplified and replaced by Eqs. (2.13) - (2.16) given below:

$$u_2^i = u_1^i = u_f(x) \tag{2.13}$$

$$\pi_1^i = \frac{\rho_2}{\rho_1} \pi_2^i = \frac{\rho_2}{\rho_1} \pi(x) \tag{2.14}$$

$$\left. \frac{\partial u_1}{\partial y} \right|^i = \frac{\mu_2}{\mu_1} \left. \frac{\partial u_2}{\partial y} \right|^i \tag{2.15}$$

$$\dot{m}_{\text{Energy}} \cong \text{Ja}/(\text{Re}_1 \text{Pr}_1) \{ \partial \theta_1 / \partial y \}^i \tag{2.16}$$

In Eq. (2.16) above, $\text{Ja} \equiv C_{pl} \Delta T / h_{fg}(p_0)$. A characteristic length, $L_c = h$ (for the channel case) and $L_c = D$ (for the tube case) is chosen to define the inlet Reynolds number $\text{Re}_{in} = \rho_2 U L_c / \mu_2$. The non-dimensional variable definitions introduced in Eq. (2.1) remains valid

for both channel and tube geometries. For thin condensate motion ($\delta \ll 1$, etc), the inertia term in the x-component of momentum balance and the convection term of energy balance in Eq. (2.2) is dropped for $I = 1$ as this does not alter the solution of the original problem for the range of parameters and flow conditions of interest here. The validity of this modeling approximation is verified through comparison of solutions obtained from this approach with those obtained from computationally solving the full equations (which retains liquid inertia terms) in the two-dimensional approach. These approximations yield an analytical solution (and representation) for the liquid velocity $u_1(x, y)$ and the temperature $\theta_1(x, y)$. These are given as:

$$u_1(x, y) = \left\{ -\frac{d\pi(x)}{dx} + \frac{\rho_1}{\rho_2} Fr_x^{-1} - \frac{\rho_1}{\rho_2} Fr_y^{-1} \frac{d\delta}{dx} \right\} \frac{Re_{in}}{2} \cdot \frac{\mu_2}{\mu_1} y(\delta(x) - y) + \frac{u_f(x)}{\delta(x)} y \quad (2.17)$$

$$\theta_1(x, y) = \varphi_t(x) \frac{y}{\delta(x)} + \theta_W(x) \quad (2.18)$$

where $\varphi_t(x) \equiv \frac{T_{sat}(p_0) - T_w(x)}{T_{sat}(p_0) - \bar{T}_W} = \frac{\Delta T(x)}{\Delta T}$ and $\theta_W(x) = \frac{T_w(x)}{\Delta T}$. For the case of uniform condensing surface temperature $T_w(x) = \bar{T}_W$ at all x , $\varphi_t(x) = 1$ and $\theta_W(x)$ is a constant equal to $\bar{T}_W/\Delta T$.

The unknown functions appearing in (2.17) and (2.18) are: $\delta(x)$, $u_f(x)$, $\pi(x)$, and $\zeta(x) \equiv d\pi(x)/dx$. The equations controlling these variables are: integral forms of mass and momentum balance for the vapor control volume of width ' Δx ' (see Fig. 2.1), the mass balance for the liquid control volume of width ' Δx ', and the interface conditions in Eqs. (2.13) - (2.16). The integral mass and momentum balance equations for the liquid and vapor phase motion at any x in the channel geometry are respectively given as:

$$\dot{m}(x) = \frac{d}{dx} \left\{ \int_0^{\delta(x)} u_1(x, y) dy \right\} = -\frac{\rho_2}{\rho_1} \left\{ \frac{d}{dx} \int_{\delta(x)}^1 u_2(x, y) dy \right\} \quad (2.19)$$

and

$$\begin{aligned}
& -\frac{d\pi(x)}{dx}\{1-\delta(x)\} + \frac{1}{\text{Re}_{\text{in}}}\left[\frac{\partial u_2(x,1)}{\partial y} - \frac{\partial u_2(x,\delta(x))}{\partial y}\right] - \frac{\rho_1}{\rho_2}\dot{m}(x)u_f(x) \\
& + \text{Fr}_x^{-1}\{1-\delta(x)\} \\
& = \frac{d}{dx}\left[\int_{\delta(x)}^1 u_2^2(x,y)dy\right].
\end{aligned} \tag{2.20}$$

For the in-tube geometry shown in Fig. 2.2, corresponding equations at any x in the tube, under the notation $\hat{r} \equiv r/D$, are given as:

$$\dot{m}(x) = \frac{2}{1-2\delta}\frac{d}{dx}\left\{\int_{\frac{1-2\delta}{2}}^{\frac{1}{2}} u_1(x,\hat{r})\hat{r}\cdot d\hat{r}\right\} = -\frac{2}{1-2\delta}\frac{\rho_2}{\rho_1}\frac{d}{dx}\left\{\int_0^{\frac{1-2\delta}{2}} u_2\hat{r}\cdot d\hat{r}\right\} \tag{2.21}$$

and

$$\begin{aligned}
& -\frac{d\pi(x)}{dx}\left\{\frac{(1-2\delta)^2}{8}\right\} + \text{Fr}_x^{-1}\frac{(1-2\delta)^2}{8} - \frac{1}{2}\frac{\mu_1}{\mu_2}\cdot\frac{1}{\text{Re}_{\text{in}}}\frac{\partial u_1}{\partial y}\bigg|^i(1-2\delta) \\
& = \frac{d}{dx}\left\{\int_0^{\frac{1-2\delta}{2}} u_2^2\hat{r}\cdot d\hat{r}\right\} + \frac{1}{2}\frac{\rho_1}{\rho_2}(1-2\delta)\dot{m}(x)u_f(x).
\end{aligned} \tag{2.22}$$

For the in-channel geometry, the equations (2.15), (2.16), (2.19), and (2.20) are to be satisfied for a reasonable choice for the vapor velocity profile $u_2(x, y)$. One such reasonable choice used in this study is:

$$u_2(x,y) = u_f\frac{1-y}{1-\delta} + b_1(x)\left[\frac{y-\delta}{1-\delta}\left\{\frac{y-\delta}{1-\delta} - 1\right\}\right] \tag{2.23}$$

In Eq. (2.23), the requirement of onset of condensation at $x = 0$ demands $\delta(0) = 0$, and $u_f(0) = 0$. The requirement that the inlet vapor velocity profile $u_2 = U.u_2(0,y)$ be a fully developed parabola with an average speed of U demands that $b_1(0) = 6$.

To get an additional estimate for validation and regularity of this 1-D approach, another choice for $u_2(x,y)$ that was used is:

$$u_2(x, y) = b_2(x)\{(y - \delta) - (y - \delta)^2\} + u_f(x) \left[1 - (y - \delta) \left\{ \frac{6\delta}{u_f} + \frac{1}{1-\delta} \right\} \right] \quad (2.24)$$

In Eq. (2.24), the requirements of onset of condensation at $x = 0$ and a fully developed parabolic velocity profile $u_2 = U.u_2(0, y)$ at the inlet, demands: $\delta(0) = 0$, $u_f(0) = 0$ and $b_2(0) = 6$.

The vapor velocity profile representation choices in Eq. (2.23) or Eq. (2.24) have been chosen to be consistent with the liquid velocity profile representation in Eq. (2.17) (i.e., they automatically satisfy Eq. (2.13)).

For the vertical in-tube case of Fig. 2.2, the expected symmetry of the vapor velocity makes a good choice for vapor velocity easier and more accurate than the asymmetric channel vapor velocity profile cases considered here. The good choice employed in this paper is:

$$u_2(x, \hat{r}) = 4 \frac{u_f(x) - u_m(x)}{(1 - 2\delta)^2} \hat{r}^2 + u_m(x) \quad (2.25)$$

In Eq. (2.25), the requirements of the onset of condensation and a fully developed parabolic velocity profile $u_2 = U.u_2(0, r)$ at the inlet demands: $\delta(0) = 0$, $u_f(0) = 0$, and $u_m(0) = 2$.

The use of interface shear condition in Eq. (2.25), effectively expresses the unknown functions - $b_1(x)$ in Eq. (2.23) or $b_2(x)$ in Eq. (2.24) or $u_m(x)$ in Eq. (2.25) – in terms of the primary unknown functions: $\delta(x)$, $u_f(x)$, $\pi(x)$, and $\zeta(x) \equiv d\pi(x)/dx$. The algebraic approach used to express all other functions in terms of the unknown functions $\delta(x)$, $u_f(x)$, $\pi(x)$, and $\zeta(x) \equiv d\pi(x)/dx$ and the computational approach needed to solve for the unknown functions are given in Chapter 3.

3 Computational Methodology

3.1 Two-Dimensional Computational Algorithm

The 1-D and 2-D computational approach presented in this chapter is also available in Mitra 2011[‡] and Mitra 2010[§].

A new 2-D computational tool has been developed for the flow in a channel schematically shown in Fig. 2.1. This approach uses commercial software to solve the interior equation given in Eq. (2.2) and uses separate code development platform to implement an algorithm that satisfies all the interface equation given in Eq. (2.3) – (2.9). The choice of commercial software was COMSOL MULTIPHYSICS, and for code/algorithm development the preferred choice was MATLAB, because this software easily integrates with COMSOL. This new tool is based on an algorithm which takes an initial guess for the interface location and the interfacial flow variables and then improves upon them until convergence, by using an iterative scheme outlined in this Chapter.

The non-linear ODE based quasi one-dimensional model can be used to provide a good engineering estimate of interfacial location and interfacial velocity of steady annular stratified flow in this geometry. This estimate can be used as an initial guess for the 2-D computational approach to expedite convergence, but is not a necessity. The algorithm for the two-dimensional tool is similar to the earlier CFD approach (Narain et al. 2004). The simulation tool locates an interface ($\phi(x, y, z, t) = 0$) by solving the interface tracking equation arising from the interface energy/mass transfer condition:

[‡] Some parts of the paper have been reproduced in this chapter by kind permission of Elsevier. The copyright permission is attached as separate document.

[§] The copyright permission for this paper can be found in Appendix A2.

$$\dot{m}_{LK} = \dot{m}_{Energy} \quad (3.1)$$

where \dot{m}_{LK} is the interfacial mass-flux (kg/m²/s) determined by the normal component of interfacial liquid velocity relative to the interfacial velocity (see eq. (A.5) of Narain et al. 2004) and \dot{m}_{Energy} is the interfacial mass-flux (kg/m²/s) determined by the interfacial energy balance (see eq. (A.6) of Narain et al. 2004) requirement associated with removal of latent heat released by the condensation rate. This requirement is rewritten in its popular interface evolution equation form:

$$\frac{\partial \phi}{\partial t} + \mathbf{V}_{eff} \cdot \nabla \phi = 0 \quad (3.2)$$

where $\mathbf{V}_{eff} \equiv \mathbf{v}_1^i - (\kappa_1 \cdot \nabla T_1|_i - \kappa_2 \cdot \nabla T_2|_i) \cdot (1/\rho_1) \cdot (1/h_{fg})$ is the modified velocity determined by the liquid interfacial velocity \mathbf{v}_1^i , liquid and vapor temperature gradients at the interface ($\nabla T_1|_i$ and $\nabla T_2|_i$ respectively), liquid density ρ_1 , liquid and vapor thermal conductivities (κ_1 and κ_2 respectively), and the latent heat or heat of vaporization h_{fg} . The above equation is currently solved by a 2D interface tracking method valid only if ϕ is explicitly given as, $y - \delta(x,t) = 0$. In the forthcoming evolution of this approach, we propose to enhance this interface tracking method by a level-set type technique Osher et al. 2003, and Sussman et al. 1994 for solving the above Eq. (3.2) without any assumption on the form of ϕ .

The proposed approach is different than the approach in other level-set techniques Osher et al. 2003, Sussman et al. 1994, Mukherjee et al. 2004, Son et al. 1998 on three counts: (i) the “interface” is to be modeled as “sharp” instead of the more common “thin

zone” models used for level set simulations, (ii) the liquid and vapor domains are to be solved separately and consecutively (as in the approach reported here) as opposed to concurrent solving of both the domains in popular level-set approach, and (iii) the original hyperbolic nature of the interface tracking equation will be retained (as in the approach reported here) as opposed to tweaking of this equation with diffusive terms for computational convenience.

The computational tool development used here is based on the solution algorithm described below:

I. The guess of film thickness, interfacial velocities for the liquid domain, and interfacial mass flux obtained from the 1D simulation are used to compute the interfacial vapor velocities through “functions” in MATLAB. Steady and unsteady simulations use one of the *interfacial mass-flux conditions* ($\dot{m}_{VK} = \dot{m}_{Energy}$) in Eq. (2.6) and (2.8) and the *continuity of tangential velocity* (Eq. 2.3) to obtain the normal and tangential components (or, equivalently, the x- and y-component of the vapor velocity u_2^1 and v_2^1) of the interfacial vapor velocity from the guessed values of liquid interfacial velocities (u_1^1 and v_1^1) and film thickness. For the steady equations, the time derivatives in these equations are set to zero.

II. From the interfacial values of the vapor velocities obtained above, the CFD solution for the vapor domain (marked \mathcal{V} in Fig. 2.1) governing equations (Eq. (2.2) for $I = 2$) is obtained/implemented on the COMSOL/MATLAB platform based on the remaining boundary conditions (inlet and top wall) as discussed in chapter 2 and depicted in Fig. 2.3. The interface location is used to create and mesh the vapor domain in Fig. 2.3 with the help of ALE (“Arbitrary Lagrangian -

Eulerian”) method Modeling_Guide available on COMSOL. This ALE method is an effective moving boundary/mesh method for these types of problems.

III. The necessary information from the vapor domain solution is extracted and transferred to the liquid domain such that the normal and tangential stress τ_1^i and p_1^i shown in Fig. 2.3 are obtained with the help of Eq. (2.4) and Eq. (2.5). The momentum, continuity and energy equations (Eqs. (2.2) for $I = 1$) for the liquid domain (marked \mathcal{L} in Fig. 2.1) is solved on COMSOL platform for the current location of the interface (same as that for the vapor domain calculation in step II). This is done by prescribing the boundary conditions – which are “normal (pressure) and tangential (shear) stress conditions” at the interface, an “outflow” condition at the exit, and wall conditions at the condensing surface based on the nature of cooling condition as shown in Fig. 2.3. For most of the investigations undertaken for this study, a prescribed saturation temperature condition at the interface and prescribed wall temperature at the condensing surface suffices to specify temperature boundary conditions for the different forms of the energy equation. Again, ALE method is used to create and mesh the liquid domain in Fig. 2.3.

IV. For the steady problem, Eq. (3.2) is solved to get an updated value of the interface location (ϕ). The updated value of the interface location is to be used to solve the vapor domain as shown in step-I. The ALE method is now used to remap all the variables to the new vapor and liquid domains corresponding to the updated value of the interface.

Steps I to IV are repeated until all the interfacial variables are converged and all interface and boundary conditions are satisfied.

V. For an unsteady problem, the known initial values for the interface location ($\phi(\mathbf{x}, t) = 0$ or $y = \delta(x, t)$) at $t = n\Delta t$, $n = 0, 1, 2$, etc. are used to predict the interface location at discrete values of times $t = (n+1)\Delta t$ at any interfacial location $\mathbf{x} \equiv x\mathbf{i} + y\mathbf{j} + z\mathbf{k}$. This is currently done through the interface tracking approach used by us.

Furthermore, the choice of the grid for tracking the interface is such that it satisfies, as in Narain et al. 2004, the Courant number restriction ($Cr_x \approx 1$, $Cr_y \approx 1$ and $Cr_z \approx 1$), allowing accurate resolution of wave amplitudes and their phase angles even for relatively coarse grids. This discretization approach makes the solution scheme verifiably compatible with analytically obtained “method of characteristics” approaches.

VI. After obtaining *tentative* new interface locations for time $t = (n + 1)\Delta t$ as described above, each domain is solved as in the steps II and III for this new interface boundary with the help ALE method. This method moves the existing mesh inside the domains to conform to the new interface locations ($\mathcal{L}_t \rightarrow \mathcal{L}_{t+\Delta t}$ and $\mathcal{V}_t \rightarrow \mathcal{V}_{t+\Delta t}$) and creates new geometries from the moved meshes, namely $\mathcal{L}_{t+\Delta t}$ and $\mathcal{V}_{t+\Delta t}$. The ALE method is also used to remap the flow field values in the interiors and at the interface of \mathcal{L}_t and \mathcal{V}_t to the interiors and at the interface of $\mathcal{L}_{t+\Delta t}$ and $\mathcal{V}_{t+\Delta t}$ respectively.

VII. The above sequence of steps I-IV are repeated at each time until a good estimate of the interface location at $t = (n+1)\Delta t$ is obtained in step III. These iterations for the same time-step also ensures that the effective velocity \mathbf{v}_{eff} used in the interface tracking equation has converged.

VIII. Repetition of the steps I to V above will yield converged interface locations and CFD solutions for each domain at each $t = n\Delta t$ for $n = 1, 2$, etc.

In forthcoming evolutions of this approach, it is planned that the current method of interface tracking ($\phi = y - \delta(x,t) = 0$) will be replaced by a “level-set” type method for which $\phi = 0$ will remain implicit at each time-step.

3.2 One-dimensional Solution Technique

Formulation for known condensing surface temperature boundary condition of $T_1(x,0) = T_w(x)$

With the algebra done on a suitable symbolic manipulation software (e.g. Mathematica from Wolfram Research Inc., USA), the formulation for both the in-tube and in-channel laminar/laminar steady annular/stratified flows (for 1g or 0g) are obtained from the defining equation $d\pi(x)/dx \equiv \zeta(x)$, and three independent governing equations arising from: interface energy balance in Eq. (2.16), integral mass balance in Eq. (2.19) or Eq. (2.21), and integral vapor momentum balance in Eq. (2.20) or Eq. (2.22). These governing equations are obtained after substituting for u_1 from Eq. (2.17), θ_1 from Eq. (2.18), and u_2 from Eq. (2.23) or Eq. (2.24) or Eq. (2.25) as the case may be. These four

governing equations are written in the following vector form of a coupled set of four first order non-linear ordinary differential equations:

$$\mathbf{A} \frac{dy}{dx} = \mathbf{f}(\mathbf{y}, x) \quad (3.3)$$

$$\mathbf{y}(x) \equiv [u_f(x), \delta(x), \pi(x), \zeta(x)]^T$$

$$\mathbf{A} = \begin{bmatrix} 0 & 0 & 1 & 0 \\ A_{11} & A_{12} & 0 & A_{14} \\ C_{11} & C_{12} & C_{13} & C_{14} \\ D_{11} & D_{12} & 0 & D_{14} \end{bmatrix}$$

$$\mathbf{f}(\mathbf{y}, x) = [\zeta(x), 0, f_3, f_4]$$

with known non-linear functions (of \mathbf{y} and x) for A_{11} , A_{12} , A_{14} , C_{11} , C_{12} , C_{13} , C_{14} , D_{11} , D_{12} , D_{14} , f_3 and f_4 (obtained from symbolic manipulation software Mathematica) which implements the definitions given in the Appendix A1.

The problem in Eq. (3.3) is equivalently posed as:

$$\frac{dy}{dx} \equiv \mathbf{A}^{-1} \cdot \mathbf{f}(\mathbf{y}, x) \equiv \mathbf{g}(\mathbf{y}, x) \quad (3.4)$$

where, at $x = 0$, we have the requirements

$$\mathbf{y}(0) = [0, 0, 0, \zeta(0^+)]^T \quad (3.5)$$

In the formulation in Eq. (3.4), the function $\mathbf{g}(\mathbf{y}, x)$ explicitly depends on x only for only those cases for which the condensing surface temperature $T_w(x)$ has a well known non unit prescription. The function $\mathbf{g}(\mathbf{y}, x) = \mathbf{g}(\mathbf{y})$ is independent of x for the uniform prescription of condensing surface temperature $T_w(x) = \bar{T}_w$ for all x . Unless otherwise stated, the thermal boundary condition is always assumed to be one of uniform condensing surface temperature \bar{T}_w .

The solutions of the integral formulation (3.4) - (3.5) have not been previously implemented in the known literature. This is partly because both $\zeta(0^+)$ in $\mathbf{y}(0)$ in Eq. (3.5)

and $\mathbf{g}(\mathbf{y}(0),0)$ in Eq. (3.4) are not defined as they are unbounded in the limit of $x \rightarrow 0$. This makes the non-linear ODE problem “singular” and outside the realm of validity of the typical existence/uniqueness theorem for ODEs (see Arnold 1973 and Greenberg 1978). Therefore, one has the following possibilities: a unique solution exists, no solution exists, or multiple solutions exist.

It should also be noted that the presence of $d^2\pi/dx^2 = d\zeta/dx$ terms in the formulation of Eq. (3.4) makes the formulation different from strictly “parabolic” formulations for single-phase and air-water duct flows (where $\dot{m} = 0$) because formulations for such flows only exhibit presence of the first order $d\pi/dx$ terms (not $d^2\pi/dx^2$). Such strictly parabolic forms would only involve a vector of the type $\mathbf{y}(x) \equiv [u_f(x), \delta(x), \pi(x)]^T$ with well defined $\mathbf{y}(0)$. The steady formulation in Eq. (3.4) is not “elliptic” either because it is computationally found that one does not have multiple solutions with different approaches to $\zeta(0^+)$ that are associated with distinctly different exit pressures $\pi(x_e)$ at $x = x_e$.

Fortunately, despite the singularity at $x=0$, Eqs. (3.4) - (3.5) are integrable. The solution for $x \geq \varepsilon$ is obtained by choosing sufficiently small near zero values of $x = \varepsilon$, $u_f(\varepsilon)$, $\delta(\varepsilon)$, $\pi(\varepsilon)$ and obtaining the value of a consistent $\zeta(\varepsilon)$ from the integrated version of the mass balance (integral of Eq. (2.19) for channel flows and the integral of Eq. (2.21) for in-tube flows). For example, the integral of Eq. (2.19) is $\int_0^\delta u_1(x,y)dy + \frac{\rho_2}{\rho_1} \int_\delta^1 u_2(x,y)dy = \frac{\rho_2}{\rho_1}$ and this equation yields $\zeta(\varepsilon)$ in terms of ε , $u_f(\varepsilon)$, $\delta(\varepsilon)$, and $\pi(\varepsilon)$. With this information on $\zeta(\varepsilon)$ available, the problem given by Eqs. (3.4) – (3.5) is rewritten, for $x \geq \varepsilon$, as:

$$\frac{dy}{dx} \equiv \mathbf{g}(\mathbf{y}, x) \quad (3.6)$$

$$\mathbf{y}(\varepsilon) \equiv [u_f(\varepsilon), \delta(\varepsilon), \pi(\varepsilon) \text{ and } \zeta(\varepsilon)]^T \quad (3.7)$$

Equations (3.6) and (3.7) are not singular and are solved by one of the several Runge-Kutta solution schemes (e.g. there are several options available on MATLAB from The MathWorks, Inc., MA).

Equations (3.6) – (3.7) were used to extensively investigate the solutions for several channel heights, tube diameters, inlet vapor speeds, condensing surface temperatures, and fluids.

One of the key results established by the unique solution of the singular Eqs. (3.4) - (3.5) or its equivalent Eqs. (3.6) – (3.7) is that, the steady annular/stratified (or film wise) condensation solution does not “require” prescription of the exit pressure condition on $\pi(x)$ (at some non-zero $x = x_e$) despite the appearance of $d^2\pi/dx^2$ terms in Eq. (3.4) or Eq. (3.6). It is clear from the solution that, for existence of a steady annular/stratified partially condensing flow (under shear driven or gravity driven), there exists a unique self-sought value of steady exit pressure (or quality). The unsteady solutions from the full 2-D technique Liang et al. 2004 and experimental realizations (see Kurita et al. 2011) show that these “annular/stratified” steady flows are quite often stable up to certain distances. However, for shear driven, experiments in Kivisalu et al. 2011, and Kivisalu et al. 2011 have shown significant increase in the heat flux under impositions of pressure fluctuations at the inlet of the condenser.

Formulation for a known condensing surface heat flux ($q''_w(x)$) boundary condition

For condensers operating at known heat flux values $q''_w(x)$ (uniform or non-uniform with distance x) for the condensing surface, the interface energy balance condition in Eq. (3.16) is no longer considered a governing equation for the unknowns ($\delta(x)$, $u_f(x)$, $\pi(x)$, and $\zeta(x)$). The heat flux across the condensing-surface ($q''_w(x)$) is nearly equal to the interfacial heat flux ($\dot{m}(x)h_{fg}$) because of the linearity of the temperature profile assumption in Eq. (2.18) implies straight conductive heat transfer to the condensing-surface. Therefore, using the non-dimensional form of \dot{m} in Eq. (2.1) and the result for θ_1 in Eq. (2.18), the interface energy balance in Eq. (2.16) becomes

$$\frac{q''_w(x)}{\rho_1 U h_{fg}} \cong \dot{m}_{\text{Energy}}(x) = \frac{\text{Ja}}{\text{Re}_1 \text{Pr}_1} \cdot \frac{\phi_t(x)}{\delta(x)} \quad (3.8)$$

For a known $q''_w(x)$, the equality between the first and the last term in Eq. (3.8) is treated as an algebraic relation for obtaining $\phi_t(x)$ (or $T_w(x) = T_{\text{sat}}(p_0) - \Delta T \cdot \phi_t(x)$) once film-thickness $\delta(x)$ has been obtained from the solution procedure described below.

With $\dot{m} = \dot{m}_{\text{Energy}}$ becoming a known function through the first equality in Eq. (3.8), the integral mass balance in Eq. (2.19) splits into the following two separate equations:

$$\frac{d}{dx} \int_0^\delta u_1(x, y) dy = \frac{q''_w(x)}{\rho_1 U h_{fg}}, \quad \text{and} \quad (3.9)$$

$$-\frac{\rho_2}{\rho_1} \frac{d}{dx} \int_\delta^1 u_2(x, y) dy = \frac{q''_w(x)}{\rho_1 U h_{fg}}. \quad (3.10)$$

Again, with algebra done with the help of a computer software, the two separate mass balance equations (arising from Eq. (2.19) or Eq. (2.21)), the vapor momentum balance (from Eq. (2.20) or Eq. (2.22)), and the defining equation $d\pi(x)/dx \equiv \zeta(x)$ yield four

separate ordinary differential equations (ODEs) and lead to a formulation of the type given in Eq. (3.4) – (3.5) or Eq. (3.6) - (3.7). The resulting problems is again solved by one of the several Runge-Kutta solution schemes and, after the solutions are obtained, the condensing surface temperature is obtained from Eq. (3.8) – i.e. through: $T_w(x) = T_{\text{sat}}(p_0) - \Delta T \cdot \phi_t(x)$.

For many conjugate problems, however, one may only know (or have an estimate of) heat-flux variations $q''_w(x)$ for a given length of the condenser. But this is different than the ability to “fix” a certain heat-flux variation $q''_w(x)$ over the length of a condenser - which is experimentally feasible but is rare in practice.

4. Results and Discussion

The results and comparisons presented in this chapter were previously published in Mitra 2011^{**}, Kurita 2011^{††}, Kivisalu 2011^{‡‡}. The results have been reproduced with kind permission from Elsevier.

4.1 Accuracy of Computational Tools

4.1.1 Accuracy of the Two-Dimensional Computational Tool

The accuracy of the two-dimensional solution is ensured through satisfaction of the following criteria:

- (i) the convergence of the flow variables in the interior of each fluid domain is satisfied,
- (ii) all the interface conditions given in Chapter 2 are satisfied,
- (iii) the solution exhibits grid independence for each domain as well as for the complete condensing flow problem.

In the two-dimensional tool, each individual domain is repetitively solved by COMSOL as a single phase flow problem by specifying the boundary conditions described in Chapter 2. The convergence criterion for both liquid and vapor domain in the COMSOL's single phase fluid solver is set at 1E-6. For each domain, only converged

^{**} Some parts of the paper have been reproduced in this chapter by kind permission of Elsevier. The copyright permission is attached as separate document.

^{††} Some parts of the paper have been reproduced in this chapter by kind permission of Elsevier. The copyright permission is attached as separate document.

^{‡‡} Some parts of the paper have been reproduced in this chapter by kind permission of Elsevier. The copyright permission is attached as separate document.

solutions are considered for data processing. Thus, convergence of each domain is ensured.

For the steady solution, convergence of the overall two-phase flow is declared only when the flow variables in the interface conditions do not change with iterations. That is, once the condensing flow solution has converged, each of the flow variables such as, $\delta(x)$, $u_1^i(x)$, $v_1^i(x)$, $u_2^i(x)$, $v_2^i(x)$, $\tau_1^i(x)$, and $p_1^i(x)$ do not change much with every successive iteration. Satisfaction of each interface condition is checked. For example, the interfacial mass-flux terms in Eq. (2.8) are plotted and are checked for convergence. A sample plot with the interfacial mass-flux terms in Eq. (2.8) are shown in Fig. 4.1.

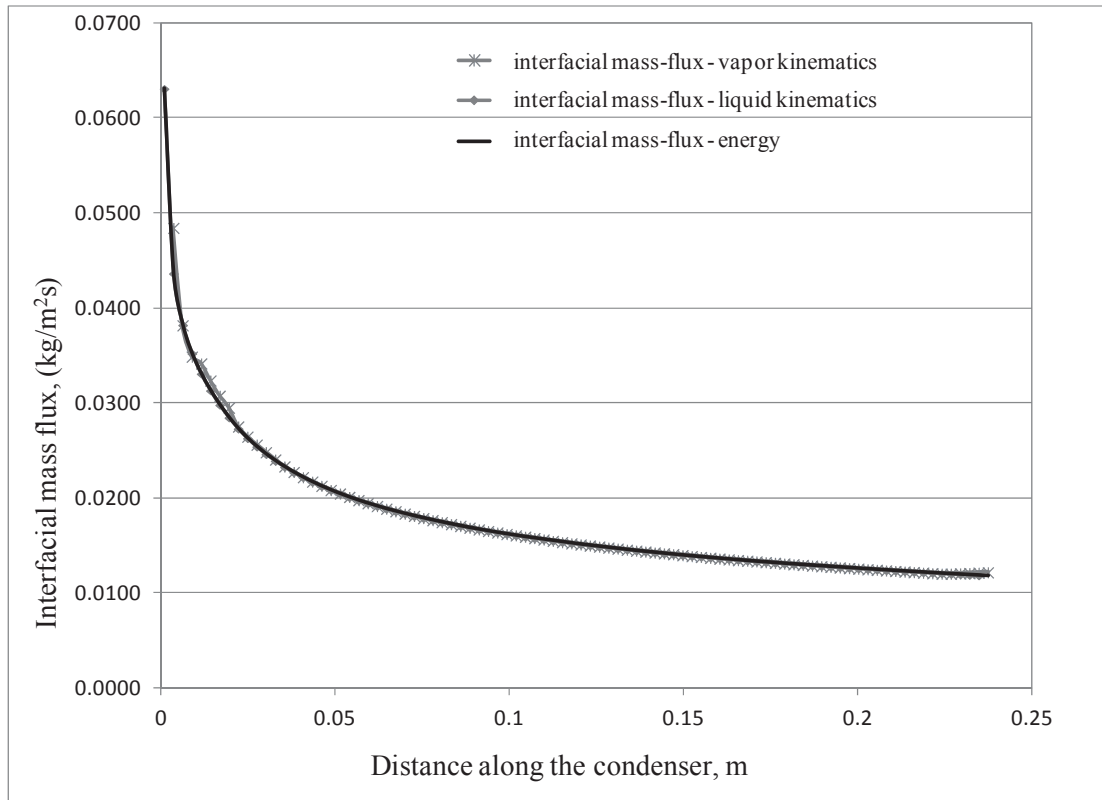


Figure 4.1: Sample convergence plot of interfacial mass-flux terms for a representative internal condensing flow problem.

There is also a need to establish proper grid independence during the development of the computational tool. Grid independence is established for each individual single phase domain and for each iteration. For a given geometry (interface location) and corresponding boundary conditions, different mesh densities are chosen to show the importance of choice of correct refinement. COMSOL allows one to refine a mesh by using predefined refinement levels. To demonstrate grid independence for a single phase domain, for a fixed interface location, default meshing parameters in COMSOL is used to solve the problem at variable refinement levels. For both liquid and vapor domains, the grid quality statistics, number of elements, and solution time is shown in Table 4.1 and their associated solutions are shown in Figs. 4.2a and 4.2b. These default refinements levels mesh the grid in a way that it maintains the minimum element quality of the grid (see (COMSOL Modeling Guide)) as seen in Table 4.1. For example, in liquid domain, for successive refinements, the element size and number of elements are chosen such that the average element quality, and element area ratio are maintained the same. For these refinements, at $x = 0.06$ m, the variation of x-directional velocity, in the liquid domain and in the vapor domain, is plotted for different grid refinement in Fig. 4.2a and Fig. 4.2b respectively. Similar results were obtained at different x-locations as well. For the liquid domain, refinement level of 1 or 2 was maintained for all simulations. Similarly, for vapor domain, refinement level of 3 or 4 was used for all simulations as refinement levels of 0 and 1 are not acceptable and for these refinement levels (0 or 1), the condensing flow problem does not converge.

Earlier code implemented in FORTRAN used a structured quadrilateral grid type for meshing the liquid and vapor domain. However, unlike the quadrilateral grid, this

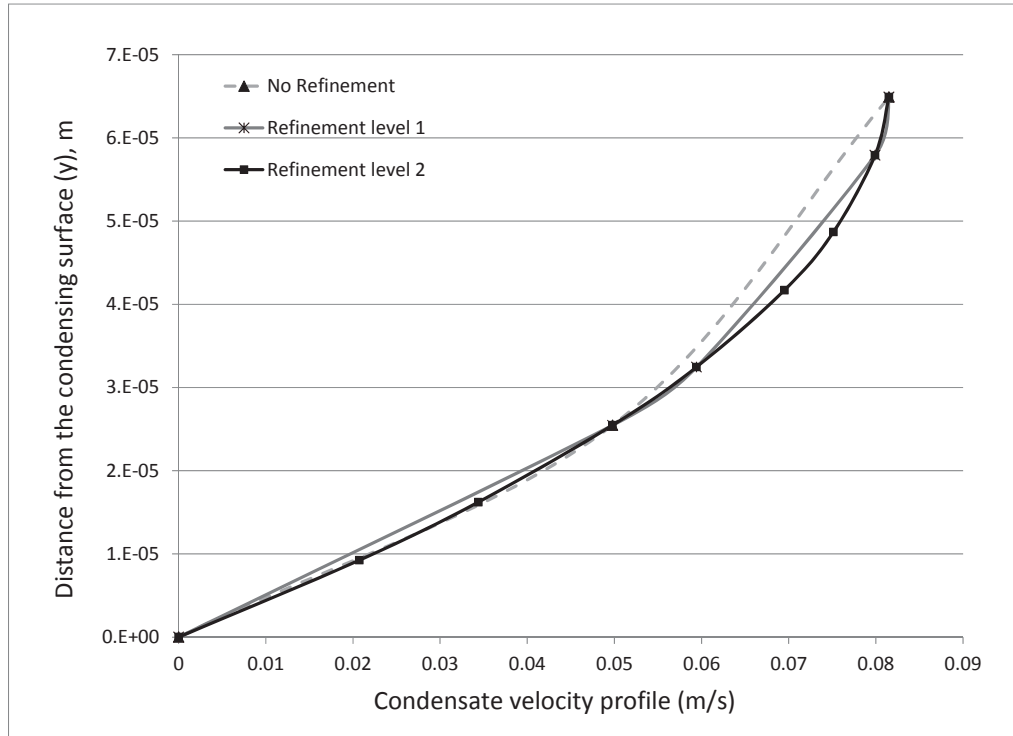
computational tool uses triangular grid for meshing the individual domain. This being the default choice in COMSOL, it helps in maintaining the best grid quality for successive refinements.

While solving a condensing flow problem, one has an option to select either of refinement levels 2, 3, or 4 to grid the vapor domain at each iterative step. Figure 4.3 shows the film thickness solutions for three different refinement levels chosen to solve the vapor domain in a complete condensing flow steady solution. As shown in Fig. 4.3, since solution does not change much with successive refinement, vapor domain is typically solved with the refinement level of 3. Similarly, it is found that the solution for different refinements of liquid domain do not change much, the refinement level for the liquid domain is maintained at level 1, as level 2 takes significantly more time and computational resources.

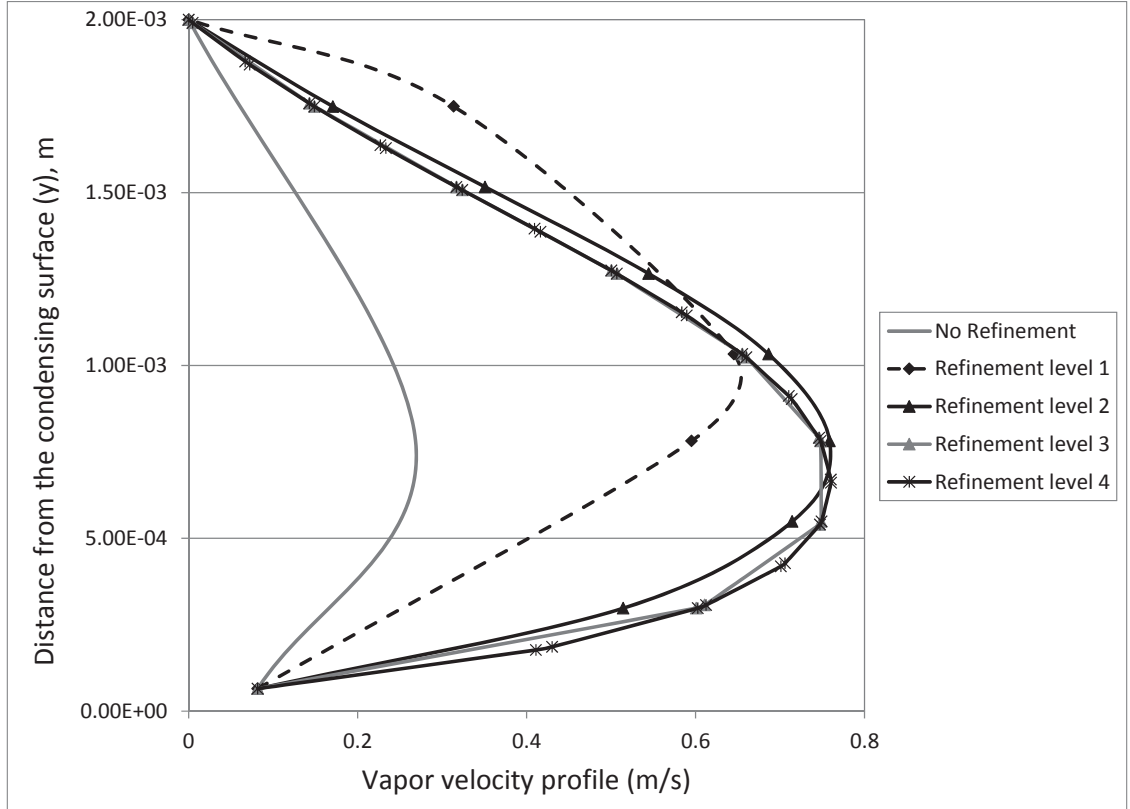
The computation for the full 2-D steady internal condensing flow problem was performed on an Intel Core i7 CPU at 2.67 GHz clock-speed with 12 GB RAM. A powerful graphic accelerator card allows better flow visualization of the solution.

Table 4.1
Grid quality statistics for different refinement levels for liquid and vapor domain.

Domain	Grid No	Refinement	Quality Statistics						Solution Time (s)
			Triangular Elements	Edge Elements	No of Elements	Minimum Element Quality	Average Element Quality	Element Area Ratio	
Liquid	1	0	5882	5882	5882	0.7438	0.8193	0.4627	16
	2	1	23528	11764	23528	0.7438	0.8193	0.4626	50
	3	2	94112	23528	94112	0.7438	0.8193	0.4628	191
Vapor	1	0	76	74	76	0.8193	0.8256	0.3979	2
	2	1	304	148	304	0.8193	0.8256	0.3979	6
	3	2	1216	296	1216	0.8193	0.8256	0.3978	6
	4	3	4864	592	4864	0.8193	0.8256	0.3978	9
	5	4	19456	1184	19456	0.8193	0.8256	0.3978	28



(a)



(b)

Figure 4.2: (a) For a flow of FC-72 in a vertical channel, the figure shows the cross-sectional condensate velocity profile, $u_1(x,y)$ at $x = 0.06$ m for different refinement levels of the mesh. (b) For a flow of FC-72 in a vertical channel, the figure shows the cross-sectional vapor velocity profile, $u_2(x,y)$ at $x = 0.06$ m for different refinement levels of the mesh.

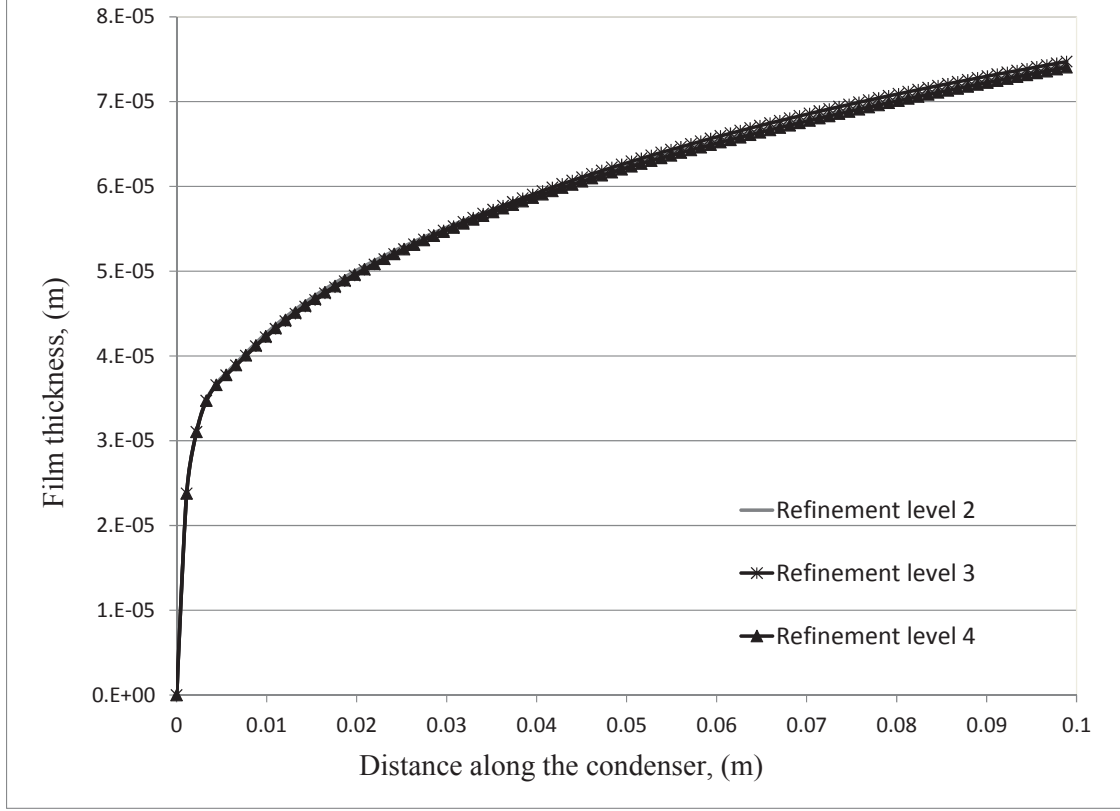


Figure 4.3: For different refinement levels chosen for the vapor domain meshing, the figure shows film thickness profiles obtained from the solution of the complete condensing flow problem.

4.1.2 Accuracy of the One-Dimensional Computational Tool

The convergence, grid independence, and accuracy of the ODE solver are well known, as a well-tested Runge-Kutta solver (MATLAB from The MathWorks, Inc., MA) was used. As mentioned earlier, the 2-D code implemented on FORTRAN is extensively tested and validated Narain et al. 2006; Narain et al. 2007; Narain et al. 2009. It has been used to solve the classical problems of Nusselt Phan et al. 2007 and Koh Kulkarni et al. 2010. Therefore, the results obtained from the earlier code implemented on FORTRAN is

compared with the results obtained from 1-D computational tool and 2-D computational tool to show self-consistency.

For representative cases chosen for both gravity and shear driven flows, agreements between the 1-D steady solution and the corresponding 2-D steady solution's film thickness predictions are demonstrated in Figs. 4.4–4.6. The agreements are good for other flow variables as well. Similar agreement for other flow conditions also exist, but are not shown here. Fig. 4.4 shows film thickness comparison between 1-D solution and 2-D solution obtained from the earlier code implemented on FORTRAN and 2-D code implemented on COMSOL/MATLAB platform for a flow of R113 in a vertical channel, whereas, Fig. 4.5 shows, for the flow of R113 vapor, the film thickness comparison for a shear driven flow in a channel in zero gravity. For a gravity driven flow of FC-72 in a vertical tube, Figure 4.6 compares the flow's solution as obtained by a 2-D (FORTRAN) and the reported 1-D technique. Because of the superior symmetric vapor velocity profile choices (see Eq. (2.25)) that are possible for zero gravity flow in a tube, 1-D solutions yield even better agreement with the nearly exact 2-D techniques than do the asymmetric vapor velocity profile choices for zero-gravity or horizontal channel flow cases (as in Fig. 4.5).

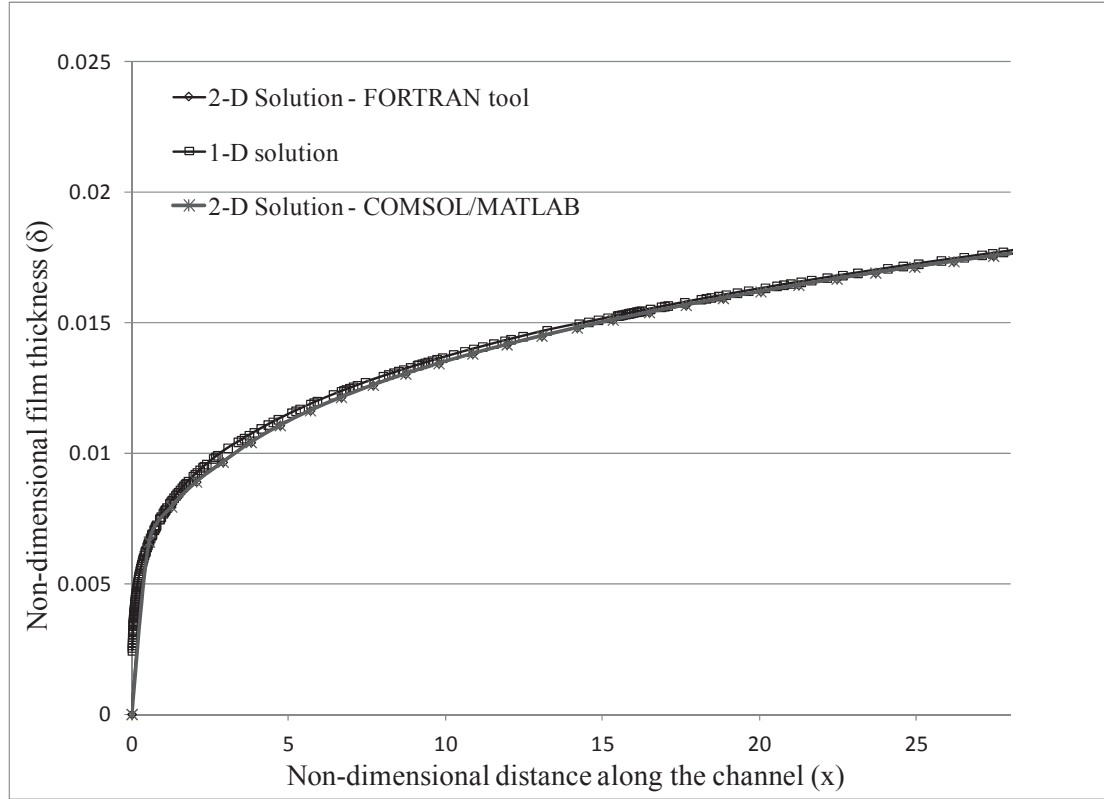


Figure 4.4: The figure compares steady/quasi-steady solutions for a vertical channel. The solutions are obtained by 2-D (FORTRAN code as well as COMSOL/MATLAB platform based code) and 1-D techniques for the flow of R-113 vapor with inlet speed of $U = 0.41$ m/s, $\Delta T = 5$ °C, $h = 0.004$ m, and $g_x = 9.8$ m/s².

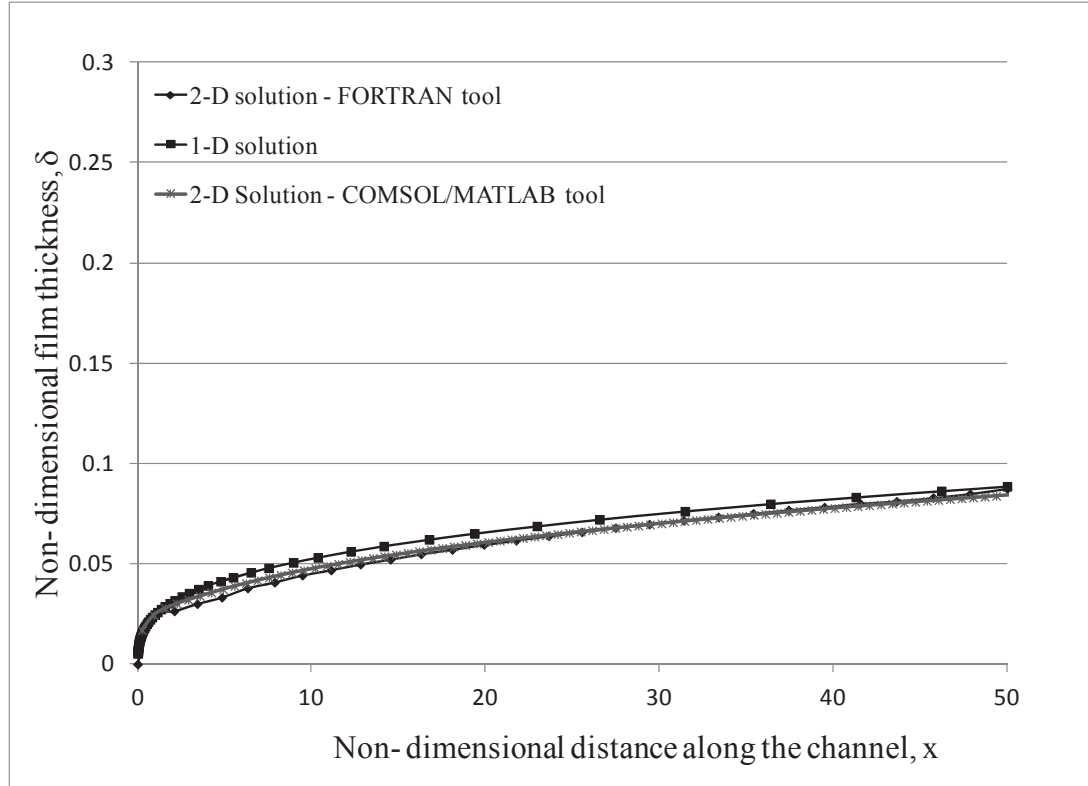


Figure 4.5: The figure compares steady/quasi-steady solutions obtained by 2-D (FORTRAN code as well as COMSOL/MATLAB platform based code) and 1-D techniques for a channel under 0g conditions. The solutions are obtained for a flow of R-113 vapor with inlet speed of $U = 0.6$ m/s, $\Delta T = 5$ °C, and $h = 0.004$ m.

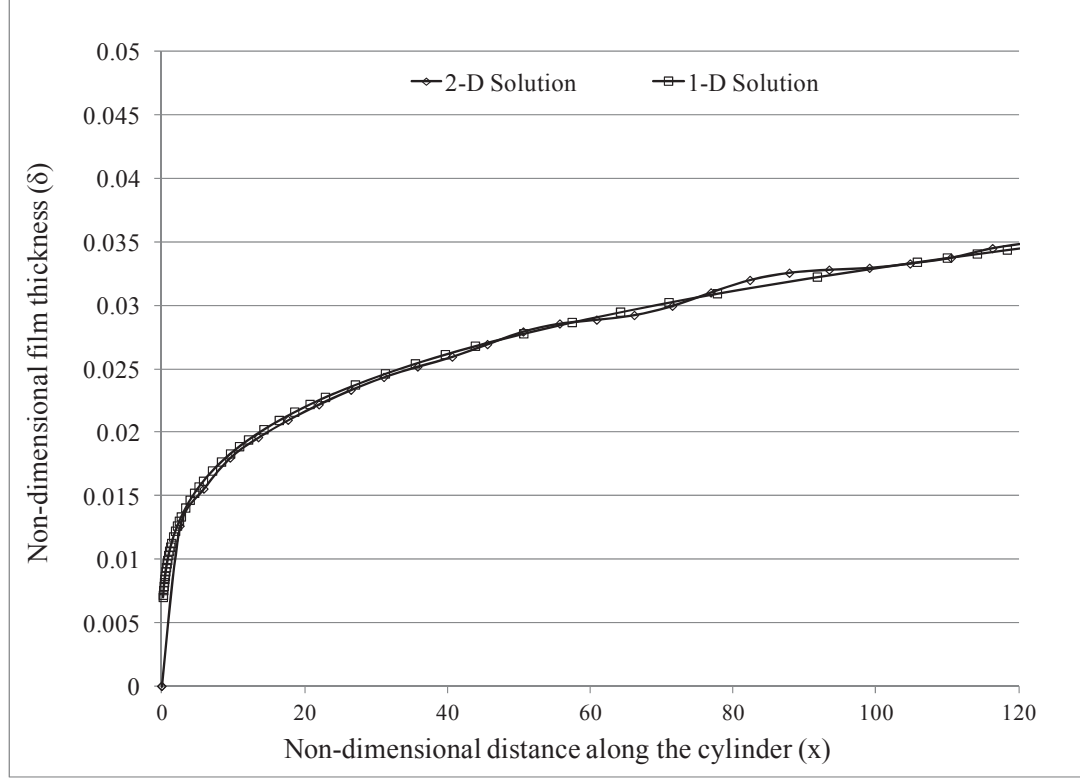


Figure 4.6: The figure compares steady/quasi-steady solutions obtained by 2-D (FORTRAN code) and 1-D techniques for a flow through a vertical cylinder. The solutions are obtained for a flow of FC-72 vapor with inlet speed of $U = 1.5$ m/s, diameter $D = 6.6$ mm, $\Delta T = 9$ °C and $g_x = 9.81$ m/s².

Since this “quasi” 1-D simulation technique is computationally more efficient, it can simulate the flow up to or very near (depending on the underlying issues of flow physics) the point of full condensation with greater ease and lower computational costs. However, only the solutions up to 70 – 80 % of the inlet vapor condensation are considered for the data analysis. This is because, the zone downstream of this point, which is near full condensation may be non-annular (particularly for shear/pressure driven flows) in nature. The results obtained from the two computational tools are compared with each other and the earlier CFD code.

4.2 Validation of the Computational Tools and Synthesis of Experimental Results with Results Obtained from the Computational Tools

After establishing the accuracy and self-consistency of the three computational tools, the results from all or any one of the tools are compared with the experimental results for internal condensing flows. Experimental results for partial and full condensing flows are available for gravity driven flow of FC-72 in a vertical tube and are reported in Kurita et al. 2011. Similarly, experimental results for shear/pressure driven condensing flows in a horizontal channel are available in Kivisalu et al. 2011, and Gorgitrattanagul 2011. The following results show the synthesis between experimental results and computational results for gravity dominated and shear driven flow cases.

4.2.1. Comparisons of Experimental Results with Computationally Obtained Results for Gravity Dominated Condensing Flows in a Vertical Tube and an Inclined Channels

Fully Condensing Flows:

The gravity driven condensing flows' experimental flow loop, test section, its instrumentation, and operating procedures were developed by J. Kurita and M. Kivisalu and are explained in detail in Kurita et al. 2011. The results obtained from these experimental runs are compared with the computational results obtained from the 1-D solution technique and the 2-D computational tool presented here. For ease in presenting the results, a summary of experimental flow loop and test section from Kurita et al. 2011 is presented here. The computationally obtained values of length of full condensation

(x_{FC}) and average heat transfer coefficient obtained for representative experimental runs of gravity driven flows in vertical tube are compared with one another.

Experimental Facility and Setup

The vertical tube condenser test-section, which is shown in Fig. 4.7, is a part of a closed flow loop shown in Fig. 4.8. For fully condensing flows of pure FC-72 vapor inside a vertical cylindrical tube of 6.6 mm diameter and 0.7 m length, the experimental conditions are typically found to be annular to annular wavy.

It has three independent feedback control strategies that can fix and steady the values of: inlet mass flow rate \dot{M}_{in} through active feedback control of the heat input to the evaporator/boiler, condensing surface temperature $T_w(x)$ (uniform or non-uniform) through feedback control of coolant water flow rate and its temperature, and inlet pressure p_{in} through active feedback control of one of the controllable displacement pumps in the set up. The flow in Fig. 4.8 is also especially designed to allow development of procedures under which condensing flows can be allowed to reach steady state while seeking their own self-selected exit conditions (exit quality or pressure). The flow loop in Fig. 4.8 is used to attain full and partially condensing flows. The operating procedure to attain full and partial condensing flows is given in Kurita et al. 2011. However, only fully condensing flow results are compared with results obtained from computational tool.

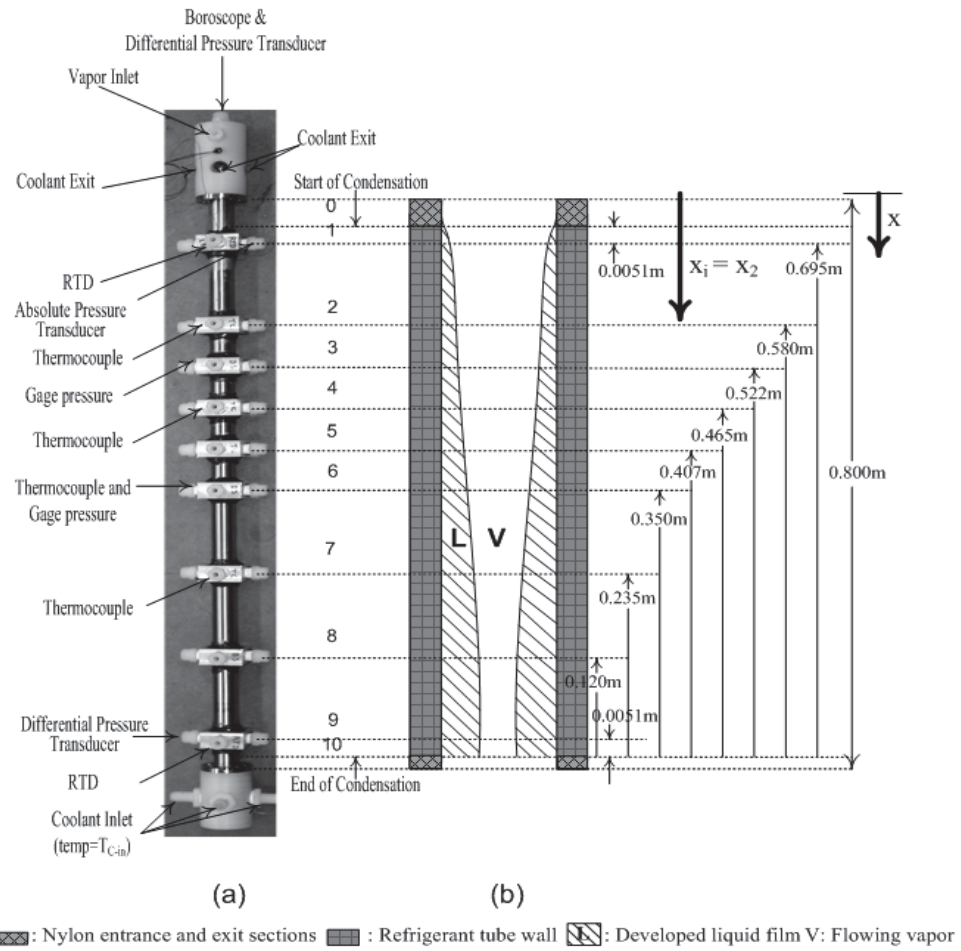


Figure 4.7: (a) The photograph of a condenser test-section. (b) The test-section schematic (diameters in (a) and (b) are not to the same scale). The condensing surface covers the zone $x_0 \leq x \leq x_{10}$.

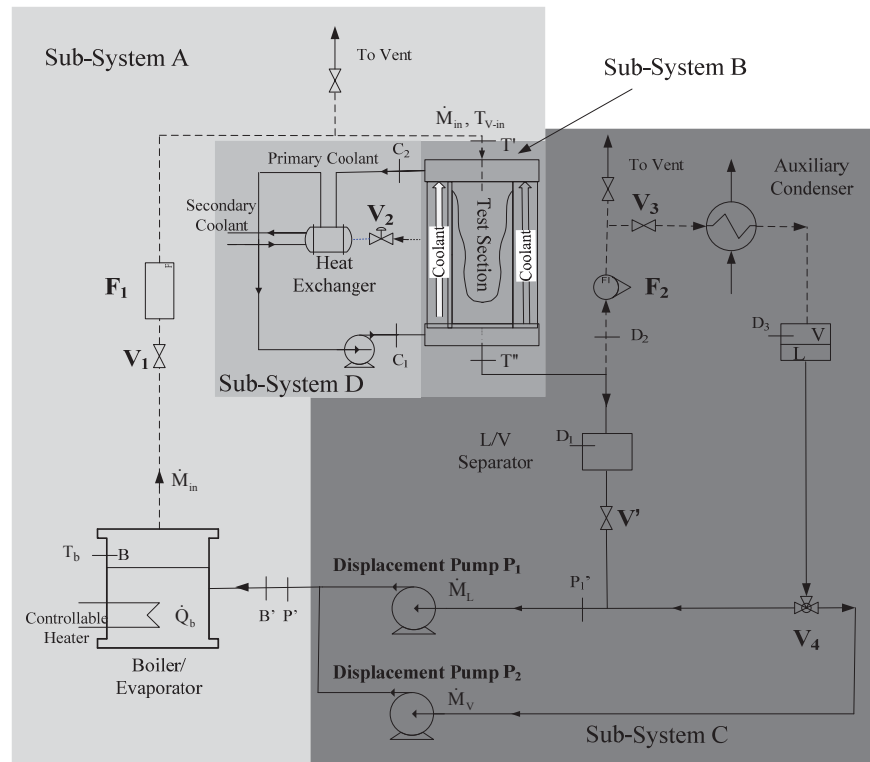


Figure 4.8: The schematic of the flow loop for achieving steady flows for partial or full condensation cases. For full condensation cases, valve V_3 is closed and the auxiliary condenser is not in use.

Table 4.2
Representative experimentally measured data Kurita et al. 2011 and some key calculated and
computed variables for natural fully condensing steady flows.

RunNo	\dot{M}_{in} (g/s)	\bar{T}_w (°C)	ΔT (°C)	P_h (kPa)	P_{dp-3} (kPa)	P_{dp-6} (kPa)	P_{dp-9} (kPa)	x_{TC-Exp} (m)	x_{TC-Sim} (m)	ρ_2/ρ_1	μ_2/μ_1	G (kg/m ² s)	Re	\dot{Q}_{out} (J/s)	\bar{q}'' (W/m ²)	\bar{h}_{exp} (W/m ² K)	\bar{h}_{sim} (W/m ² K)
Error	± 0.05	± 0.9	± 1.7	± 0.15	± 0.15	± 0.15	± 0.27	% Error mean max ±11% ±27%	(m)	± 0.0010	± 0.0039	% Error mean max ±34% ±66%	% Error mean max ±21% ±25%	% Error mean max ±13% ±20%	% Error mean max ±22% ±37%	% Error mean max ±25% ±34%	
1	0.25	296	12.8	47.67	49.52	52.24	57.41	0.107	0.111	0.0039	0.0164	7.31	4426	22.71	10278	804	775
2	0.25	296	9.0	40.77	42.01	44.72	49.83	0.149	0.159	0.0033	0.0157	7.31	4479	22.97	7423	820	769
3	0.25	295	5.6	33.69	34.23	36.25	41.28	0.238	0.259	0.0028	0.0149	7.31	4540	23.26	4705	836	768
4	0.25	295	5.0	32.29	32.82	34.25	39.26	0.276	0.293	0.0027	0.0147	7.31	4557	23.34	4085	819	771
5	0.25	295	4.5	31.65	32.20	33.47	38.46	0.285	0.326	0.0026	0.0147	7.30	4559	23.34	3944	867	760
6	0.25	295	4.3	31.31	31.86	32.85	37.84	0.302	0.339	0.0026	0.0146	7.30	4563	23.36	3725	862	770
7	0.25	295	4.1	30.92	31.48	32.37	37.36	0.308	0.356	0.0026	0.0146	7.31	4571	23.40	3661	903	783
8	1.00	296	10.3	43.09	43.78	43.66	43.14	0.694	0.895	0.0035	0.0160	29.22	17836	91.50	6389	617	478
9	1.00	296	11.2	44.82	45.51	45.39	45.06	0.683	0.816	0.0037	0.0161	29.23	17793	91.30	6449	576	482
10	1.00	296	12.0	46.54	47.23	47.09	47.42	0.644	0.764	0.0038	0.0163	29.23	17740	91.03	6816	569	480
11	1.00	296	12.8	48.26	48.94	48.80	49.67	0.612	0.711	0.0039	0.0165	29.22	17684	90.75	7150	560	482
12	1.00	297.2	16.9	58.61	59.34	59.27	62.38	0.469	0.528	0.0048	0.0174	29.25	17441	89.50	9203	543	483
13	1.00	306.1	17.5	82.74	83.40	83.14	86.62	0.459	0.508	0.0066	0.0204	29.26	16971	86.90	9125	521	480
14	1.00	303	42.4	165.48	166.07	168.67	174.33	0.159	0.186	0.0138	0.0246	29.25	15967	80.53	24397	575	492

Experimental Range and Results

The experimental results that show key details of the representative flow runs were obtained by J. Kurita for the fully condensing flows and are given in Table 4.2. These results were obtained by the flow loop arrangement in Fig. 4.8 and the procedures 1 and 2 described in section 2.2 of Kurita et al. 2011. The experimental runs reported in Table 4.2 cover only a portion of the non-dimensional parameter space (\tilde{x} , Re_{in} , $G_p \equiv ((\rho_2^2 g_x D_h^3) / \mu_2^2)$, Ja/Pr_1 , ρ_2/ρ_1 , μ_2/μ_1) that governs this in-tube problem. With distance x from the inlet satisfying the constraints $0 \leq x \leq x_{FC}$ for full condensation cases considered here, the remaining non-dimensional parameters cover the zones shown in Figs. 5b – c of Kurita et al. 2011. The experiments were conducted for mass flux over a range of $2.9 \text{ kg/m}^2\text{-s} \leq G \leq 87.7 \text{ kg/m}^2\text{-s}$, temperature difference ΔT of 5°C to 45°C , and length of full condensation x_{FC} in the range of $0 < x_{FC} < 0.7 \text{ m}$. The ranges of the non-dimensional numbers involved in Figs. 5b – c of Kurita et al. 2011 are:

$$\begin{aligned} 0.0025 < \rho_2/\rho_1 < 0.11 \\ 0.015 < \mu_2/\mu_1 < 0.025 \\ 471000 < G_p < 9510000 \\ 0.004 < Ja/Pr_1 < 0.069 \end{aligned} \tag{4.1}$$

It should be noted that the ability to cover a limited range of ρ_2/ρ_1 and μ_2/μ_1 values in Fig. 5c of Kurita et al. 2011, results from the fact that $\Delta T \equiv T_{Sat}(p_{in}) - \bar{T}_W$ was systematically changed by changing the inlet pressure p_{in} and the representative vapor properties change when $T_{Sat}(p_{in})$ changes.

Comparison of length of full condensation (x_{FC})

It was observed that, for the chosen and reported values of \dot{M}_{in} and $\Delta T \equiv T_{Sat}(p_{in}) - \bar{T}_W$, the flow self-selected an effective point of full condensation whose distance x_{FC} from the inlet was such that $0 < x_{FC} < L$ and the test-section was filled with liquid downstream of the point/zone of full condensation. Most gravity driven vertical tube flows visually appeared to be annular wavy up to some point x_A close to the point x_{FC} ($> x_A$) of full condensation. In other words, annular gravity dominated flows are robust and loss of annularity is not a significant phenomenon for such flows. The length ($x_{FC} - x_A$) of the non-annular zone could not be quantified but appeared small and somewhat dependent on flow conditions. The experimental value of x_{FC} is calculated by a technique described in Kurita et al. 2011 which uses the knowledge of pressure transducer readings at x_1 , x_3 , x_6 , and x_9 (shown in Fig. 4.7). The experimental results given in Table 4.2 for these “self-selected/natural” fully condensing flows show a hydrostatic component in absolute pressure readings at transducer locations below the point of full condensation. For most cases considered here, $x_{FC} < x_9 < L$, and therefore there is always a hydrostatic component of pressure at location - x_9 in Fig. 4.7. This implies:

$$p_{in} - p_{x9} = (p_{in} - p_{x_{FC}}) + (p_{x_{FC}} - p_{x9}) \cong (p_{in} - p_{x_{FC}}) + \rho g(x_{FC} - x_9) . \quad (4.2)$$

Because both the reported experiments in Kurita et al. 2011 and associated theory in Mitra et al. 2011 confirm that, for most cases, the pressure differences in the two-phase (mostly) annular region is negligible compared to the hydrostatic pressure (i.e. $|p_{in} - p_{x_{FC}}| \ll |\rho g(x_{FC} - x_9)|$), Eq. (4.2) simplifies to:

$$p_{in} - p_{x9} \cong \rho g(x_{FC} - x_9) \quad (4.3)$$

Because the left side of Eq. (4.3) is available from the experimental results, Eq. (4.3) is used to obtain experimental estimates for x_{FC} , the distance between the inlet and the effective point of full condensation. Furthermore the computational solution approach described here gives - under the assumption of nearly smooth interface, steady laminar vapor flow (in the near interface zone) and laminar condensate flow - direct theoretical estimates for x_{FC} and $(p_{in} - p_{x-FC})$ values. Cases for which the 1-D prediction tool does not allow (or is not valid) one to go right up to 100% condensation, the theoretical estimate for x_{FC} is obtained by extrapolating from the theoretically obtained distances for 80 – 90% condensation of the incoming vapor. Although predictions of $|(p_{in} - p_{x-FC})|$ is off (as it should be – given the impact of interfacial waves and vapor turbulence on this variable), its order of magnitude is correct and, therefore it is found that the right side of Eq. (4.3) correctly approximates the right side of Eq. (4.2).

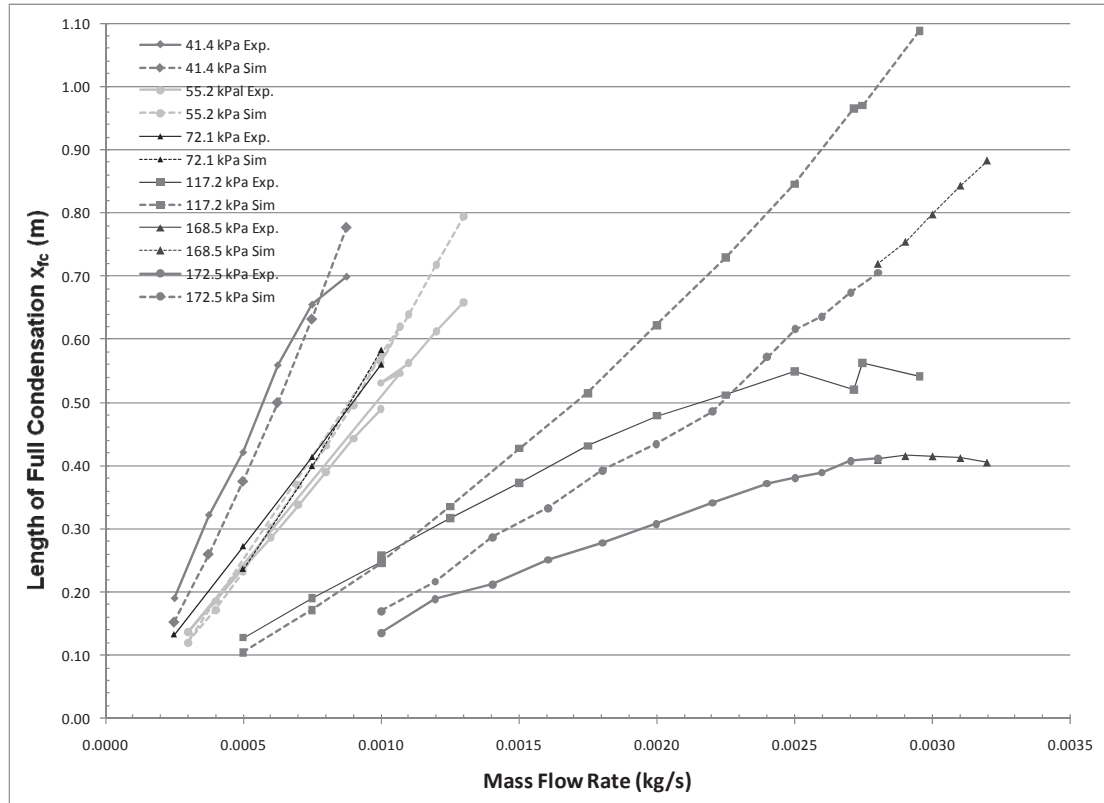


Figure 4.9: The comparison of theoretically and computationally obtained values of x_{FC} as a function of M_{in} . Here the dashed lines indicate the simulation results and the solid lines indicate the experimental results.

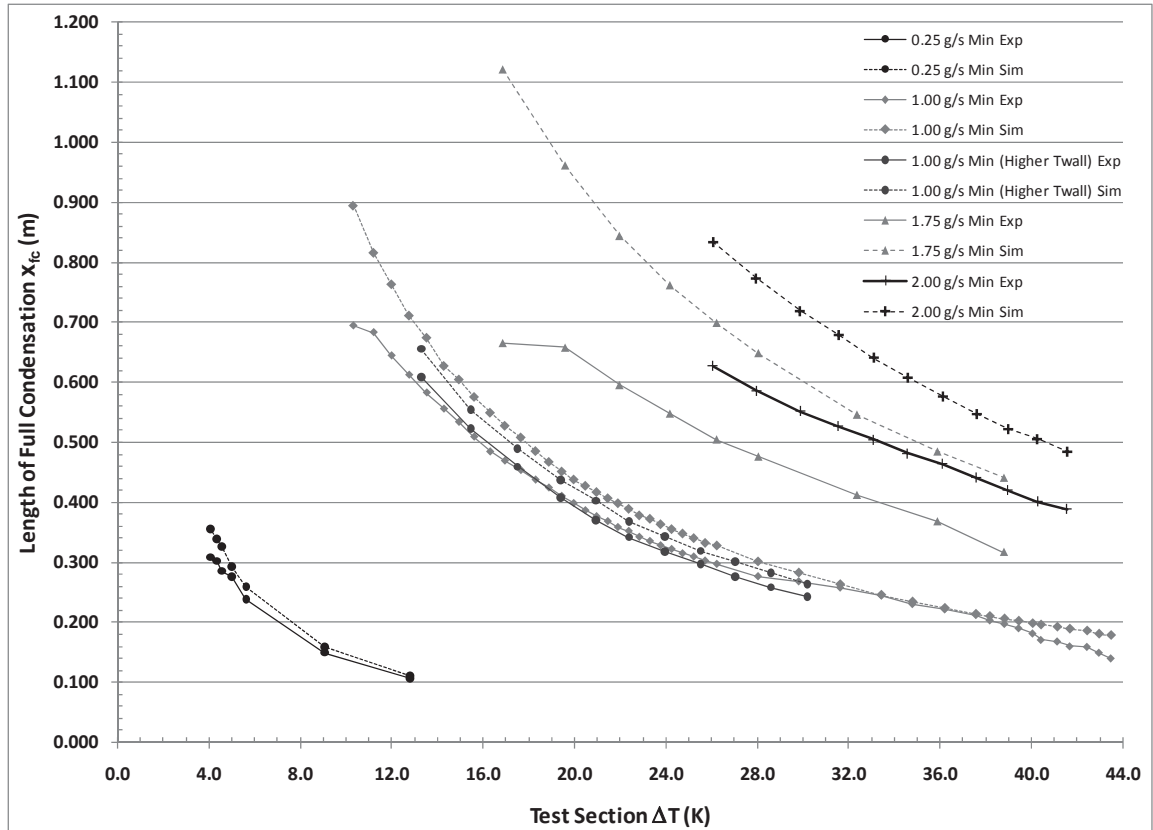


Figure 4.10: The comparison of theoretically and computationally obtained values of x_{FC} as a function of ΔT . Here the dashed lines indicates the simulation results and the solid lines indicate the experimental results.

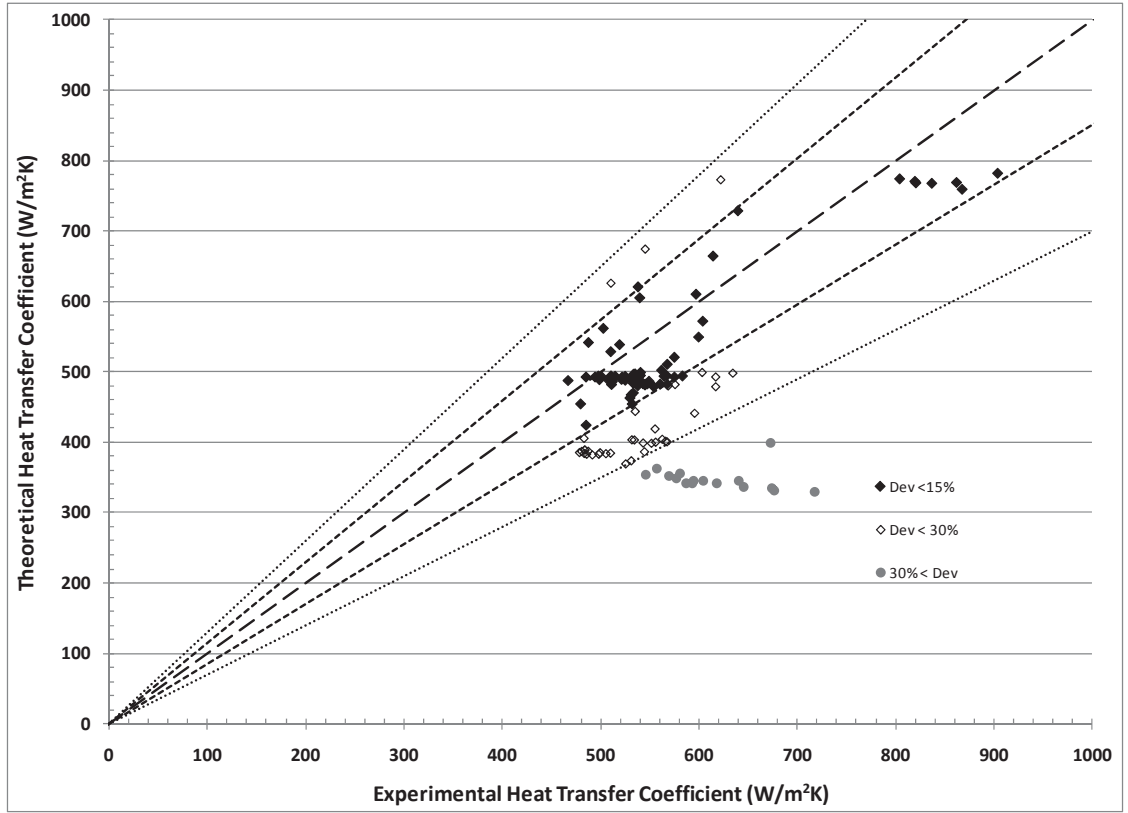


Figure 4.11: Comparison of experimentally and computationally obtained values of average heat transfer coefficients for fully condensing flows.

As shown in Figs. 4.9-4.11, whenever the laminar vapor/laminar condensate assumption is adequate, there is an excellent agreement (within 3 - 4%) between theoretical and experimental estimates of x_{FC} . Equivalently, because of Eq. (4.3) we also have an agreement between experimental and theoretical estimates of $\Delta p \equiv (p_{x9} - p_{in})$. In Figs. 4.9-4.10, the reported plots show the functional dependence structure of $x_{FC} = x_{FC}(\dot{M}_{in}, \Delta T)$ as one of the two variables (\dot{M}_{in} or ΔT) is varied while the other is held fixed. Figures 4.9-4.10 show the cases for which the experimentally calculated x_{FC} starts becoming significantly smaller than the theoretically calculated x_{FC} at larger values of \dot{M}_{in} and ΔT . Therefore, Figs. 4.9-4.10, provide us with a good opportunity to

experimentally obtain and develop a quantitative criteria as to when the near interface region of the vapor flow starts interacting strongly with laminar waviness or turbulence of the condensate in the near interface region. A reasonable procedure for quantifications of these effects, that appear to be the most probable cause (given the videos show the annularity of these flows) for theory and experiment to deviate from one another, is described in section 4 of Kurita et al. 2011.

Comparison of heat transfer coefficient:

For fully condensing flows, the experimental value of the average heat-transfer coefficient \bar{h} (or \bar{h}_{Exp}) is obtained from Eq. (4.4) below. For this, the experimental estimates of \dot{M}_{in} , x_{FC} , and $\Delta T \equiv T_{\text{Sat}}(p_{\text{in}}) - \bar{T}_{\text{W}}$ are used in Eq. (4.4).

$$\dot{Q}_{\text{out}} \approx \dot{M}_{\text{in}} h_{\text{fg}} = (\pi D \cdot x_{\text{FC}} \cdot \bar{h}) \Delta T \quad (4.4)$$

The theoretical value of the average heat-transfer coefficient \bar{h} (or \bar{h}_{Sim}) is obtained by employing the computationally obtained values for the distance x_{FC} in Eq. (4.4). The resulting value of \bar{h}_{Sim} is found to be equivalent, or nearly the same, as the one obtained from the relationship:

$$\bar{h} \cong \frac{k_1}{x_{\text{FC}}} \cdot \int_0^{x_{\text{FC}}} \frac{1}{\Delta(x)} \cdot dx \quad (4.5)$$

where the film thickness $\Delta(x) \equiv D \cdot \delta(x)$ and the expression on the right of Eq. (4.5) is evaluated by the computational solution approach described here.

The full condensation runs/cases allows comparison of theoretically and experimentally obtained values of the average heat-transfer coefficient \bar{h} . These comparisons are shown in Fig. 4.11. In Figs. 4.11, most of the experimental data, that agree well (i.e. within 15%) with the theoretical models presented here, are found to correspond to gravity dominated flows for which the Nusselt correlations in Nusselt 1916 is adequate.

Besides the vertical tube experimental results discussed in Kurita et al. 2011, relevant experimental results obtained from the slightly tilted (“so called” horizontal) channel also meet the requirement of having a condensate motion that is annular/wavy, laminar/laminar, and gravity dominated (as in Nusselt 1916).

Partially Condensing Flows

Partially condensing flow experiments conducted by Lu et al. 1995 were intended to be for a horizontal channel but only later the authors realized that the bottom-surface of the condenser had a 0.5 to 1° tilt. Therefore, one should be careful in concluding that horizontal channel experimental data for hydraulic diameters that are mm scale or larger are always “shear driven” cases. This may not be the case because if the experimental arrangement shows even $\pm 1/2^\circ$ or more inclination, interfacial shear forces on the condensate become quite weak (if $D_h \geq 4$ mm for the flows considered here) relative to the more dominant gravitational forces.

Because of the above described sensitivity/limitations with large hydraulic diameter horizontal channel condensing flows, it was found that the large hydraulic diameter rectangular cross-section ($w = 40$ mm, $h = 25$ mm) test-section of 0.9 m length used in the experiments of Lu et al. 1995 do not relate to the intended investigations of purely

shear driven cases. In fact the results are in near perfect agreement with entirely gravity driven or gravity dominated cases. This observation follows from the hypothesis that the experimental uncertainties caused their channel's bottom condensing-surface (see Fig. 2.1) to be tilted downward by an angle of $\alpha = 1^\circ$. The comparisons between the condensing flow theory and experiments under this hypothesis for their runs Lu et al. 1995 are presented in Table 4.3. A private correspondence of Dr. Narain with the senior author of Lu et al. 1995 also states that they only ensured the *horizontalness* of the top surface of their test-section and that the condensing-surface itself might have had a 1° downward tilt. Therefore, when the condensing-surface in the experiments reported in Lu et al. 1995 is assumed to have an unintended downward inclination of $\alpha = 1^\circ$ (see Fig. 2.1), most of their data is in excellent agreement with the computational theory. The discovery of this error as reported in Mitra et al. 2011, was obtained by R. R. Naik while using the 1-D computational tool presented here. Under this assumption, the comparison of their film thickness and average heat transfer coefficient data is shown in Table 4.3 for representative flows of FC-72 and in Table 4.4 for representative flows of R113. The values of $h_t \equiv \dot{Q} / (A.\Delta T)$, where \dot{Q} is total heat removal (in W) for a condensing-surface area of $A = 0.04 \text{ m}^2$

Lu et al. 1995 data are also close to the gravity dominated Nusselt regime Nusselt 1916. Hence, the agreement of their data with the Nusselt result is also quite good (though not as good as the full theory). Lu et al. 1995 experimental runs involved only partial condensation and hence heat transfer rates were calculated from Eq. (1) in Kurita et al. 2011 with Table 4.3's parameter space corresponds to the non-dimensional parametric space of:

$$9285.3 \leq Re_{in} \leq 35284.7, 0.0243 \leq Ja/Pr_1 \leq 0.0909, 0.0080 \leq \rho_2/\rho_1 \leq 0.0086$$

$$0.0459 \leq \mu_2/\mu_1 \leq 0.0472, 3198304 \leq G_p \leq 3651997 \quad (4.6)$$

and Table 4.4's parameter space being

$$5358.71 \leq Re_{in} \leq 28918.56, 0.0130 \leq Ja/Pr_1 \leq 0.0275, 0.0047 \leq \rho_2/\rho_1 \leq 0.0057$$

$$0.0171 \leq \mu_2/\mu_1 \leq 0.0226, 1122008 \leq G_p \leq 1518915 \quad (4.7)$$

A graphical comparison of average heat transfer coefficient obtained by their experiment Lu et al. 1995 and the computational theory is presented in Fig. 4.12.

Table 4.3
Comparison of experimental results of Lu et al. 1995 for FC-72 vapor with computationally obtained results for an inclined channel with 1° inclination.

Run	M_{in}	ΔT	Film Thickness - Experimental, (mm) at different x, (mm)					Film Thickness - Computational, (mm) at different x, (mm)					h_{i-exp}	h_{i-comp}	h_{i-Nu}
	$\times 10^3$ (kg/s)	(°C)	x = 50.8	x = 152.4	x = 254	x = 457.2	x = 812.2	x = 50.8	x = 152.4	x = 254	x = 457.2	x = 812.2	(W/m ² .°C)	(W/m ² .°C)	(W/m ² .°C)
322	4.77	20.26	0.24	0.32	0.34	0.34	0.37	0.19	0.25	0.29	0.33	0.38	150.84	184.12	165.55
317	6.29	30.23	0.27	0.40	0.40	0.41	0.42	0.21	0.27	0.31	0.36	0.42	160.15	169.95	153.04
321	6.73	19.67	0.20	0.31	0.32	0.34	0.36	0.19	0.25	0.28	0.33	0.38	176.47	185.90	166.67
313	7.87	31.37	0.24	0.37	0.41	0.42	0.44	0.21	0.27	0.31	0.36	0.42	154.41	169.09	151.74
320	7.73	19.86	0.19	0.32	0.33	0.34	0.36	0.19	0.25	0.28	0.33	0.38	169.64	185.53	166.23
312	8.15	40.86	0.22	0.40	0.46	0.48	0.51	0.22	0.29	0.33	0.38	0.44	157.52	161.62	145.19
319	9.06	20.47	0.18	0.29	0.32	0.34	0.37	0.19	0.25	0.29	0.33	0.38	168.60	184.31	165.12
331	9.16	10.53	0.17	0.24	0.26	0.27	0.28	0.16	0.22	0.25	0.29	0.33	195.85	213.33	190.52
311	10.89	41.12	0.21	0.36	0.43	0.48	0.50	0.22	0.29	0.33	0.38	0.44	164.07	161.80	145.01
345	11.23	40.58	0.22	0.35	0.42	0.46	0.48	0.22	0.29	0.33	0.38	0.44	167.19	162.29	145.43
314	11.21	30.81	0.23	0.30	0.37	0.40	0.44	0.21	0.27	0.31	0.36	0.42	164.71	170.21	152.32
346	11.64	28.21	0.21	0.30	0.37	0.39	0.40	0.20	0.27	0.30	0.35	0.41	182.64	173.82	155.43
301	12.29	47.58	0.29	0.39	0.39	0.42	0.53	0.22	0.29	0.33	0.39	0.45	143.56	158.31	141.89
323	12.77	20.12	0.17	0.27	0.30	0.32	0.34	0.19	0.25	0.28	0.33	0.38	181.91	185.86	165.85
324	14.57	20.32	0.17	0.28	0.28	0.29	0.34	0.19	0.25	0.29	0.33	0.38	197.49	185.37	165.21
315	15.68	29.88	0.19	0.28	0.33	0.37	0.37	0.20	0.27	0.31	0.36	0.41	211.63	172.48	153.88
325	17.13	19.99	0.20	0.28	0.30	0.31	0.31	0.19	0.25	0.28	0.33	0.38	218.08	186.41	165.83

Table 4.4
Comparison of experimental results of Lu and Suryanarayana for R113 vapor with computationally obtained results for an inclined channel with 1° inclination.

Run	M_{in} * 10 ³ (kg/s)	ΔT (°C)	Film Thickness - Experimental, (mm) at different x, (mm)					Film Thickness - Computational, (mm) at different x, (mm)					h_{exp} (W/m ² ·°C)	h_{comp} (W/m ² ·°C)	h_{Nu} (W/m ² ·°C)
			x = 50.8	x = 152.4	x = 254	x = 457.2	x = 812.2	x = 50.8	x = 152.4	x = 254	x = 457.2	x = 812.2			
221	2.45	21.42	0.19	0.32	0.35	0.39	0.44	0.23	0.30	0.35	0.40	0.46	190.18	202.76	181.94
220	2.58	31.21	0.25	0.38	0.40	0.46	0.51	0.26	0.34	0.38	0.45	0.51	184.61	184.93	165.88
100	3.19	14.76	0.31	0.35	-	0.38	0.38	0.21	0.27	0.31	0.36	0.42	205.50	222.52	199.26
180	4.17	33.83	0.30	0.36	0.41	0.43	0.47	0.26	0.34	0.39	0.45	0.52	188.91	181.03	162.91
181	3.99	21.42	0.19	0.29	0.32	0.34	0.40	0.23	0.30	0.34	0.40	0.46	209.36	203.12	182.05
182	4.37	14.15	0.23	0.26	0.28	0.32	0.36	0.20	0.27	0.31	0.35	0.41	220.96	224.89	201.58
202	5.32	32.19	0.22	0.34	0.41	0.44	0.48	0.26	0.34	0.38	0.45	0.52	190.57	183.77	164.91
201	5.22	39.79	0.26	0.37	0.42	0.44	0.50	0.28	0.36	0.41	0.48	0.56	192.00	173.90	156.23
203	5.29	20.11	0.17	0.28	0.31	0.34	0.41	0.28	0.36	0.41	0.48	0.56	218.14	173.90	184.67
225	5.45	38.71	0.24	0.38	0.44	0.47	0.52	0.27	0.36	0.41	0.48	0.55	188.79	175.19	157.19
207	6.60	31.62	0.18	0.29	0.34	0.40	0.43	0.26	0.34	0.39	0.45	0.52	204.04	184.56	165.37
208	6.82	22.28	0.15	0.30	0.34	0.37	0.40	0.23	0.31	0.35	0.40	0.47	214.40	201.49	180.22
195	7.42	38.28	0.18	0.32	0.37	0.42	0.47	0.27	0.36	0.41	0.47	0.55	209.23	176.08	157.68
211	8.43	21.20	0.13	0.27	0.30	0.37	0.40	0.23	0.30	0.34	0.40	0.46	244.53	204.37	182.32
223	9.51	37.03	0.17	0.29	0.36	0.42	0.50	0.27	0.35	0.40	0.47	0.54	217.38	177.88	159.03
213	9.86	39.73	0.15	0.30	0.37	0.44	0.53	0.27	0.36	0.41	0.48	0.55	215.20	174.88	156.36
215	9.76	21.65	0.11	0.20	0.25	0.35	0.38	0.23	0.30	0.35	0.40	0.46	228.93	203.61	181.36
206	13.21	30.95	0.17	0.28	0.34	0.38	0.41	0.25	0.33	0.38	0.44	0.51	257.44	186.82	166.26

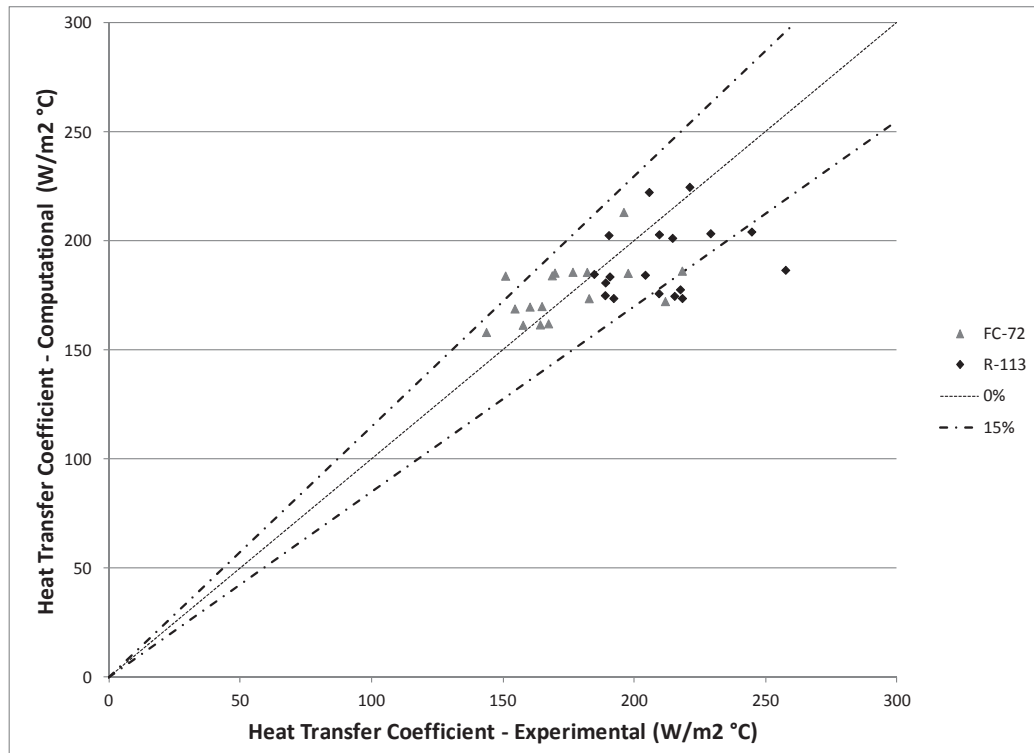


Figure 4.12: The figure graphically presents the nature of agreement between theoretically and experimentally Lu et al. 1995 obtained values of average heat-transfer coefficient.

4.2.2 Comparisons of Experimental Results with Computationally Obtained Results for Shear Driven Condensing Flows in a Horizontal Channel

Purely shear driven flows occur in 0g, in the horizontal channel configuration of Fig. 2.1 (with $\alpha = 0$ and $g_y = -9.81 \text{ m/s}^2$), and, as shown later, in the μm -scale duct geometries of modern interest.

The shear driven horizontal channel condensing flows' experimental flow loop, test section, its instrumentation, and operating procedures were developed by M. Kivisalu and Nook G. and are explained in detail in Kivisalu et al. 2011 and Gorgitrattanagul 2011. The reported experimental results are for annular zones of fully condensing flow of pure FC-72 vapor. The flow condenses on the horizontal condensing surface (316 stainless steel) which is the bottom surface (wall) of a rectangular cross-section duct of 2 mm height, 15 mm width, and 1 m length. The sides and top of the duct are made of clear plastic for flow visualization. The test section and its instrumentation is shown in Fig. 4.13.

The results obtained from these experimental runs Gorgitrattanagul 2011 are compared with the computational results obtained from 2-D computational tool with $g_y = -9.81 \text{ m/s}^2$ and actual wall temperature variations recorded during the experiments.

A comparison with an experimental heat flux data and detailed computational predictions for a sample run of shear driven condensing flow in a horizontal channel with the $T_w(x)$ variation as shown in Fig. 4.14 is done. These comparisons are shown in Figs. 4.15 – 4.17. Additional comparative runs of similar nature are given in Table 4.5. For a representative run involving annular FC-72 condensation in the test-section of Fig. 4.13,

one has inlet mass flow rate $\dot{M}_{in} = 0.698$ g/s, inlet pressure $p_{in} = 100$ kPa, the length of the annular regime $x_A \approx 95$ cm, and condensing-surface temperature $T_w(x)$ over $0 \leq x \leq x_A$ as depicted in Fig. 4.14. Thus the controlling value of representative temperature-difference $\Delta T = T_{sat} - T_w$ is 5.9 °C. Additional experimental observations are: (i) the value of heat-flux measured by a heat-flux meter (from Vatel Corporation as discussed in Kivisalu et al. 2011) at $x = 40$ cm is 0.14 W/cm², (ii) flow visualization results, as in Fig. 6 of Kivisalu et al. 2011, confirming the nature of the annular and the non-annular regimes (over $x \geq x_A$), and (iii) the pressure-difference $\Delta p_{40} = 50$ Pa as measured by a differential pressure transducer between $x = 0$ and $x = 40$ cm.

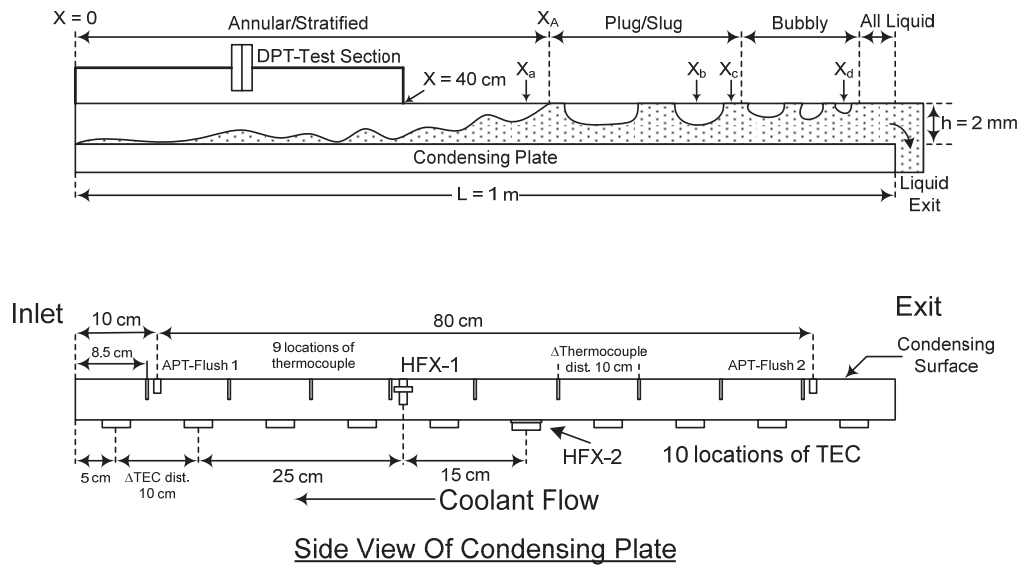


Figure 4.13: Side views of: (a) test-section, and (b) instrumented condensing plate

The computational predictions for this sample run, using the 2-D scientific approach (with $g_y = -9.81$ m/s²) presented in this thesis, are shown in Figs. 4.15 – 4.17. Figure 4.15 shows the mean liquid film thickness $\Delta(x)$ with x for over $0 \leq x \leq x_A$. Figure 4.16 shows the corresponding heat-flux, q''_w , variations with x over $0 \leq x \leq x_A$ and the fact that the

experimentally measured heat-flux values at $x = 40$ cm are within 25 % of the computational predictions. Figure 4.17 shows variations, with downstream distance x , of the cross-sectional values of the liquid flow rate $\dot{M}_L(x)$ and the vapor flow rate $\dot{M}_V(x)$.

For different experimental runs, a set of comparisons of heat-flux values at $x = 40$ cm obtained from 2-D computational tool with actual $T_w(x)$ variations and the experimentally measured value of heat-flux is shown in Table 4.5. For the range of cases involving low to moderate interfacial waviness associated with inlet Reynolds number $Re_{in} \leq 12,500$ (with FC-72 and ΔT in 5 to 16 °C range), the agreement of the 2-D simulation tool with heat-flux value at $x = 40$ cm is quite good. Note that, as discussed for gravity assisted condensing flows Kurita et al. 2011, the vapor flow laminarizes in the vicinity of the slow moving condensate (because of bending streamlines and negligible x -component of vapor velocity). However, for horizontal shear/pressure driven annular condensing flows, the condensate momentum is much smaller and, as a result, the re-laminarization in far field turbulence is slower because of a slow reduction in cross-sectional vapor flow rate $\dot{M}_V(x)$. Despite the absence of increasing possibility of condensate turbulence, as is the case with some gravity driven flows Kurita et al. 2011, the flow sensitivity to interfacial waviness is higher and this waviness is visually seen to increase for the $Re_{in} \geq 17,500$ (with FC-72 and ΔT in 9 to 15 °C range) cases in Table 4.5. Since the condensate motion is entirely shear driven, the impact of the condensate motion on heat-flux values that arise from waves and ever-present noise from the wall or active devices in the loop is quite significant for horizontal or 0g flows. Under these sensitive conditions, the agreement seen in Table 4.5 is remarkable.

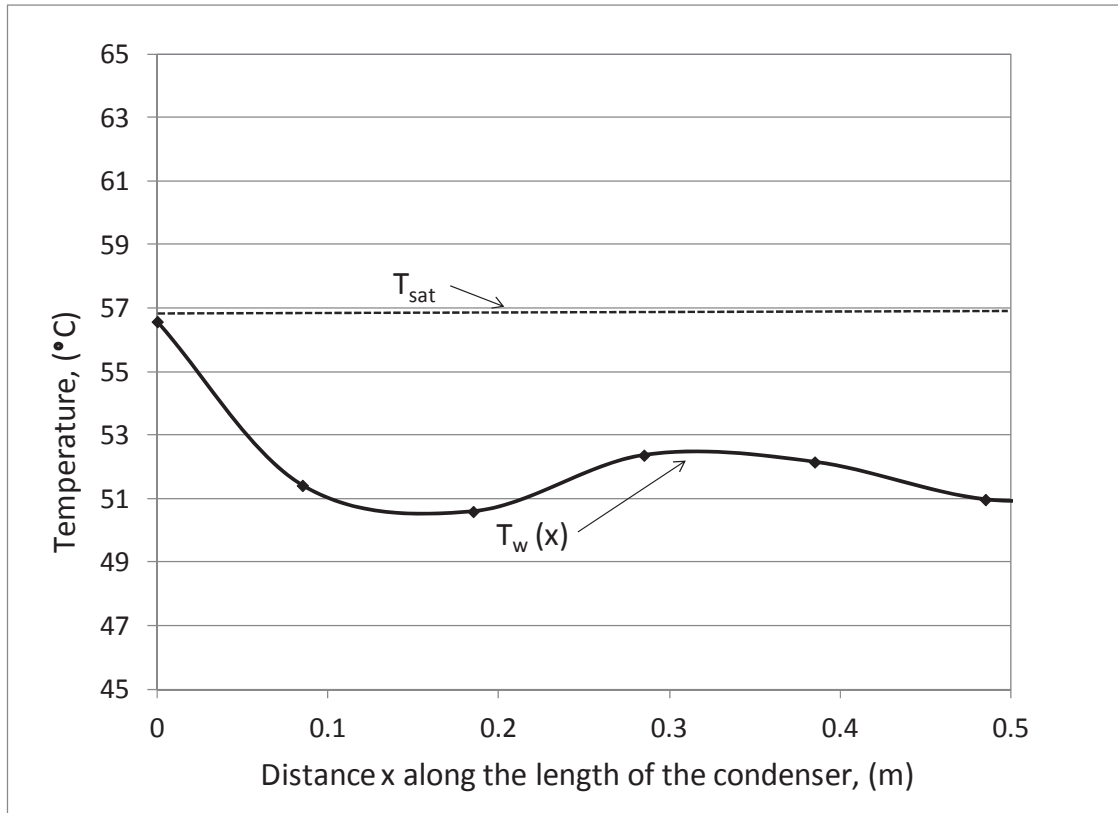


Figure 4.14: Condensing-surface temperature T_w versus distance x for case # 4 in Table 4.5.

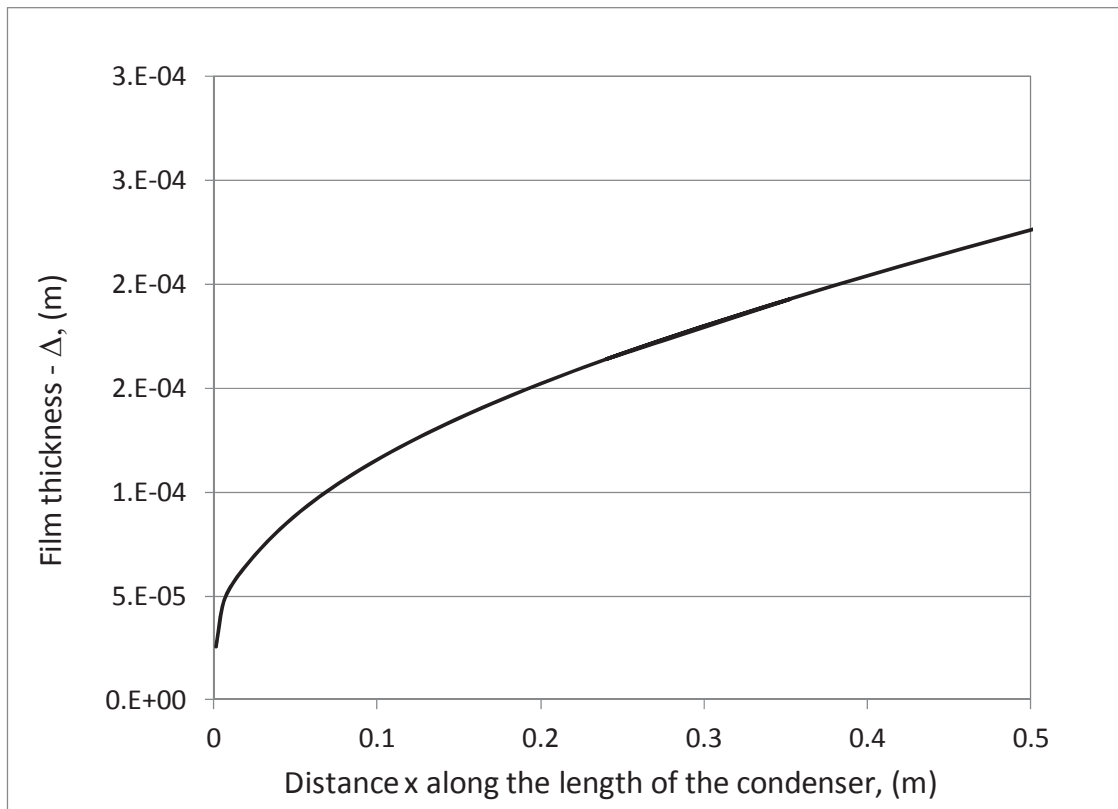


Figure 4.15: Liquid film thickness $\Delta(x)$ versus x for case # 4 in Table 4.5.

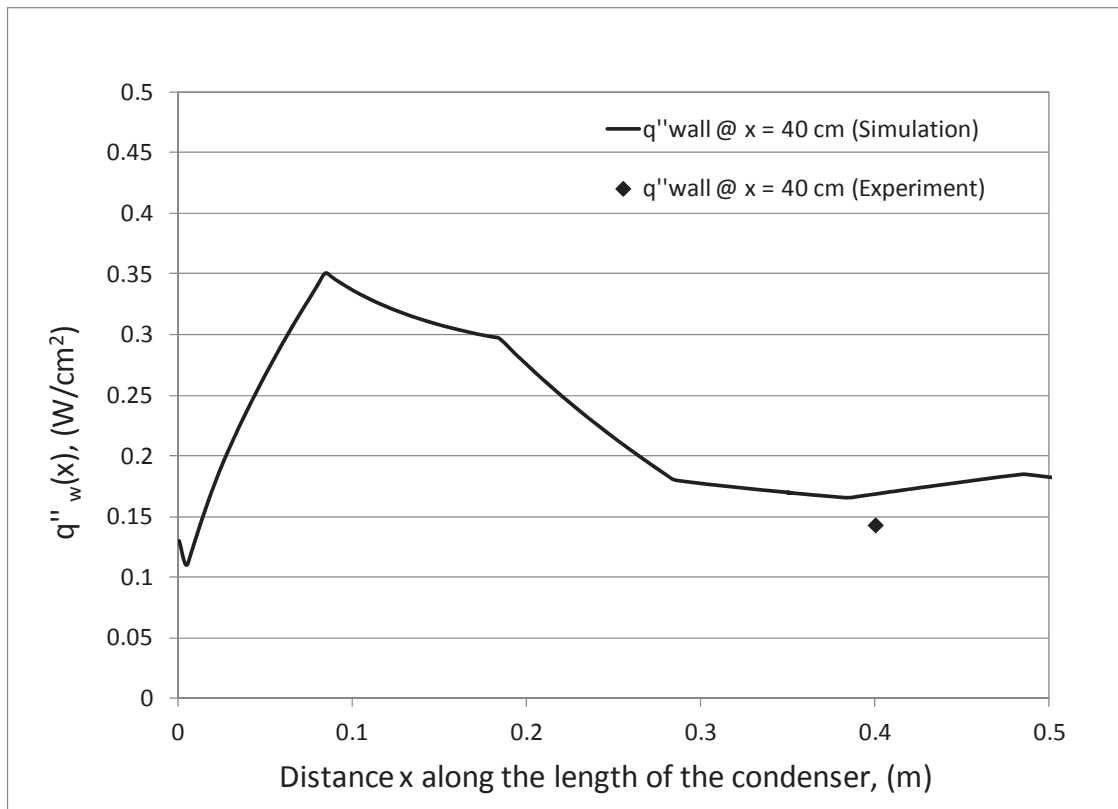


Figure 4.16: Condensing-surface heat-flux q''_w variations with x for case # 4 in Table 4.5.

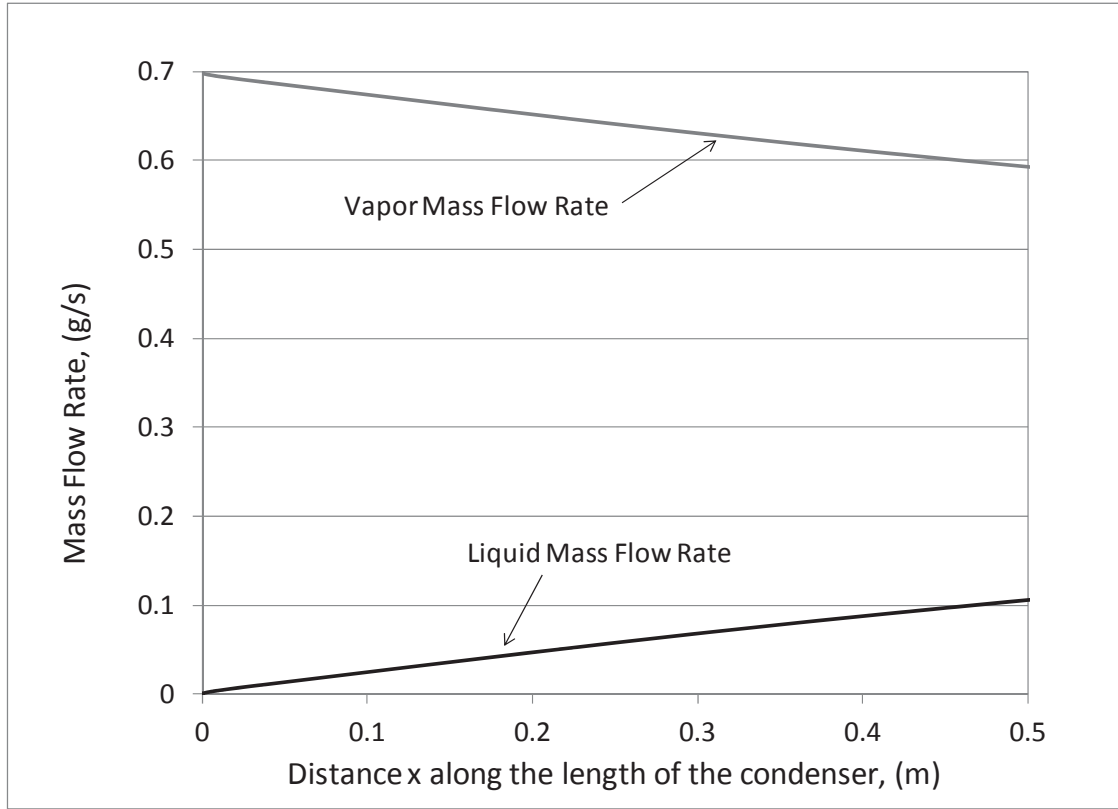


Figure 4.17: Cross-sectional liquid mass flow rate \dot{M}_L and the vapor mass flow rate \dot{M}_V for case # 4 in Table 4.5.

The 2-D steady tool is more accurate than the 1-D tool and it has the capability to simulate condensing flows in the presence of transverse gravity and compares results with 0g situations. Hence, this tool is used for this comparison. However, the 1-D tool is much quicker and more effective to implement.

The research that employs 2-D unsteady simulation theory to predict the length of the annular regime x_A and compares the predictions against selected experiments is currently ongoing. This work is also being extended to define the boundaries of the annular regime in a flow regime map (defined in terms of the governing non-dimensional parameters).

Table 4.5
Representative experimental runs for annular condensation

Case	\bar{M}_{in}	\bar{p}_{in}	$T_{sat}(\bar{p}_{in})$	\bar{T}_w	ΔT	$\bar{q}''_{w Expt}$ @ $x = 40$	$\bar{q}''_{w 2-D}$ @ $x = 40$	% Error for 2-D	x_A (Expt)
	g/s	kPa	° C	° C	° C	W/cm ²	W/cm ²		m
Error	± 0.05	± 0.15	± 1	± 1	± 1	$\pm 25\%$			$\pm 12\%$
1	0.702	99.98	56.6	48.6	7.9	0.18	0.23	27.3	71
2	0.700	99.99	56.6	49.8	6.8	0.16	0.22	36.9	90
3	0.700	99.99	56.6	50.0	6.6	0.15	0.21	38.6	93
4	0.698	99.99	56.6	50.7	5.9	0.14	0.17	25.0	95
5	1.000	101.07	57.0	44.0	13.0	0.40	0.48	19.6	57
6	1.470	101.07	57.0	46.6	10.4	0.59	0.49	16.8	70
7	1.599	101.07	57.0	47.2	9.8	0.60	0.50	16.4	88

However, the reader should be cautioned that typical horizontal tube experimental results available in the literature for mm or larger scale horizontal *tubes* are not in any of the categories of purely shear driven annular flows, or gravity dominated annular flows. This is because these flows are often three-dimensional in nature (except when vapor flows are fast and the flow is annular) where both forward shear and azimuthal gravity component are important.

4.3 Differences between Gravity Driven and Shear Driven Condensing Flows

Figure 4.18 shows the film thickness and cross sectional velocity and temperature profiles for gravity driven ($g_x = 9.8\text{m/s}^2$) and shear driven ($g_x = 0$) condensing flows in a tube under identical flow conditions. It can be seen from Fig. 4.18 that if all else remains the same, entirely shear driven annular flows have much thicker condensate ($\delta(x) \equiv \delta_{ps}(x)$, where subscript “ps” denotes pure shear) and, hence, much lower heat transfer rates (which is typically inversely proportional to film thickness). The comparative computational results shown in Figs. 4.18–4.19 for in-tube condensing flows of FC-72 vapor indicate remarkable differences between gravity and shear driven flows with regard to the velocity profiles (see Fig. 4.18) and pressure variations (see Fig. 4.19).

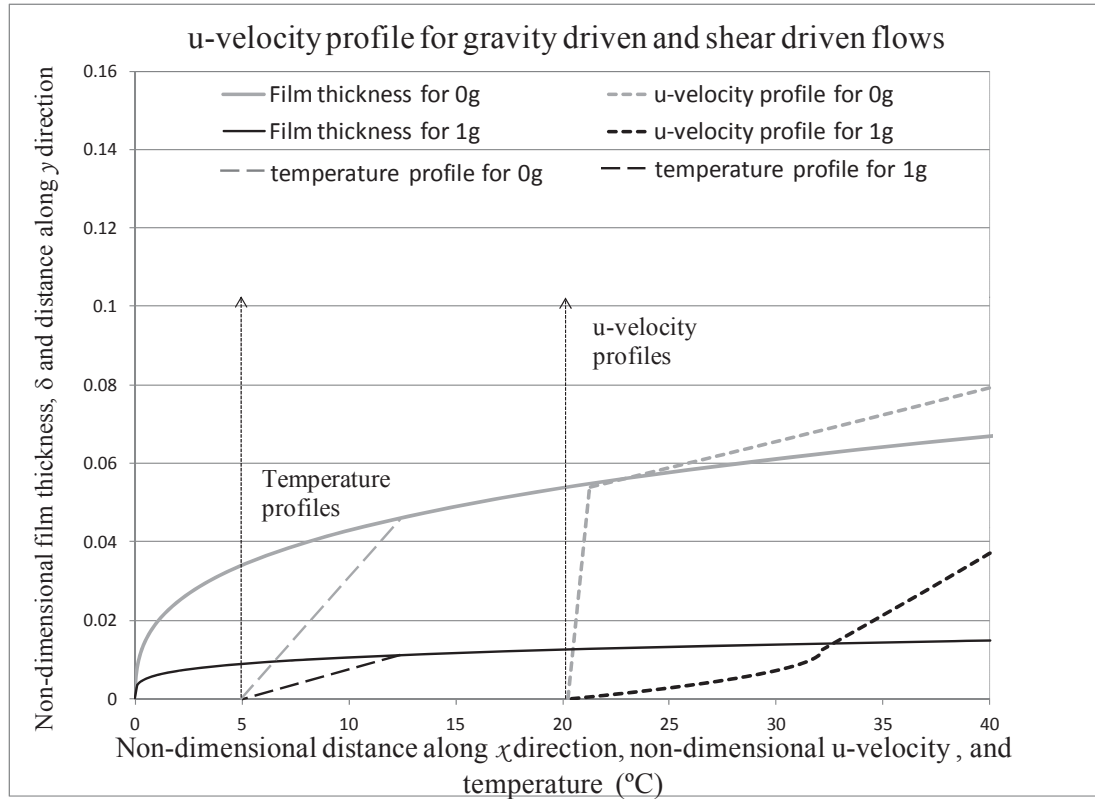


Figure 4.18: Figure shows film thickness versus x variation and the y -variations of the x -component of the velocity profile (at $x = 20$) for gravity driven 1g and shear driven 0g flows inside a tube. The figure also shows the linearity of temperature profiles (at $x = 20$) for both the cases. The solutions are obtained for flow of FC-72 vapor with inlet speed of $U = 0.7$ m/s, $\Delta T = 7.5^{\circ}\text{C}$, and diameter $D = 6.6$ mm.

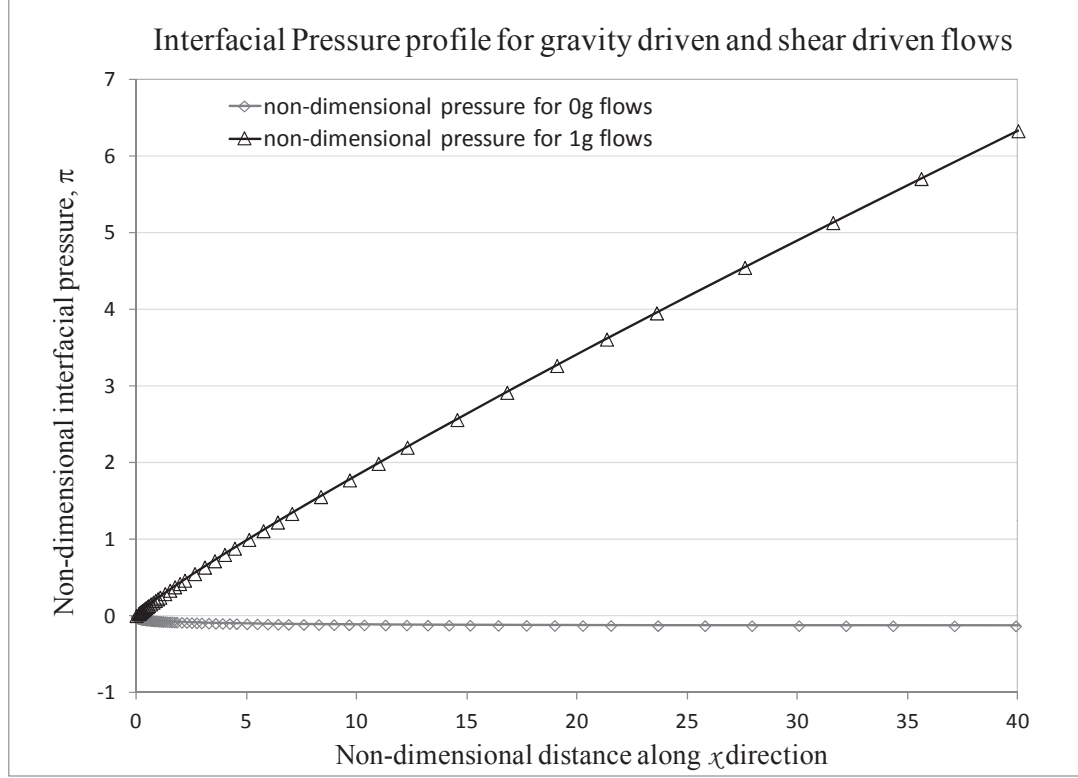


Figure 4.19: For the cases shown in Fig. 4.18, this figure shows the non-dimensional interfacial pressure variations with downstream distance.

The velocity profile for gravity driven flow is parabolic in shape with nearly zero slope at the interface (as interfacial shear is not needed to drive the condensate) while the one for shear driven flow is linear with adequate non-zero interfacial shear. For a cooling method that results in only moderate imposition of wall heat-flux, the pressure difference for gravity driven flow often amounts to a pressure rise (see Fig. 4.19) as opposed to small pressure drops associated with shear driven 0g flows. It should be noted that the actual pressure difference in the vapor phase needs to account for two competing effects: (i) a pressure rise needed for vapor deceleration associated with the size of mass transfer rate across the interface, and (ii) a pressure drop needed to overcome interfacial shear. For the gravity driven flow case in Fig. 4.19, it is the vapor deceleration effect that

dominates as interfacial shear is allowed to be negligible and for the shear driven case in Fig. 4.19, it is the interfacial shear effect that slightly exceeds the vapor deceleration effects (as interfacial mass transfer or wall heat-flux is not too high). For both gravity and shear driven flow cases, however, over the lengths considered, temperature profiles within the condensate film remain linear (see Fig. 4.18). This has been verified to be true even in a full 2-D steady simulation approach. It should be noted that the pressure difference features should not be generalized to all shear/pressure driven cases, as heat-flux controlled flows and flows in smaller diameters have different features.

For the gravity dominated condensate flows, the gravitational force and wall shear effects are so large relative to interfacial shear effects that gravity fully determines the condensate flow and the interface location. This interface location and associated interfacial mass-flux values then determine the rest of the vapor flow features (such as pressure variations, etc.) in a way that the pre-determined interface location and the condensate motion associated with the interface location remains independent of the inlet vapor mass flow rate.

However, the above comparisons of strictly steady flows are not enough to fully understand the differences between shear driven and gravity driven flows. The gravity dominated and shear/pressure driven flows show significant differences in response to inlet fluctuations in pressure/mass flow rates. One should refer Kivisalu et al. 2011 where experimental results show that, compared to gravity driven flows, shear driven unsteady flows show significantly greater sensitivity to imposition of time varying pressure-differences.

4.4 The 1-D approach's ability to handle different condensing-surface thermal boundary conditions for different methods of cooling

For many conjugate heat transfer problems, the thermal boundary condition for the condensing surface temperature $T_w(x)$ or heat-flux $q_w''(x)$ are not known and needs to be initially assumed. Subsequently these assumed values need to be iteratively corrected (until convergence) by checking their compatibility with the solution (or realization) of the adjoining conjugate heat transfer problem (s). As an example, after assuming a thermal temperature boundary condition $T_w(x)$ for the condensing-surface, the condensing surface problem is solved and heat-flux variation $q_w''(x)$ is found. This $q_w''(x)$ then becomes the boundary condition for the conjugate heat-transfer problem which is then solved and the solution of this conjugate problem yields a new value of $T_w(x)$ for the condenser-surface. With this new condensing-surface temperature boundary condition $T_w(x)$, the condensing flow problem needs to be solved again. The process of solving the condensation flow problem and the conjugate problem needs to be iterated until mutually consistent and convergent thermal boundary conditions for the condensing-surface is obtained. For the above reason, it is important to develop a solution technique that demonstrates the ability to solve a condensing flow problem for *any* known uniform or non-uniform thermal boundary condition of $T_w(x)$ or $q_w''(x)$.

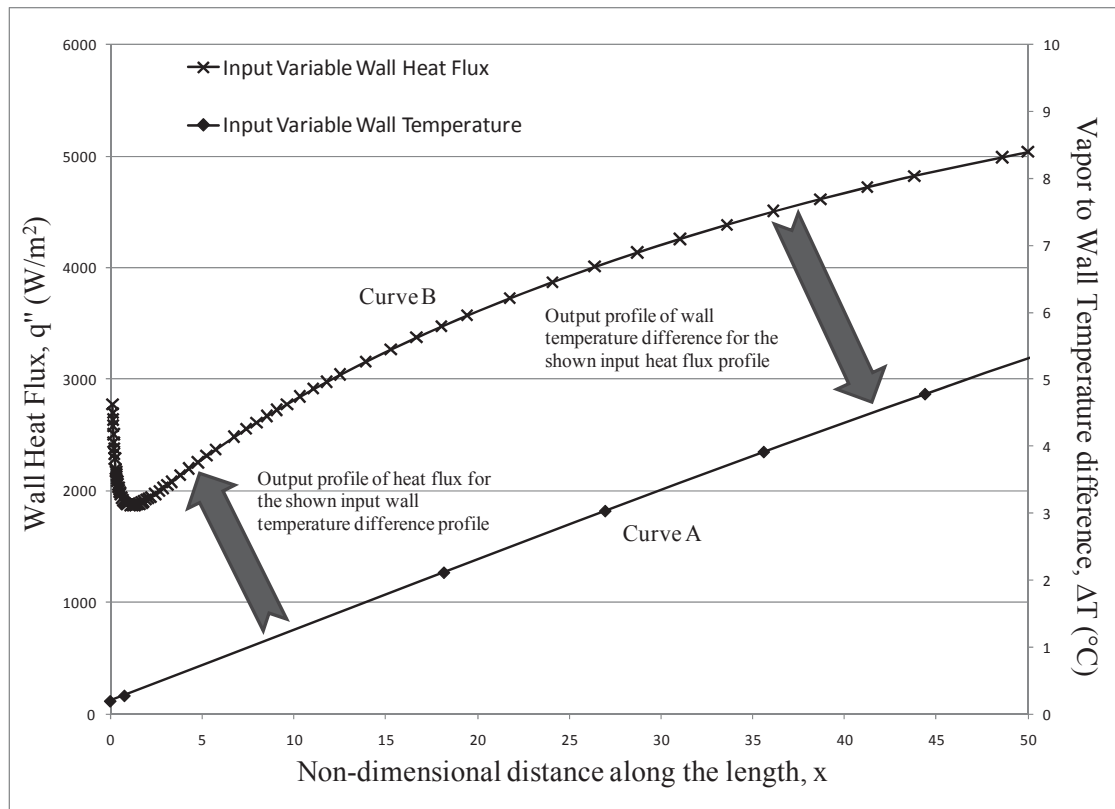


Figure 4.20: For a flow of FC-72 vapor inside a vertical tube condenser with average inlet speed $U = 7$ m/s, diameter $D = 0.002$ m, the figure shows the profiles of (i) vapor to condensing-surface temperature variations (curve A), and (ii) condensing-surface heat-flux variations (curve B).

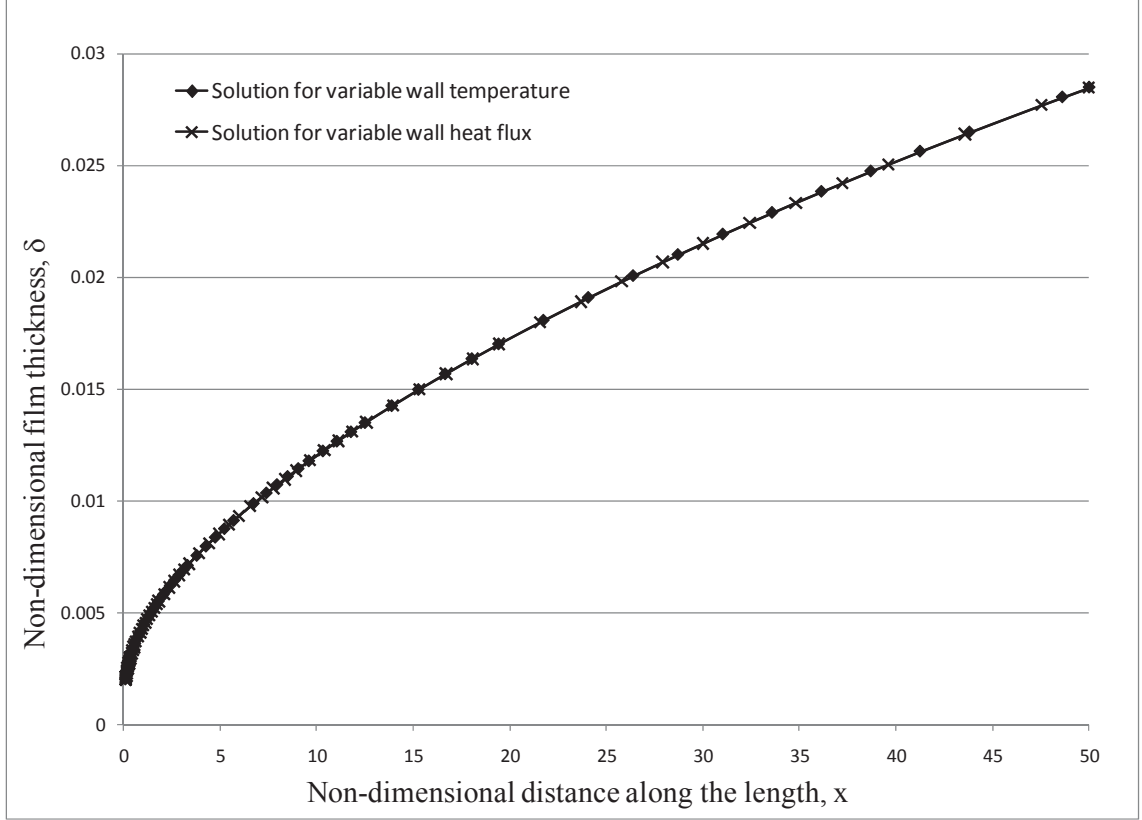


Figure 4.21: For the cases shown in Fig. 4.20, the non-dimensional film thickness profile predictions resulting from the solutions of the problems for variable wall temperature difference (curve A) and variable heat flux profile (curve B) as prescriptions for condensing-surface thermal boundary condition.

In Fig. 4.20, curve-A depicts an assumed $\Delta T(x) \equiv T_{\text{sat}}(p_{\text{in}}) - T_w(x)$ for a certain non-uniform condensing surface temperature $T_w(x)$. The 1-D simulation methodology described in chapter 3 for variable wall temperature yields the film-thickness $\delta(x)$ curve in Fig. 4.21 as well as the values of $q_w''(x)$ (in W/m^2) shown as curve-B in Fig. 4.20. The fact that this prediction methodology for a known $\Delta T(x)$ as well as the prediction methodology described in chapter 3 for variable wall heat-flux $q_w''(x)$ are both good is demonstrated next. We use the output of $q_w''(x)$ from the variable wall temperature case (curve-B in Fig. 4.20) as the input “known” wall heat-flux for the variable heat-flux methodology of chapter 3. This yields two results: (i) the film thickness $\delta(x)$ curve shown

in Fig. 4.21, and (ii) $\Delta T(x) \equiv T_{\text{sat}}(p_{\text{in}}) - T_w(x)$ values shown as curve-A in Fig. 4.20. The fact that both the $\delta(x)$ curves in Fig. 4.21 and the $\Delta T(x)$ curves in Fig. 4.20 are identical, establishes the efficacy of our 1-D simulation approach for the important class of problems involving non-uniform thermal boundary conditions for condensing-surface. To our knowledge, this type of simulation capability for a lower dimension 1-D technique has not been reported before and, therefore, is one of the unique contributions of this work.

4.5 Similarity and differences in shear driven flows (0g and transverse gravity) and gravity driven flows, with an assessment of their impact on the investigation of length of annularity

4.5.1 Similarity and differences between 0g and transverse gravity

For the internal condensing flows in a channel with $g_x = 0$, the flow is characterized as shear/pressure driven flow. Firstly, annular stratified steady solutions were computationally obtained for zero gravity ($g_y = 0 \text{ m/s}^2$) and transverse gravity ($g_y = -9.81 \text{ m/s}^2$) for the schematic channel geometry shown in Fig. 2.1. These steady solutions with $g_y = 0 \text{ m/s}^2$ and $g_y = -9.81 \text{ m/s}^2$ were found to be the same (except for the hydrostatic pressure) for the length of channel investigated. Figure 4.22 shows the agreement in the representative film thickness for a flow of FC-72 in a channel with $g_y = 0 \text{ m/s}^2$ and $g_y = -9.81 \text{ m/s}^2$ and identical flow conditions. Similar agreement exists in all the flow variables except for the cross-sectional pressure profile. A representative cross-sectional pressure profile at $x = 0.15$ is shown in Fig. 4.23. The pressure rise towards the condensing surface

for the transverse gravity ($g_y = -9.81 \text{ m/s}^2$) case is due to the hydrostatic pressure component.

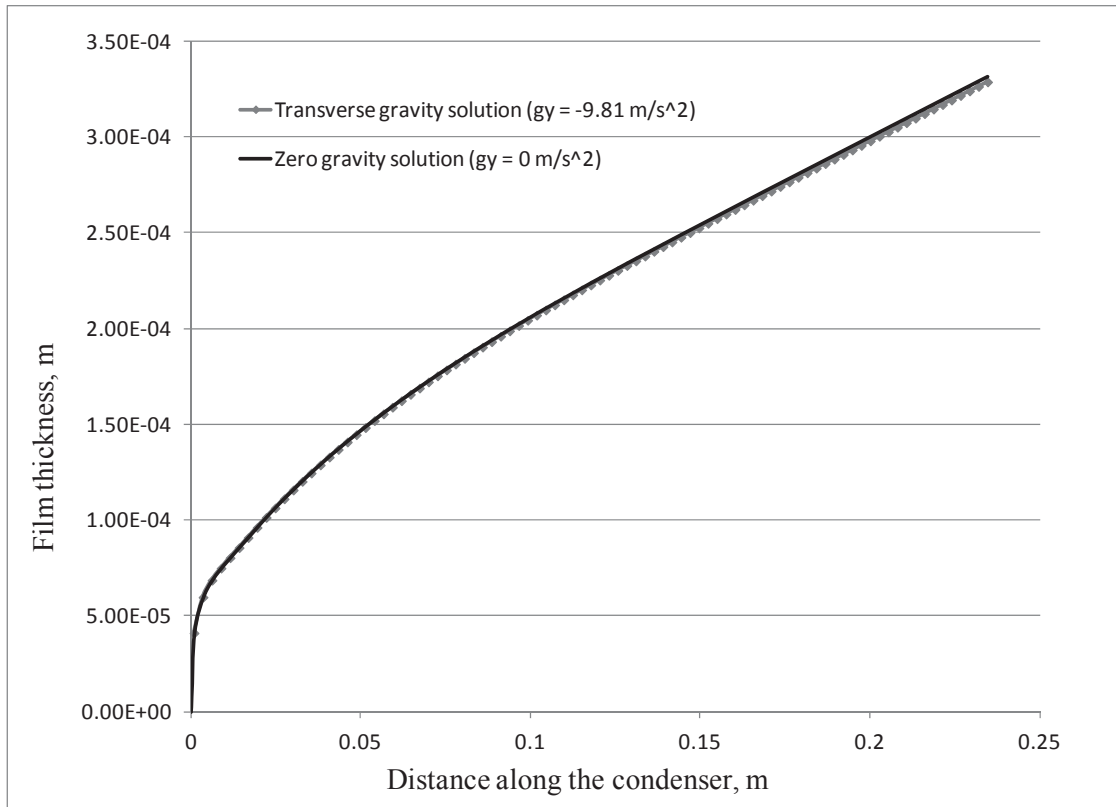


Figure: 4.22: Film thickness comparisons for shear driven flows in the presence ($g_y = -9.81 \text{ m/s}^2$) and the absence ($g_y = 0 \text{ m/s}^2$) of transverse gravity.

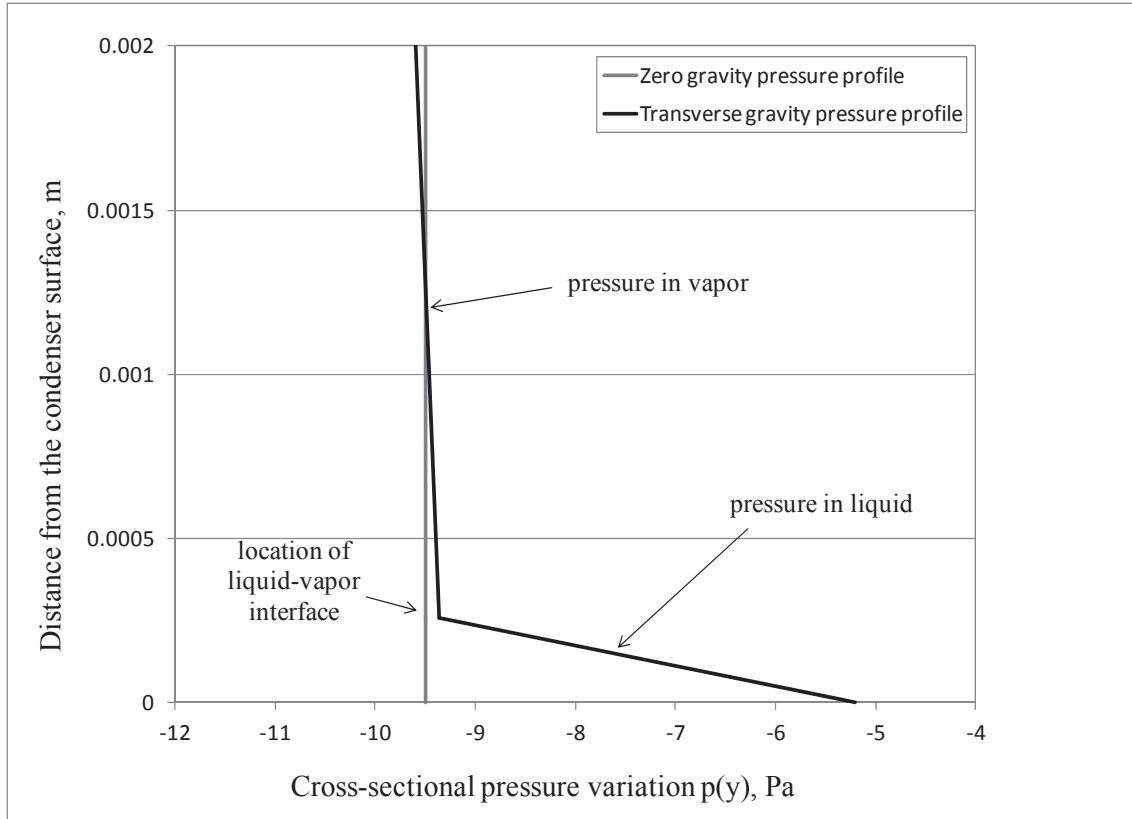


Figure 4.23: The figure shows the pressure variation at $x = 0.15$ m for a flow as in Fig. 4.22, in the presence ($g_y = -9.81$ m/s²) and the absence ($g_y = 0$ m/s²) of transverse gravity.

4.5.2 Investigation for estimating the length of annular regime

For condensing flow inside a horizontal channel, both annular/stratified and non-annular plug/slug, bubbly, etc regimes are observed. Amongst these regimes particular interest is in attaining and maintaining the annular flow regime. This is because it has high thermal efficiency. Therefore, specially for shear/pressure driven flows, it is important to investigate the length of annularity for a given mass flow rate at the inlet, and thermal boundary condition. In Gorgitrattanagul 2011, the length of annularity has been investigated for a horizontal condenser for range of mass flow rates and average temperature difference between the condensing surface and the saturation temperature.

The 2-D computational tool presented here has the capability to simulate condensing flows in long channels. Therefore, computational simulation results are obtained for a flow inside a 2 mm horizontal channel (with flow of pure FC-72) with 0.4 g/s vapor mass flow rate at the inlet and average $\Delta T = 17.45^\circ\text{C}$. This case simulates the condensing flow inside the channel described in Fig. 4.13, and represents operating conditions that are the same as in run S3C4 in Gorgitrattanagul 2011. Figures 4.24 - 4.25 show sample results obtained from the full steady 2-D computational tool that solve this horizontal channel problem in the presence of transverse gravity ($g_y = -9.81 \text{ m/s}^2$).

Figure 4.24 shows film thickness and liquid interfacial velocity along the length of the condenser for this case. As seen here, the film thickness is seen to grow as interfacial velocity (and interfacial shear as seen in Fig. 4.25) decreases with distance along the condenser. In the initial portion of the condenser, as the film thickness is very small, the vapor rapidly condenses; the interfacial velocity (see Fig. 4.24) increases driving the condensate motion forward. For this small zone the interfacial pressure force per unit volume term $(-dp/dx)^i$ in the momentum balance, shown in Fig. 4.26, is negative indicating flow deceleration near the interface. This is because of the bending of the streamlines in the vapor as it rapidly condenses. The streamline plot of velocity magnitude is shown in Fig. 4.27. Downstream of this zone, for $0 < x < x'$ in Figs. 4.24-4.26, as the film thickness increases, the interfacial shear continues to drop and pressure force per unit volume continues to increase to assist in driving the condensate forward.

As seen in Fig. 4.24, the interfacial condensate velocity is seen to increase up to a point x' , and then it starts decreasing for the zone $x > x'$. In this zone $x > x'$, the pressure force per unit volume starts decreasing - indicating concurrent reduction in the pressure

force as well as viscous force. Note that, the interfacial shear in Fig. 4.26 continues to approach zero. As shown in Fig. 4.27, the streamlines in the liquid bend upwards after it crosses the liquid-vapor interface and this indicates an upward moving difficult trajectory in comparison to gravity driven flows. This trajectory is due to a lack of forward moving force that arises from insufficient interfacial shear (see Fig. 4.26) as well as an eventually decreasing pressure gradient (see Fig. 4.26). Hence, the resulting film thickness in this zone increases rapidly. For the case simulated here, the length of the annular zone is experimentally found to be 0.27 m in Gorgitrattanagul 2011. This rapid rise in film thickness and insufficient shear suggests that any noise/disturbance given at this location would eventually grow and break the film into non-annular morphology. This hypothesis will be tested by R. Naik through the unsteady numerical simulations and will be presented in Naik, 2012.

Also, as shown in Kivisalu et al. 2011, shear driven flows are very sensitive to inlet pressure/mass flow rate fluctuations. It is shown in Kivisalu et al. 2011 that significant heat transfer enhancements and change in the length of annular zone is observed for frequently occurring minuscule absolute pressure fluctuations at the inlet of the horizontal condenser. Hence, it is essential to computational study the impact of small to moderate inlet pressure fluctuations (about, 1kPa amplitudes for a mean pressure of around 100 kPa – with frequency in the range of 0-20 Hz) on shear/pressure driven condensing flows.

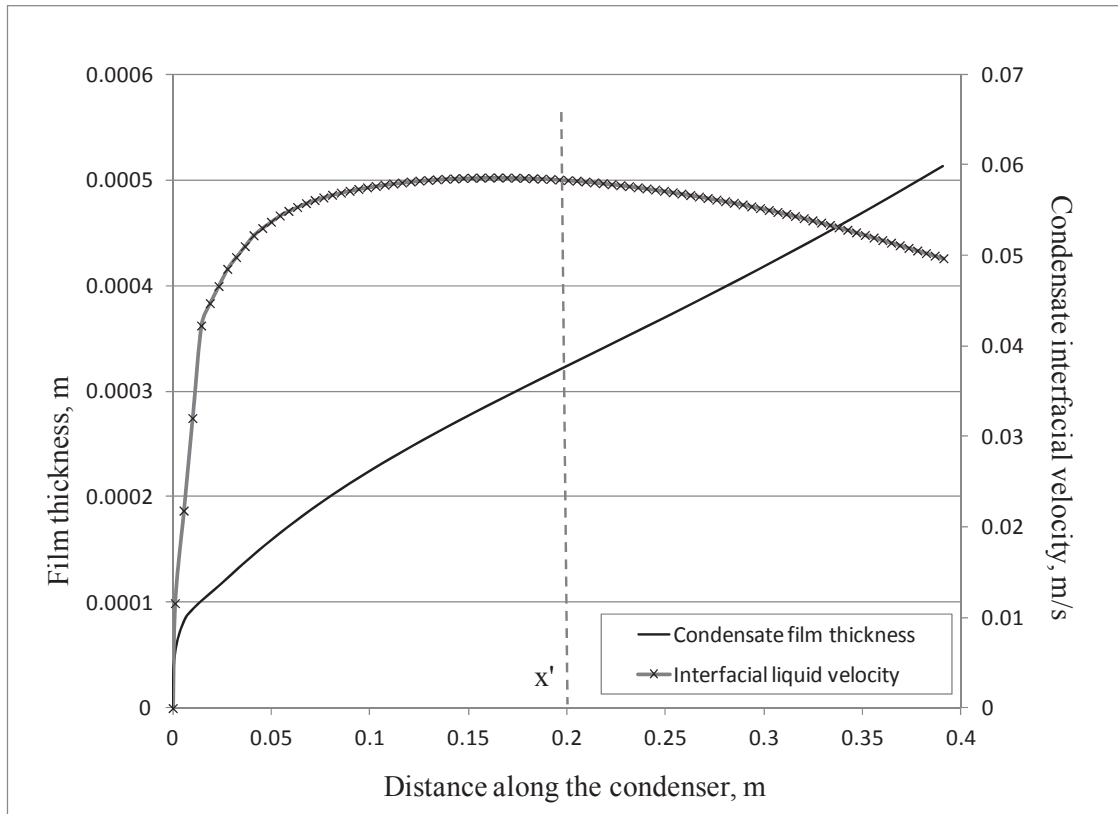


Figure 4.24: For the flow of FC72 vapor in a horizontal channel with channel height = 2 mm, the figure shows the film thickness and condensate interfacial velocity along the length of the condenser. The case is simulated for inlet mass flow rate = 0.4 g/s and $\Delta T = 17.45$ °C.

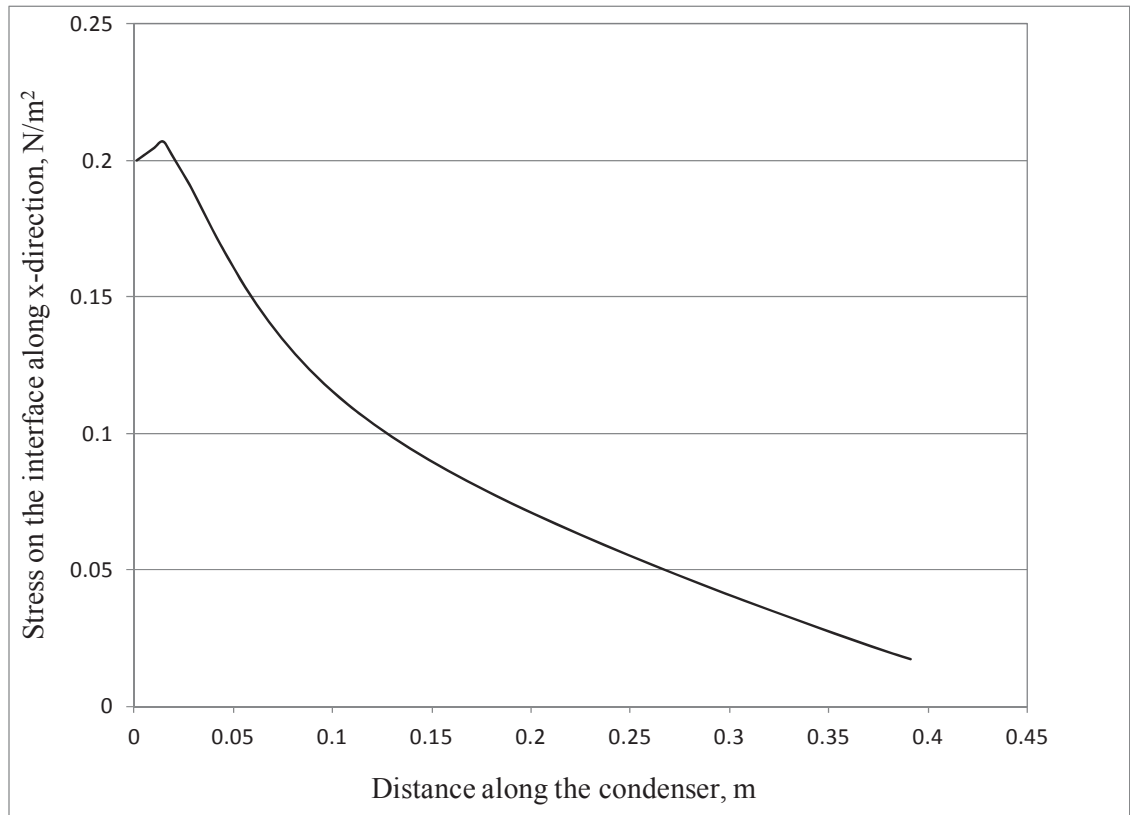


Figure 4.25: For the flow in Fig. 4.24, the figure shows interfacial stress on the interface along the length of the condenser.

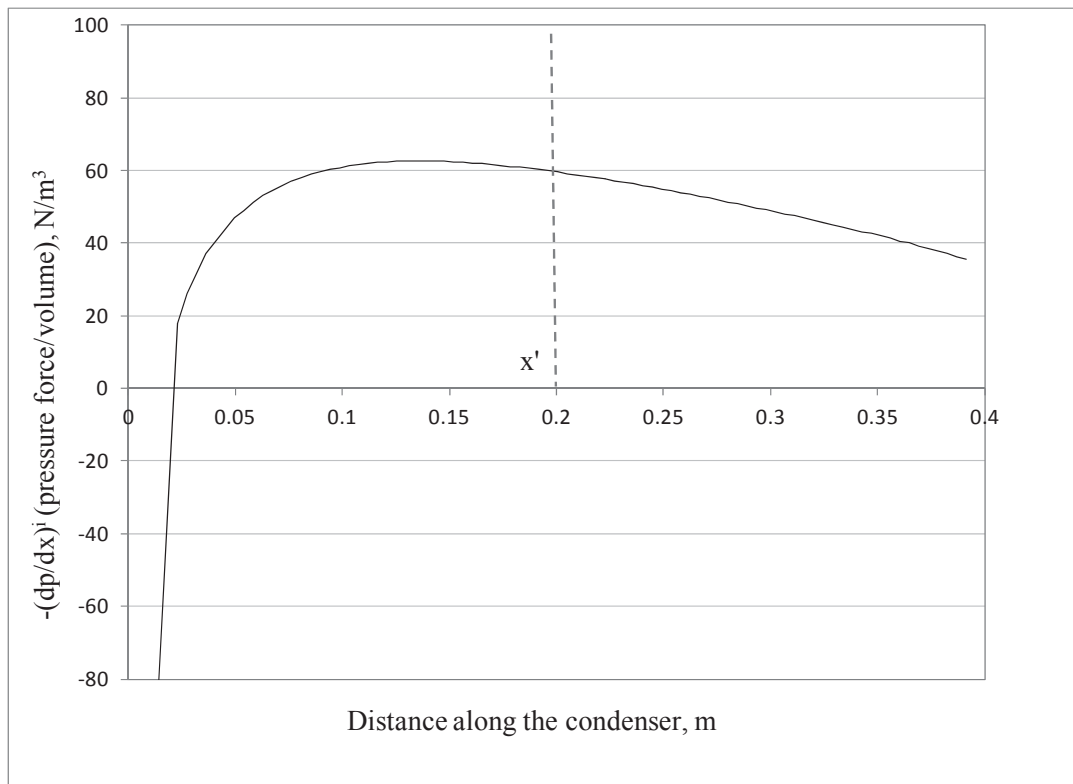


Figure 4.26: The figure shows pressure gradient along the length of the condenser.

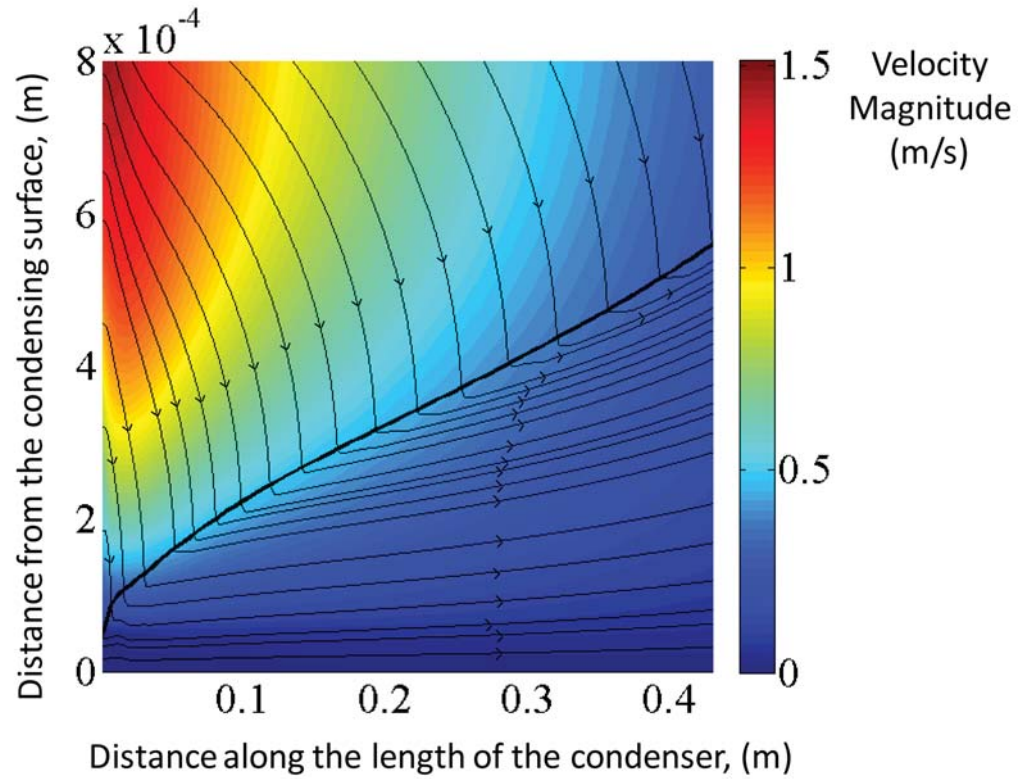


Figure 4.27: Streamline plot of velocity magnitude for the flow in Fig. 4.24.

4.5.3 Impact of inclination on condensing flow in tilted channels

A comparison of shear driven condensing flow ($g_x = 0 \text{ m/s}^2$) inside a channel with $g_y = 0 \text{ m/s}^2$ and $g_y = -9.81 \text{ m/s}^2$ has been shown in section 4.5.1. Most of the flow variables (except for cross-sectional pressure) were shown to be the same, over the distance considered, for the two cases.

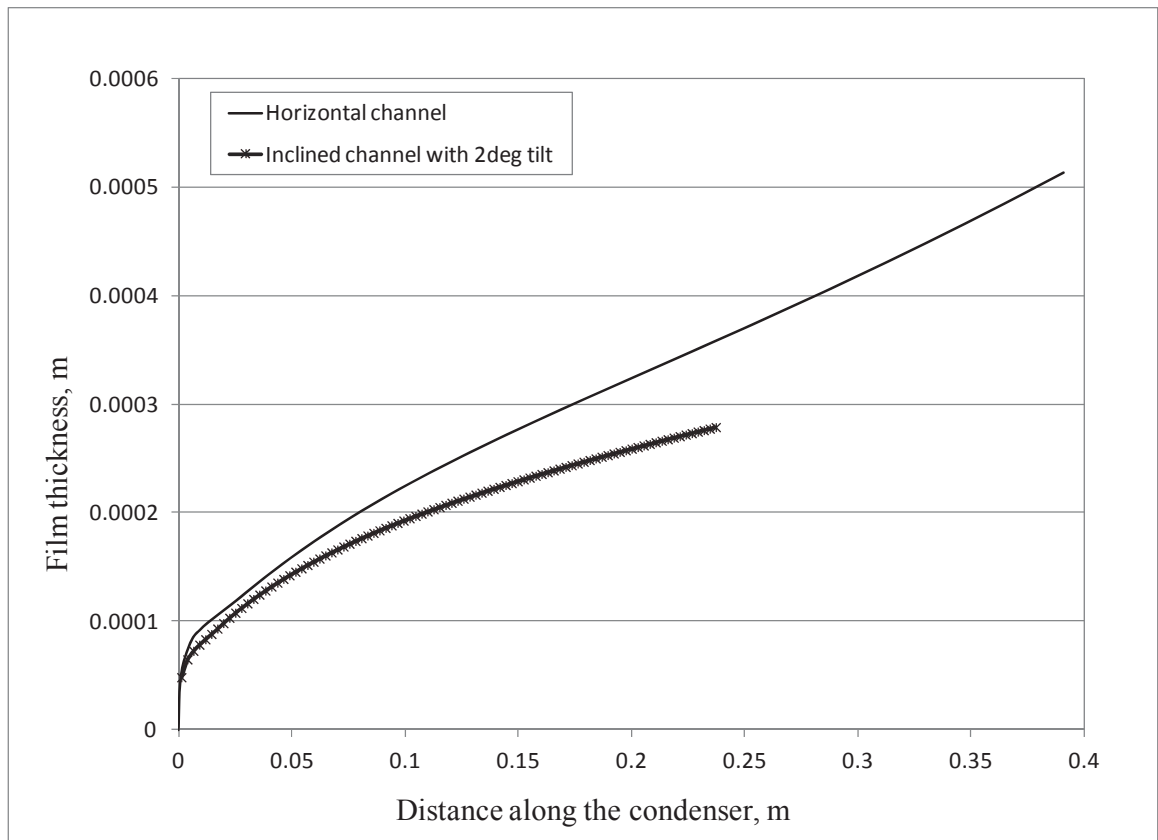


Figure 4.28: Figure shows comparisons of film thickness for a horizontal channel flow and a channel with 2° inclination. The flow condition is same as that of Fig. 4.24.

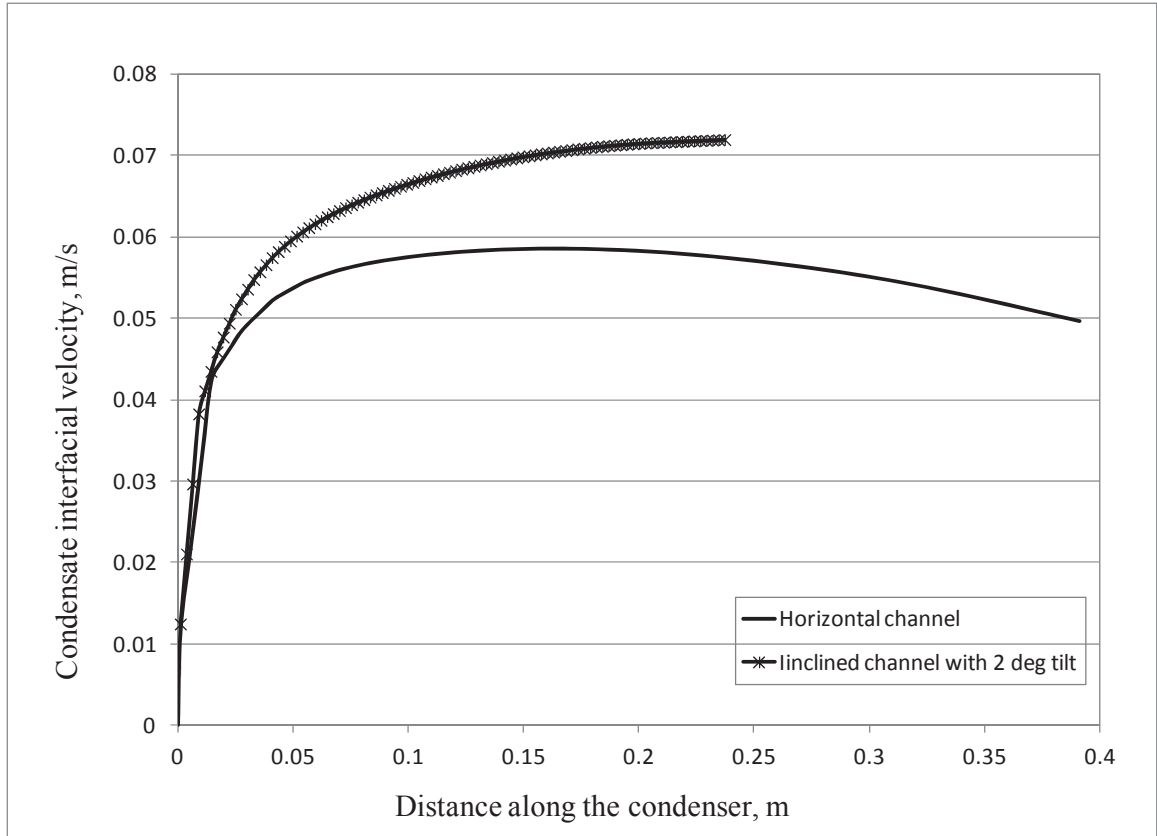


Figure 4.29: Figure shows comparisons of condensate interfacial velocity for a horizontal channel flow and a channel with 2° inclination. The flow condition is same as that of Fig. 4.24.

For a long horizontal channel with $g_y = -9.81 \text{ m/s}^2$, the flow physics shown in Figs. 4.24-4.27 suggests that for $x > x'$, the flow due to insufficient shear will not remain annular. For the same channel the impact of small inclination on the flow has been studied here. Figure 4.28 compares the film thickness for a horizontal channel and a channel with 2° inclination. The film thickness for the channel with 2° inclination is significantly different than the horizontal channel solution. For the channel with 2° inclination, approximately 90 % of the incoming vapor had condensed by the downstream distance of 0.25 m. Hence the depicted solution is shorter in length compared to the horizontal channel solution. Figure 4.29 shows that, for the channel with

2° inclination, the condensate interfacial velocity continues to increase along the length. This is due to the impact of gravity on the flow as gravity assists in draining the condensate in the condenser. Thus, even small inclinations affect the flow from being purely shear driven to flow with substantial influence from gravity. Figure 4.30 shows the streamlines and velocity magnitude for the channel with 2° inclination. Note that the liquid streamlines in the gravity assisted flows in Fig. 4.30 do not need to end upwards as do the streamlines in the shear/pressure driven flow case of Fig. 4.27. These qualitative results on what causes loss of annularity for shear/pressure driven flows are being made quantitative by R. R. Naik, with the help of unsteady simulations and the method of characteristics.

As the tilt of the channel change, investigation that demarcate the flows' non-dimensional parameter space into purely shear driven zone, purely gravity dominated zone and “mixed” transition zone is presented in Chapter 5.

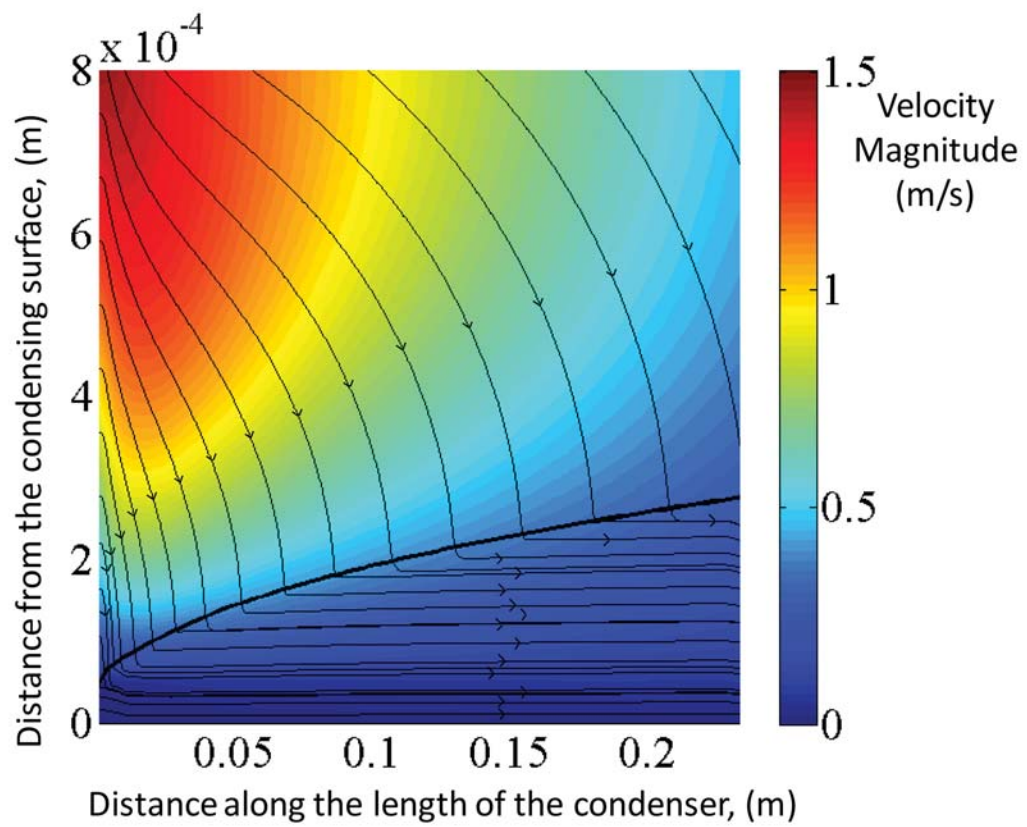


Figure 4.30: Streamline of velocity magnitude for a channel with 2° inclination.

5. Computational results that define the transition zone between entirely gravity driven and entirely shear/pressure driven annular/stratified condensing flows

The results, correlations, and transition maps presented in this chapter was previously published in Mitra 2011⁸. For the in-tube flow in Fig. 2.2, this solution technique allows an investigation of the role of the gravitational acceleration component g_x on the nature of the flows. To better comprehend the role of gravity on the condensing flow, the typical non-dimensional gravity given by Fr_x^{-1} is not conclusive. This is because the Fr_x^{-1} has the average inlet velocity. Therefore, we define a gravity parameter $G_p \equiv Fr_x^{-1} \cdot Re_{in}^2$, which is independent of average inlet velocity.

Using this gravity parameter, G_p , the non-dimensional solution space (x , Re_{in} , Ja/Pr_1 , $G_p = Fr_x^{-1} \cdot Re_{in}^2$, $Fr_y^{-1}=0$, ρ_2/ρ_1 , μ_2/μ_1) can be divided in a is purely shear driven domain (where $g_x = 0$) and gravity dominated domain (where g_x is sufficiently large and the flow is in the sense that the interface location and the condensate motion is entirely determined by gravity).

At a fixed location $x = x^\#$ of an in-tube flow, Fig. 5.1 shows the variation of film thickness ratio ($\delta(x^\#)/\delta_{ps}(x^\#)$) for a flow of FC-72 vapor, as a function of the gravity parameter G_p ($\equiv Fr_x^{-1} \cdot Re_{in}^2 \equiv (\rho_2^2 g_x D_h^3) / \mu_2^2$) when this parameter is increased by changing the gravitational component g_x from $g_x = 0$ to $g_x = 9.81 \text{ m/s}^2$. Here, $\delta_{ps}(x^\#)$ is the non-dimensional film thickness at $x = x^\#$ for the pure shear case where $G_p = 0$ (i.e. $g_x = 0$). The film thickness ratio $\delta(x^\#)/\delta_{ps}(x^\#)$ is equal to 1 for $G_p = 0$ (as $\delta(x) = \delta_{ps}(x)$, for $G_p =$

⁸ Some parts of the paper have been reproduced in this chapter by kind permission of Elsevier. The copyright permission is attached as separate document.

0), whereas, for $G_p > G_p^*$, the film thickness ratio quickly settles at a number equal to $\delta_{Nu}(x^\#)/\delta_{ps}(x^\#)$. Here, $\delta_{Nu}(x)$ is the non-dimensional film thickness for the gravity dominated case given by Eq. (10.21) of Incropera et al. 2002. For sufficiently large G_p , one is in the *gravity dominated* zone for most $x > 0$, and the solution behaves as if $\delta(x) \approx \delta_{Nu}(x)$, where $\delta_{Nu}(x)$ is the classical Nusselt result given by:

$$\delta_{Nu}(x) = \frac{1}{L_c} \left[\frac{4 \cdot k_1 \cdot \mu_1 \cdot \Delta T \cdot x}{g \cdot \rho_1 \cdot (\rho_1 - \rho_2) \cdot h_{fg}} \right]^{1/4}$$

$$\cong [4 \cdot (Ja/Pr_1) \cdot (x/G_p) \cdot (\mu_1/\mu_2)^2 \cdot (\rho_1/\rho_2)^2]^{1/4} \quad (5.1)$$

Figure 5.1 illustrates the significant transitions that take place as G_p increases and that purely shear driven flows seem to exist only for very small near zero G_p values. This discussion emphasizes the need to develop a transition map to demarcate the boundaries between a gravity dominated zone and a purely shear driven zone.

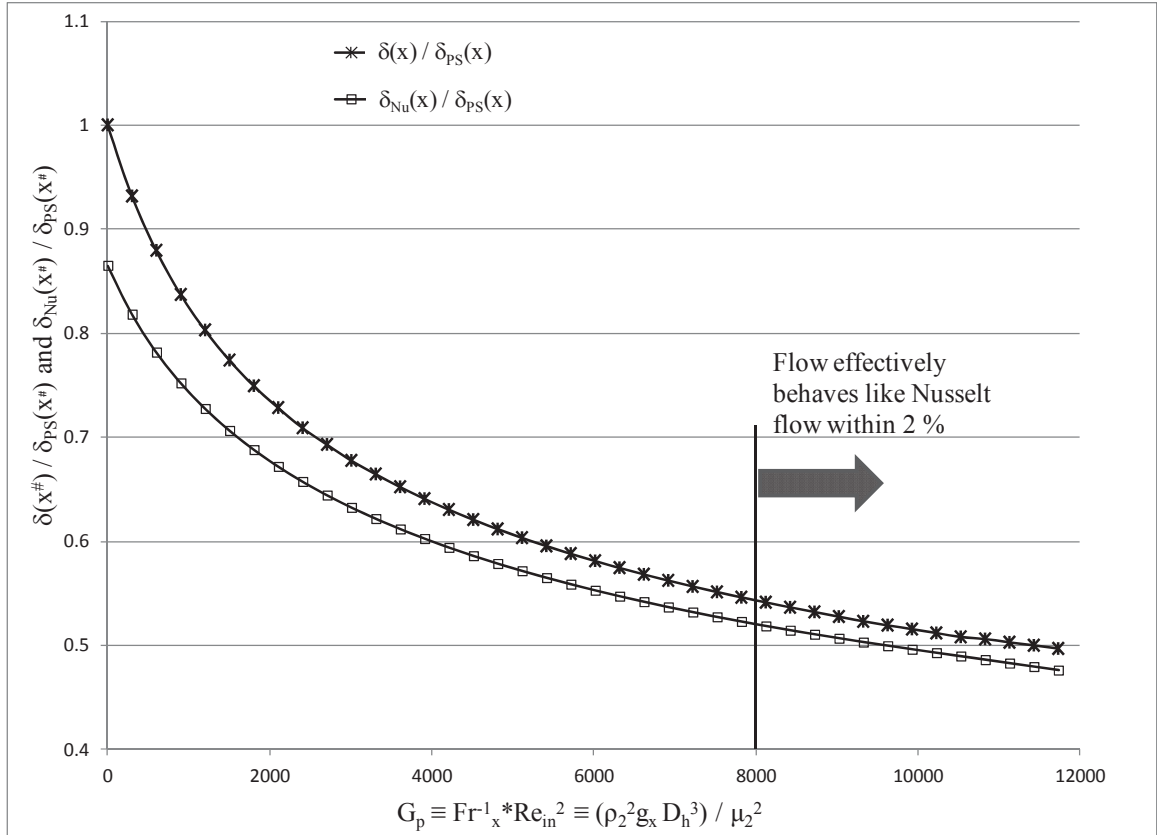


Figure 5.1: Figure shows the variation in film thickness ratio ($\delta(x^\#)/\delta_{ps}(x^\#)$) and ($\delta_{Nu}(x^\#)/\delta_{ps}(x^\#)$) at $x^\# = 80$ with variations in G_p . The solutions are obtained for flow of FC-72 vapor with inlet speed of $U = 0.7$ m/s, $\Delta T = 7.5^\circ\text{C}$, and diameter $D = 6.6$ mm.

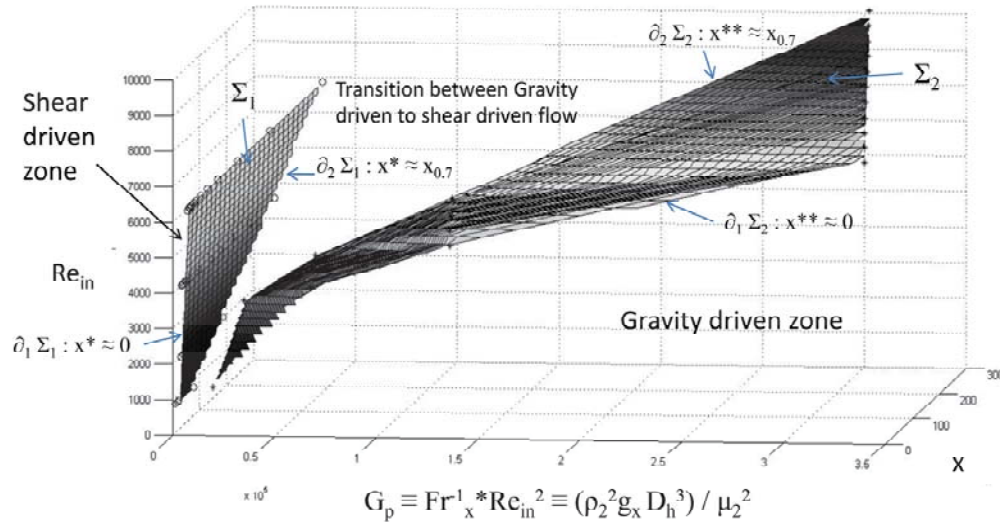


Figure 5.2: The figure yields a division of (x, Re_{in}, G_p) space that marks a gravity dominated zone, a shear dominated zone, and a transition zone between them. The flow of FC-72 vapor inside the tube has $Ja/Pr_1 = 0.004$, $(\rho_2/\rho_1) = 0.0148$ and $(\mu_2/\mu_1) = 0.0241$.

The gravity and shear driven condensing flows for the in-tube flows under varying values of g_x are governed by the following non-dimensional parameters:

$$\{x, Re_{in}, G_p, \frac{\rho_2}{\rho_1}, \frac{\mu_2}{\mu_1}, Ja/Pr_1\}, \quad (5.2)$$

where $Re_{in} \equiv \rho_2 U D / \mu_2$, $G_p \equiv Fr_x^{-1} * Re_{in}^2 \equiv \rho_2^2 g_x D_h^3 / \mu_2^2$, and $Ja/Pr_1 \equiv \Delta T k_l / h_{fg} \mu_1$.

Figure 5.2 shows a division of (x, Re_{in}, G_p) space, between gravity dominated and shear driven flows for a given set of values for $(Ja/Pr_1, \rho_2/\rho_1, \mu_2/\mu_1)$. To the left of the surface Σ_1 , the solutions are within 4% of pure shear ($g = 0$) solution $\delta_{ps}(x)$ and to the right of the surface Σ_2 , one is within 4% of the gravity dominated Nusselt result $\delta_{Nu}(x)$ given in Eq. (5.1).

Since all the flow variables (non-dimensional film thickness δ , non-dimensional pressure π , etc.) are functions of the variables listed in Eq. (5.2), for the purpose of limiting our discussions to some refrigerants (water, FC-72, R-113, etc.) and some commonly occurring situations ($U = 0.5$ m/s to 3 m/s, $D = 1$ mm to 7 mm, $\Delta T = 3$ °C to 25 °C, etc.), we limit the non-dimensional parameters in Eq. (5.2) to:

$$\begin{aligned}
0 \leq x \leq x_A < x_{FC} \quad \text{or} \quad 0 \leq x \leq x_{0.75} \approx x_A \\
900 \leq Re_{in} \leq 22000 \\
0.0036 \leq Ja/Pr_1 \leq 0.0212 \\
3.2E-4 \leq \rho_2/\rho_1 \leq 0.03 \\
0.0113 \leq \mu_2/\mu_1 \leq 0.06 \\
57000 \leq G_p \leq 4,840,000.
\end{aligned} \tag{5.3}$$

In the first inequality in Eq. (5.3), x_A is the approximate length up to which steady annular/stratified flows might actually exist in reality (i.e. the flow is stable and is allowed to self-seek its natural exit condition) and x_{FC} is the length of full condensation. For gravity dominated cases, it is found, both computationally and experimentally Kurita et al. 2011, that $x_{FC} \approx x_{1.0}$ is the location where approximately 100% of the incoming vapor flow rate is condensed and the flow is still mostly in the wavy annular regime. As a result, the reported 1-D annular flow results are meaningful up to x_{FC} or quite close to it. However, for pure shear driven cases where the flow is allowed to self-seek its natural exit condition, the assumption of annular/stratified flows beyond a certain distance x_A (where A is the number denoting the fraction of \dot{M}_{in} that has condensed up to that location) is generally not true (see Gorgitrattanagul 2011) as more complex flow

morphologies (such as plug/slug, bubbly, etc. flows) typically occur over a significant distance between x_A and x_{FC} .

It is computationally found that, for the parameter range in Eq. (5.3), one can solve the steady equations for both gravity and shear driven flows for $0 \leq x \leq x_{0.75}$ where, $x_{0.75}$ ($\equiv x_{0.75}(Re_{in}, Ja/Pr_1, G_p, \rho_2/\rho_1, \mu_2/\mu_1)$) is defined to be the distance at which 75% of the incoming vapor flow rate \dot{M}_m is condensed.

Furthermore, because condensate flows are thin, it is assumed that the flow conditions are such that the condensate is laminar up to x_{FC} for most cases of interest. This laminar flow assumption is subsequently verified through the well-known Incropera et al. 2002 thumb rule which states that, the film Reynolds number $Re_\delta \cong 4\dot{M}_L(x)/\pi D\mu_1$ (where $\dot{M}_L(x)$ is the cross-sectional condensate mass flow rate in kg/s) be approximately less than 1000. Though, strictly, laminar/laminar modeling of the flow should be adequate only for $Re_{in} \leq 2100$ in order to ensure vapor laminarity, it is experimentally found that (see Kurita et al. 2011) the assumption of “near interface” laminarity is all that is needed for heat transfer prediction by this model. This assumption is valid for much higher values of Re_{in} (see the sample criteria that is experimentally developed in Kurita et al. 2011 for the flow of FC-72).

Details, trends, and projections for the surfaces Σ_1 and Σ_2 in Fig. 5.2

The transition between gravity dominated region (right of Σ_2) and the purely shear driven region (left of Σ_1) as represented in Fig. 5.2 is now described. This description needs the help of the subsequent Figs. 5.3–5.4.

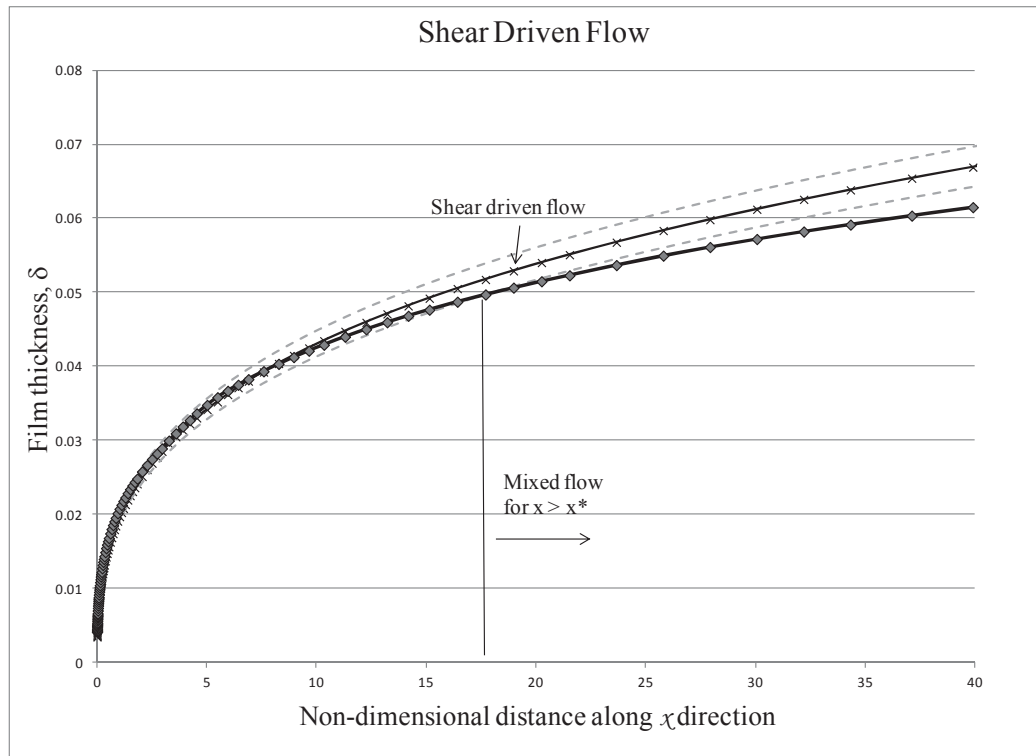


Figure 5.3: The figure shows the 4 % rule and a distance x^* by which the flows are categorized with respect to the pure shear (0g) film thickness profile $\delta_{ps}(x)$.

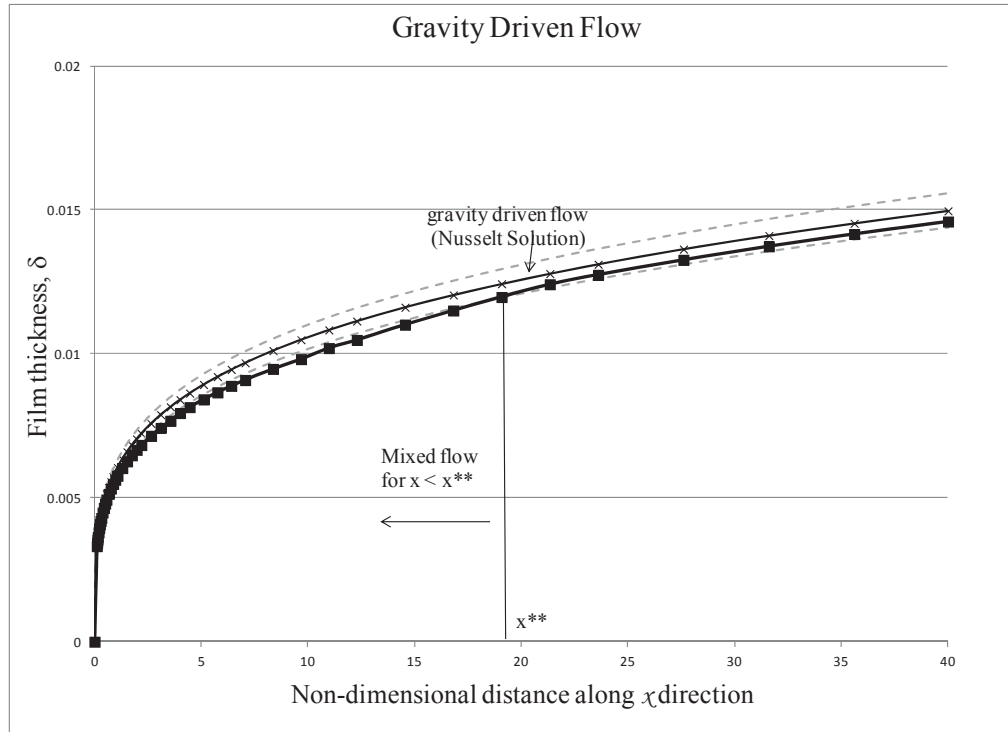


Figure 5.4: The figure shows the 4 % rule and a distance x^{**} by which the flows are categorized with respect to gravity dominated film thickness profile $\delta_{Nu}(x)$.

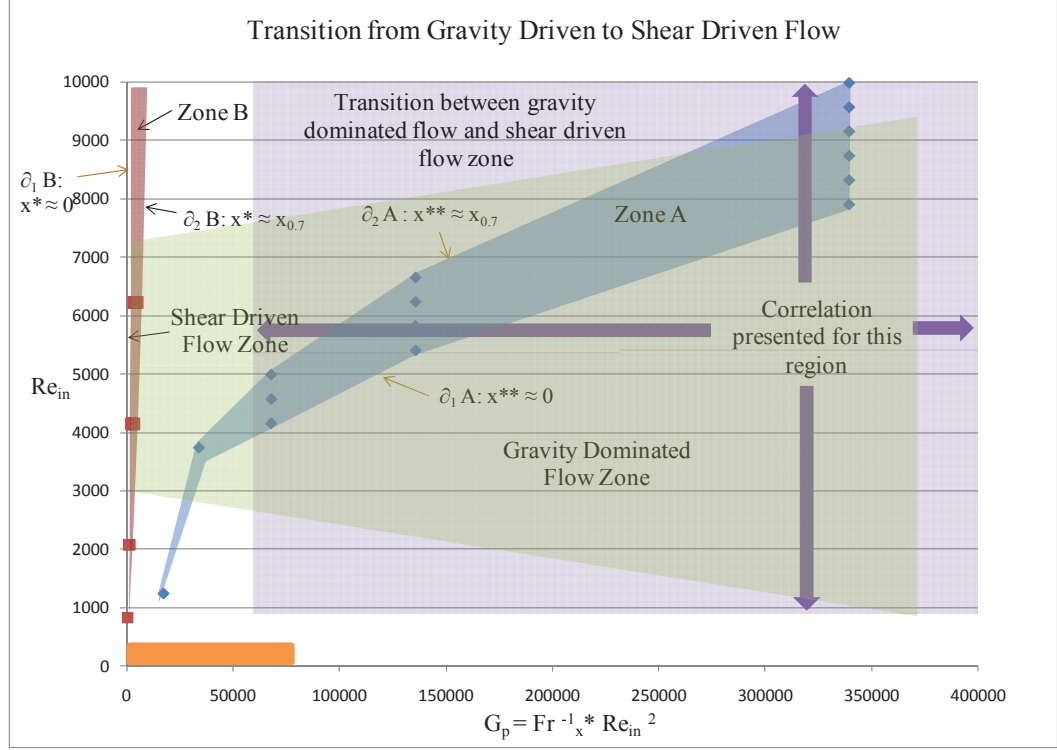


Figure 5.5: The figure is a projection of Fig. 5.2 in $(Re_{in} - G_p)$ plane and it also marks a gravity dominated zone, a shear dominated zone, and a transition zone between them.

The map in Fig. 5.2 is obtained by: (i) first selecting representative values of $Ja/Pr_1 = 0.004$, $\rho_2/\rho_1 = 0.0148$, and $\mu_2/\mu_1 = 0.0241$ which is within the cubical neighborhood of $(Ja/Pr_1, \rho_2/\rho_1, \mu_2/\mu_1)$ given in Eq. (5.3), and (ii) by considering transitions between entirely gravity and entirely shear driven flows in the three-dimensional (x, Re_{in}, G_p) space. In this space, a solution for $0g$ ($G_p = 0$), under pure shear conditions, has a non-dimensional film thickness profile, denoted as $\delta_{ps}(x)$. A representative profile of $\delta_{ps}(x)$ along with a 4% neighborhood (shown by dotted lines) is shown in Fig. 5.3. When the gravity parameter G_p is gradually increased to non-zero positive values (this could happen by allowing gravity vector in Fig. 2.2 to become non-zero or by inclining the horizontal channel in Fig. 2.1), it is found that over a certain downstream distance $x > x^*$,

the shear driven flow starts exhibiting a departure greater than 4% from the $G_p = 0$ case. Typically, this x^* value reduces as G_p increases. This x^* , when plotted as $x^* = x^*(Re_{in}, G_p)$, yields the surface Σ_1 in Fig. 5.2. The curves bounding the surface Σ_1 in Fig. 5.2 arise from the constraints $0 < x^* \leq x_{0.7}$ and $0 \leq Re_{in} \leq 7000$.

A representative profile of $\delta_{Nu}(x)$ in Eq. (5.1) along with a 4% neighborhood (shown by dotted lines) is shown in Fig. 5.4. If the parameters are such that the flow's film thickness predictions are within this neighborhood, the flow is said to be gravity dominated or entirely gravity driven. If for any given parameter set in the gravity dominated region, G_p is reduced or Re_{in} is increased, a point x^{**} appears near the inlet in Fig. 5.4 and is marked by the fact that the effects of shear in the region $0 \leq x \leq x^{**}$ causes a departure greater than 4% from the $\delta_{Nu}(x)$ behavior. This x^{**} increases as G_p is further reduced (or Re_{in} is further increased). This x^{**} , when plotted as $x^{**} = x^{**}(Re_{in}, G_p)$, yields the surface Σ_2 in Fig. 5.2. The curves bounding the surface Σ_2 in Fig. 5.2 arise from the constraint $0 < x^{**} \leq x_{0.7}$ and $0 \leq Re_{in} \leq 10000$.

Therefore, in the shear driven flow zone (left of surface Σ_1 in Fig. 5.2 or left of its projection – termed *zone B* - in Fig. 5.5), where $\delta(x) \approx \delta_{ps}(x)$, the following equation is satisfied:

$$\text{for } 0 < x < x_{0.7}, \quad \left| \frac{\delta(x) - \delta_{ps}(x)}{\delta_{ps}(x)} \right| < 0.04. \quad (5.4)$$

Similarly, in the gravity dominated flow zone (right of surface Σ_2 in Fig. 5.2 or right of its projection – termed *zone A* – in Fig. 5.5), where $\delta(x) \approx \delta_{Nu}(x)$, the following equation is satisfied:

$$\text{for } 0 < x < x_{0.7}, \quad \left| \frac{\delta(x) - \delta_{Nu}(x)}{\delta_{Nu}(x)} \right| < 0.04 \quad (5.5)$$

As shown in Fig. 5.2, operating conditions on surface Σ_1 itself (i.e. *zone B* in Fig. 5.5) are such that, over the leading part ($0 < x < x^*$), the condensate film is affected by shear whereas, over the aft portion ($x^* < x < x_{0.7}$), gravity effects start playing a role. Thus for these operating conditions, the following conditions hold:

$$\begin{aligned} &\text{for } 0 < x < x^*, \quad \left| \frac{\delta(x) - \delta_{ps}(x)}{\delta_{ps}(x)} \right| < 0.04 \\ &\text{while for } x^* < x < x_{0.7}, \quad \left| \frac{\delta(x) - \delta_{ps}(x)}{\delta_{ps}(x)} \right| \geq 0.04 \end{aligned} \quad (5.6)$$

Similarly for operating conditions on surface Σ_2 (i.e. *zone A* in Fig. 5.5) are such that, over the leading part ($0 < x < x^{**}$), the condensate film is affected by shear whereas, over the aft portion ($x^{**} < x < x_{0.7}$), gravity effects remain dominant. Thus for these operating conditions, the following criteria hold:

$$\begin{aligned} &\text{for } 0 < x < x^{**}, \quad \left| \frac{\delta(x) - \delta_{Nu}(x)}{\delta_{Nu}(x)} \right| > 0.04 \\ &\text{while for } x^{**} < x < x_{0.7}, \quad \left| \frac{\delta(x) - \delta_{Nu}(x)}{\delta_{Nu}(x)} \right| \leq 0.04 \end{aligned} \quad (5.7)$$

The region between surfaces Σ_1 and Σ_2 in Fig. 5.2 (i.e. between *zone A* and *zone B* in Fig. 5.5) define “mixed” driven flows for which both shear and gravity are important to varying degrees. This transitional zone is characterized by the set of following two equations that hold for all x ($0 < x < x_{0.7}$):

$$\left| \frac{\delta(x) - \delta_{Nu}(x)}{\delta_{Nu}(x)} \right| > 0.04 \quad \text{and} \quad \left| \frac{\delta(x) - \delta_{ps}(x)}{\delta_{ps}(x)} \right| > 0.04 \quad (5.8)$$

Recall that $\delta_{ps}(x)$ is the film thickness obtained for the purely shear driven flows under zero gravity conditions. These $\delta_{ps}(x)$ values for the internal condensing flows in the annular/stratified regime can be correlated and are useful. A computationally obtained

correlation of the solutions obtained from the 1-D approach for $Fr_x^{-1} = 0$ (i.e. $G_p = 0$) while the remaining non-dimensional parameters continue to be in the range given in Eq. (5.3). The correlations are within 8% of the numerical solutions for the film thickness $\delta_{ps}(x)$ (or for the local heat transfer coefficient h_x through $Nu_x \equiv h_x \cdot L_c / k \approx 1/\delta(x)$) and the point of 75% condensation (i.e. $x = x_{0.75}$). They are given as:

$$\delta_{ps}(x) = \frac{0.7487 * X^{0.35} * (Ja/Pr_1)^{0.3611} * (\rho_2/\rho_1)^{0.2380}}{Re_{in}^{0.3529} * (\mu_2/\mu_1)^{0.5947}} \quad (5.9)$$

$$x_{0.75} = \frac{0.0447 * Re_{in} * (\rho_2/\rho_1)^{0.43} * (\mu_2/\mu_1)^{0.49}}{(Ja/Pr_1)^{0.9}}$$

Even though the impact of the temperature difference variable ΔT (i.e. its non-dimensional form Ja/Pr_1) on the surface Σ_1 and Σ_2 is important, it is not clearly depicted through Fig. 5.2 (because it is for a specific value of ΔT). Thus, we project Fig. 5.2 on $Re_{in} - G_p$ plane and obtain Fig. 5.5. For each Ja/Pr_1 , we take the left most line of Zone-B and right most line of Zone-A in Fig. 5.5 (which are, respectively, projections of Σ_1 and Σ_2 of Fig. 5.2) and then, using these lines, construct the surfaces Σ_S and Σ_G in the $(Re_{in}, G_p, Ja/Pr_1)$ space. This is done and shown in Fig. 5.6.

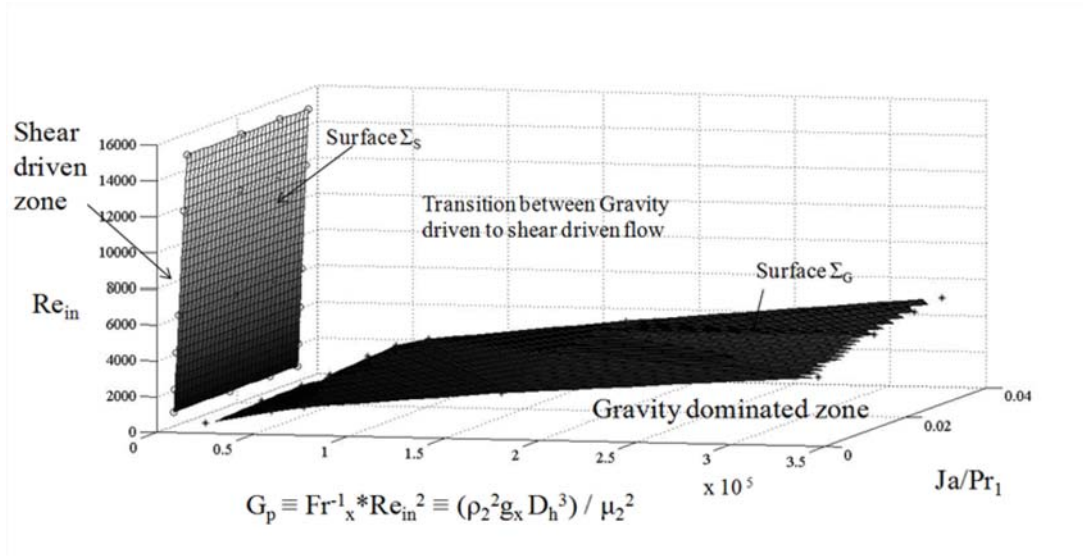


Figure 5.6: The figure suggests the boundaries in $(Ja/Pr_1, Re_{in}, G_p)$ space that marks a gravity dominated zone, a shear dominated zone, and a transition zones between them. The flow of FC-72 vapor has $(\rho_2/\rho_1) = 0.0148$ and $(\mu_2/\mu_1) = 0.0241$.

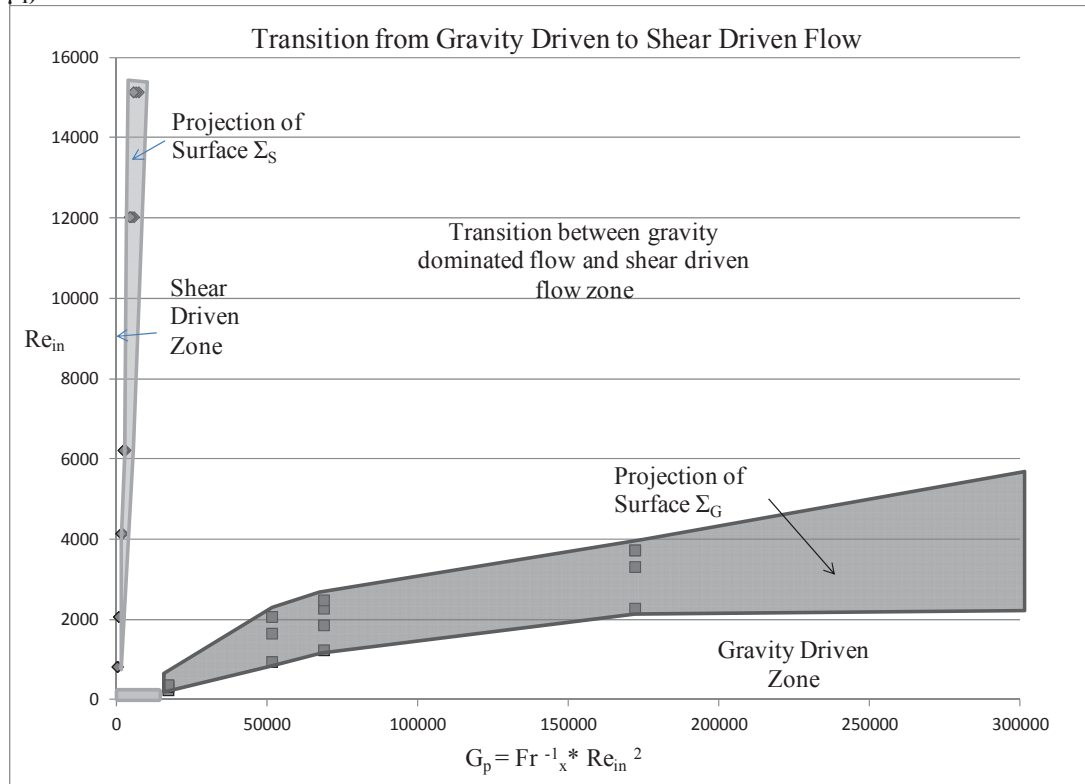


Figure 5.7: The figure is a projection of Fig. 5.6 in $(Re_{in} - G_p)$ plane.

Now Fig. 5.6 shows that, for any given fluid (ρ_2/ρ_1 and μ_2/μ_1 values) one can think of the “narrow” region to the left of Σ_S as the region for which the flow is shear driven at all x , Re_{in} , and Ja/Pr_1 of interest. Similarly, one can think of the “large” region to the right of Σ_G in Fig. 5.6 as the region for which the flow is “gravity dominated” at all x , Re_{in} , and Ja/Pr_1 of interest. To better understand the impact of the temperature difference ΔT (i.e. Ja/Pr_1) on the curvature of the surfaces Σ_S and Σ_G of Fig. 5.6, the surfaces’ projections on Re_{in} - G_p plane is shown in Fig. 5.7. The above described transition maps for annular flows significantly enhance similar investigative interests of Chen et al. 1987.

As the experimental/computational knowledge of the actual parametric boundaries for realizing annular/stratified flows become available through further research, the transition maps for annular/stratified flows shown in Fig. 5.6 can incorporate and show these boundaries. Furthermore, such maps can then be presented in a fashion that these graphical results can be generated for a range of (ρ_2/ρ_1 , μ_2/μ_1) values of interest to the user. After the flows’ sensitivities are better understood, a more general purpose correlation for the “mixed” driven flow region can also be proposed.

5.1 Summarized Correlations

For “near interface” laminar conditions in the vapor and the liquid, the modeling presented here is adequate, provided the wave amplitudes are not significant, the annular flows are stable and experimentally realized in a way that is cognizant of these flows’ different sensitivities to imposed fluctuations, etc. For a quick estimate of the key trends for such quasi-steady annular flows, following correlations are recommended:

- (i) For purely shear driven flows (left of Σ_1 in Fig. 5.2 or left of Σ_S in Fig. 5.7), the recommendation for heat transfer coefficient h_x is:

$$Nu_x = \frac{h_x L_c}{k_1} = \frac{1}{\delta_{ps}(x)}, \quad (5.10)$$

where $\delta_{ps}(x)$ and $x_{0.75}$ are given by Eq. (5.9).

- (ii) For gravity dominated flows (right of Σ_2 in Fig. 5.2 or right of Σ_G in Fig. 5.7), the definition for heat transfer coefficient h_x in Eq. (5.10) remains the same, except that $\delta_{ps}(x)$ is replaced by $\delta_{Nu}(x)$ given by the Nusselt correlation in Eq. (5.1).

- (iii) For a “mixed” driven annular flow marked by the purple shaded domain in Fig. 5.5 (which is mostly gravity dominated), the heat transfer coefficient h_x (in $Nu_x \equiv (h_x L_c / k_1) = 1/\delta(x)$) and $x_{0.75}$ can be obtained from:

$$\delta(x) = \frac{15.93 * x^{0.26} * (Ja_1 / Pr_1)^{0.2684} * (\rho_2 / \rho_1)^{0.8065}}{Re_{in}^{0.8056} * (\mu_2 / \mu_1)^{0.8426} * (Fr_x^{-1})^{0.3891}} \quad (5.11)$$

$$x_{0.75} = \frac{2.69 * Re_{in}^{0.1826} * (\rho_2 / \rho_1)^{1.1695} * (\mu_2 / \mu_1)^{0.1085}}{(Ja_1 / Pr_1)^{0.9911} * (Fr_x^{-1})^{0.5334}}$$

Better correlations for this “mixed” driven flow is possible but is not attempted here.

6. Computational results for condensing flows in micrometer scale ducts

Purely shear driven flows may occur in μm -scale (or large) hydraulic diameter D_h ducts regardless of the duct's orientation with respect to the gravity vector as shown in Mitra 2011⁹. This is because, as hydraulic diameter D_h decreases, shear and pressure forces per unit volume starts increasing and, at some low enough value of D_h , they dominate the gravitational forces per unit volume.

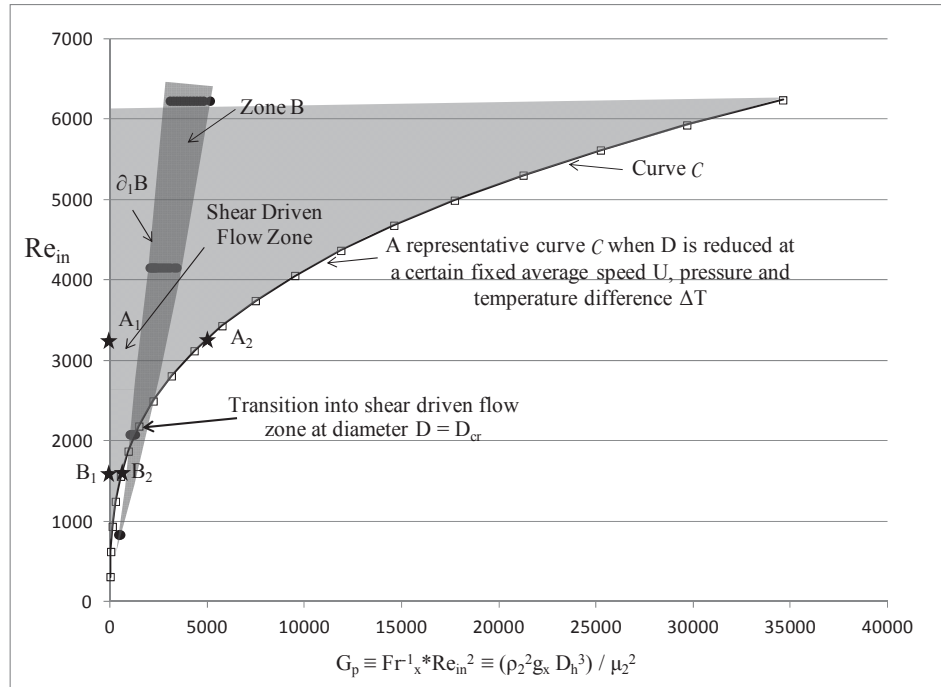


Figure 6.1: For the same inlet speed U and gravity (g_x), as tube diameter $D \rightarrow 0$, the parameter Re_{in} and G_p vary along the representative curve C . The curve C intersects zone B of Fig. 5.5 when a certain diameter D_{cr} is reached.

⁹ Some parts of the paper have been reproduced in this chapter by kind permission of Elsevier. The copyright permission is attached as separate document.

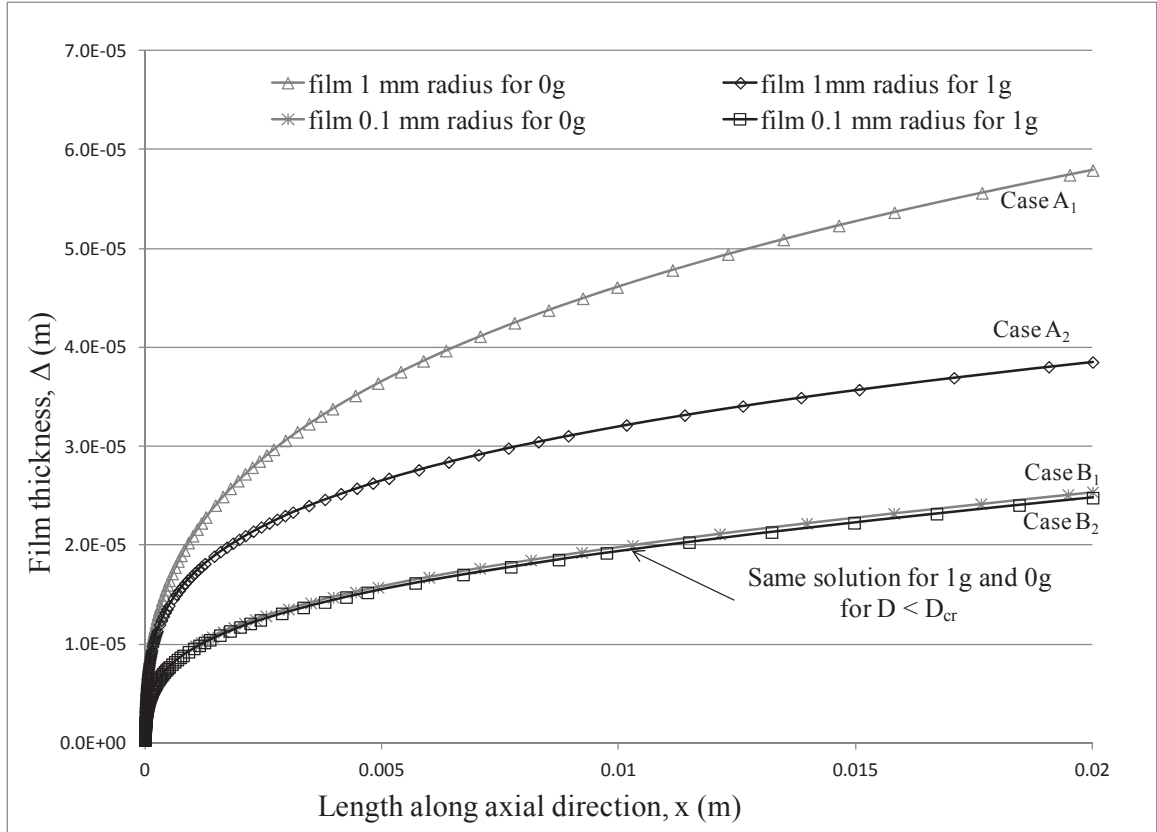


Figure 6.2: For the flow of FC-72 vapor with $U = 3$ m/s and $\Delta T = 3$ °C, the figure shows solutions for 1g and 0g cases for diameter $D_1 = 2$ mm and $D_2 = 0.2$ mm. For $D_1 > D_{cr}$ (≈ 0.3 mm), the figure shows two distinct solutions for 1g and 0g cases. For $D_2 < D_{cr}$ (≈ 0.3 mm), the solutions for both 1g and 0g cases are seen to have become nearly identical.

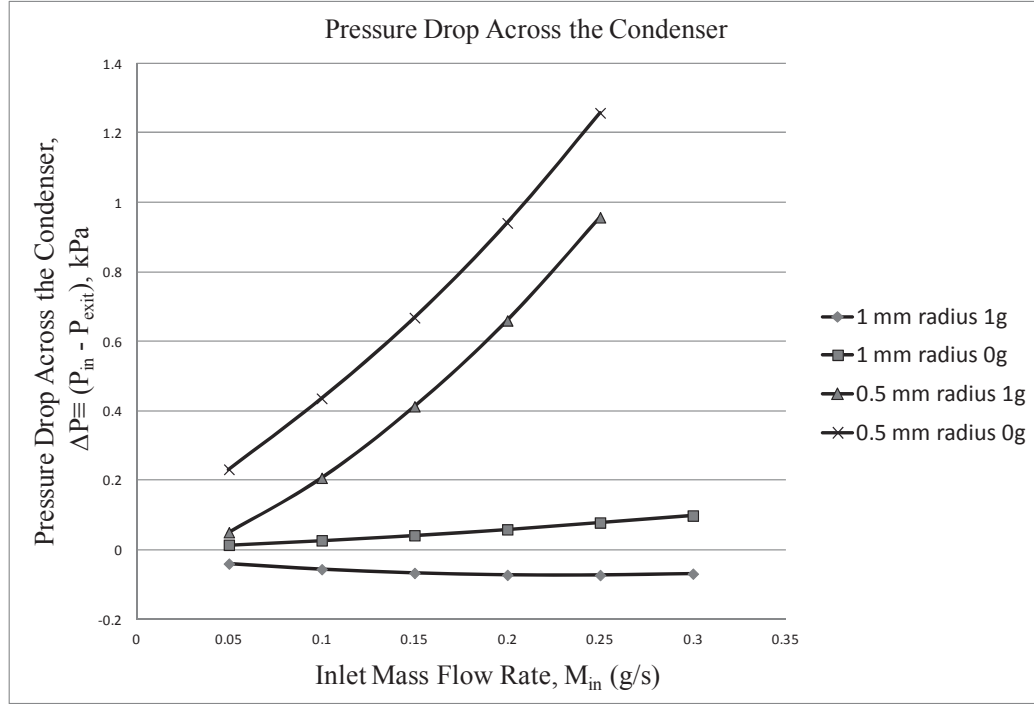


Figure 6.3: As the tube diameter becomes sub mm- to μm -scale, the figure shows (for the FC-72 flow in Fig. 6.2) a significant rise in pressure drop ($\Delta P = P_{in} - P_{exit}$) across the condenser. The pressure drop also increases with increase in inlet mass flow rates M_{in} .

Consider, in Fig. 6.1, a Re_{in} - G_p projection of a three dimensional result of the type shown in Fig. 5.2. If one reduces the tube diameter D by letting $D \rightarrow 0$ – while average vapor inlet speed U , gravity level g_x , and ΔT are held constant – an arbitrary point A_2 moves along the curve C in Fig. 6.1 to point B_2 . At sufficiently small diameter $D = D_{cr}$, the pure shear boundary zone B (of Fig. 5.5) is fully crossed for the Ja/Pr_1 value under consideration. This is illustrated by the fact that, for point A_2 in Fig. 6.1 (which marks a 1g situation for a vertical tube of diameter D), the corresponding 0g situation is point A_1 . Since $D > D_{cr}$ associated with the transition to shear driven flows, the 1g (A_2) and 0g (A_1)

flows are quite different. This difference is clearly seen through film thickness simulation results (shown in Fig. 6.2) for point A₁ and A₂. However, for cases marked by points B₁ and B₂ in Fig. 6.1, the 1g point B₂ has a corresponding 0g point B₁. Since both these flows are for diameters of the tube $D \leq D_{cr}$, the simulation results for these flows are nearly identical (again see Fig. 6.2) as both the flows have a gravitational parameter which is at or near zero and condensate flow is shear driven in nature. As a result, one finds that for $D < D_{cr}$ (which is nearly equal to 0.3 mm and could be in μm range if a different curve C was chosen for a different U and ΔT), the flow becomes shear driven (see Fig. 6.1). Despite this, for this gravity insensitive behavior there may often be a serious penalty of large pressure drops (see Fig. 6.3) and high pumping powers across the length of such mm- or μm -scale condensers. However if a designer of a two-phase thermal system for an aircraft chooses the tube diameter D_{cr} and its operating conditions properly (e.g. in the region left of zone B in Fig. 6.1), the condenser performance could be both acceptable as well as gravity-insensitive.

As a result of significant changes in pressure drop values (Fig. 6.3) along with the changes in the other flow features, it should be noted that some new issues – that are ignored in the proposed theory - have become important for these “ $D < D_{cr}$ ” μm -scale flows. These new issues are: (i) variations in interfacial saturation temperature $T_{sat}(p_2^i)$ may become non-negligible as variations in interfacial pressure p_2^i have become significant, (ii) vapor’s density variation (compressibility) became important because of the large pressure drop, (iii) liquid-vapor surface tension effects may become important because of the large curvature at the interface (as one of the radii of the curvature is of the same order of magnitude as $D_{cr}/2$), and (iv) liquid-solid surface energy issues

(“disjoining pressure,” etc.) may become important over a certain range of film thickness values depicted in Fig. 6.2. The last liquid-solid surface energy issue may not be important for most other micro-scale flows of interest. For example, if $D \leq 0.3$ mm, the film thickness variations in Fig. 6.2 where disjoining pressure may be important corresponds to approximate locations $0 \leq x \leq 0.02$ m where $10 \text{ nm} \leq \delta \leq 20 \text{ nm}$.

The above issues are important for flows in the micro-meter range, hence, the 2-D computational tool will be modified in the future to incorporate the disjoining pressure, compressibility, and $T_{\text{sat}}(p_2^i)$ variations.

7. Conclusions and future research

7.1 Conclusions

1. An effective 1-D theoretical/computational approach has been presented for solving a class of annular in-tube and in-channel condensing flows for different thermal boundary conditions.
2. A 2-D computational solution technique for the steady governing equations of the internal condensing flows (utilizing COMSOL and MATLAB) has been presented. The computational tool has also been extended to solve transient internal condensing flow problems.
3. The computational tools developed for this dissertation are also compared with the earlier 2-D computational tool implemented on FORTRAN and the results from all three computational tools are shown to be consistent with one another.
4. The results obtained using the 1-D and 2-D computational tools are synthesized with the experimental results obtained for gravity driven flows in vertical tube Kurita et al. 2011 and inclined channels Lu et al. 1995; and for shear/pressure driven flows in horizontal channels Gorgitrattanagul 2011.
5. Computational results presented here also highlight the significant differences between steady gravity driven and steady shear driven annular flows as far as flow features are concerned.
6. The results regarding the transition maps (which are helpful in ascertaining whether the annular flow is entirely gravity driven, purely shear driven or mixed) are very useful for ascertaining transition between gravity and shear driven annular stratified flows. These transition maps are presented for a large range of

parameters and this should be useful for estimates in the design of certain experiments and applications. The maps also highlight the need for presenting the boundary of the annular flow regimes within the context of the non-dimensional parameters considered here.

7. For condensers in the mm-scale range, the zones shown in Fig. 5.2 and correlations in Eqs. (5.9) and (5.11) should be considered reliable and representative of other correlations that can be developed by the method given here.
8. The shear/pressure driven or 0g correlation in Eq. (5.9) for annular/stratified flows (zone to the left of surface Σ_s in Fig. 5.5) is an important quantitative result for design and operation of condensers in space. However, such shear driven flows are much more geometry dependent than the gravity driven flows. The quantitative uniqueness and attainability of shear driven flows, along with various sensitivities of these flows have been demonstrated through experiments in Kivisalu et al. 2011. These results are important for effective use of condensers in space-based or μm -scale applications.
9. The solutions for the shear driven flow highlights the differences between the 0g flows and the flows in the presence of transverse gravity. Theoretically feasible lengths of annular flows have been investigated with the help of the steady full 2-D simulation tool. Comparison of flow features near the zone of non-annularity for shear/pressure driven flows and gravity driven flows show that it is more difficult to make gravity driven flows non-annular.

7.2 Recommendations for Ongoing/Future work:

Condensing flow problems to be investigated in the future

Considering the development of the new computational tool, the following flow problems related to this thesis need to be further investigated with the help of a new tool:

- (i) An investigation of the length of annularity through unsteady 2-D computational tool is currently being done by R. R. Naik for his PhD thesis. The unsteady 2-D computational tool that will yield these results is already established. For a range of operating parameters, the length of annularity will be characterized, possibly with a non-dimensional parameter space.
- (ii) Unsteady tool needs to be used to study the internal condensing flows in micro-scale ducts. The impact of surface tension, disjoining pressures, and thermal non-equilibrium need to be studied for the flow in micro-scale ducts.
- (iii) It has been shown in Kivisalu et al. 2011 that, in the presence of large fluctuations in the mass flow rates, large heat flux enhancements are observed. One of the possible explanations of this phenomenon is the interaction of the transient compressibility effects with the interfacial waves. It will be important to investigate the impact of compressibility on the condensing flows.
- (iv) The tool presented here should be amenable to modifications that include the impact of vapor turbulence in the region away from the interface. This modeling may be important for better estimates of the pressure-difference over the annular zone.
- (v) The 1-D tool has already been used to investigate flow boiling in tube and channel geometry. This engineering simulation technique should be extended to a full 2-D

CFD simulation on the COMSOL/MATLAB platform for investigation of length of annular flow boiling, impact of noise, and fluctuation sensitivities.

- (vi) Subsequently, analogous to this dissertation, synthesis between computational and experimental results for annular boiling flows needs to be achieved.

7.3 Aiding thermal system development

To assist in developing a robust and reliable thermal system, two predictive tools have been presented, validated and established. With further development of the unsteady simulation tool and the proposed *annular flow boiling* simulation tool, a complete flow loop can be modeled. With the help of such tools, boundary condition sensitivities should be investigated for flow condensation and flow boiling - specially for shear/pressure driven flows. After synthesizing these results for flow boiling and flow condensation, system level analysis can be undertaken to design novel thermal system. Our research group at MTU is planning to propose such a thermal system. Design and development of such a system will immensely benefit from the proposed correlations and transition maps.

References

- A. Narain, M. Kivisalu, R. Naik, N. Gorgitrattanagul, Mitra S and Hasan MM 2012. Comparative Experimental and Computational Studies for Annular Condensing and Boiling Flows in Millimeter Scale Horizontal Ducts. Submitted to Proceedings of the ASME 2012 Summer Heat Transfer Conference, Rio Grande, Puerto Rico.
- Arnold VI 1973. Ordinary differential equations. Cambridge,, MIT Press.
- Carey VP 2008. Liquid-vapor phase-change phenomena : an introduction to the thermophysics of vaporization and condensation processes in heat transfer equipment. New York, Taylor and Francis.
- Carpenter FG and Colburn AP 1951. The Effect of Vapor Velocity on Condensation Inside Tubes. Proceedings of the General Discussion of Heat Transfer ASME: 20-26.
- Cavallini A, Censi G, Del Col D, Doretti L, Longo GA, Rossetto L and Zilio C 2003. Condensation inside and outside smooth and enhanced tubes - a review of recent research. International Journal of Refrigeration-Revue Internationale Du Froid 26(4): 373-392.
- Chen MM 1961. An Analytical Study of Laminar Film Condensation: Part 1 Flat Plate. Journal of Heat Transfer-Transactions of the Asme 83: 48-54.
- Chen SL, Gerner FM and Tien CL 1987. General Film Condensation Correlations. Experimental Heat Transfer 1(2): 93-107.
- Chen Y, Li X, Wu J and Shi M 2009. One dimensional numerical simulation for steady annular condensation flow in rectangular microchannels. Heat and Mass Transfer 46(1): 75-82.
- Delhay JM 1974. Jump Conditions and Entropy Sources in Two-phase Systems; Local Instant Formulation. International Journal of Multiphase Flow 1: 395-409.
- Dobran F and Thorsen RS 1980. Forced Flow Laminar Filmwise Condensation of a Pure Saturated Vapor in a Vertical Tube. International Journal of Heat and Mass Transfer 23(2): 161-177.
- Gorgitrattanagul N 2011. The Length of the Annular Regime for Condensing Flows Inside a Horizontal Channel - the Experimental Determination of its Values and its Trends. Mechanical Engineering and Engineering Mechanics. Houghton, MI, Michigan Technological University. MS
- Greenberg MD 1978. Foundations of applied mathematics. Englewood Cliffs, N.J., Prentice-Hall.
- Incropera FP and DeWitt DP 2002. Fundamentals of heat and mass transfer. New York, J. Wiley.
- Kivisalu M, Gorgitrattanagul N, Mitra S, Naik R and Narain A 2011. Shear/Pressure Driven Internal Condensing Flows and their Sensitivity to Inlet Pressure Fluctuations. Proceedings of IMECE 2011 ASME International Mechanical Engineering Congress and Exposition, Denver, Colorado, USA.
- Kivisalu M, Gorgitrattanagul P, Mitra S, Naik R and Narain A 2011. Prediction and Control of Internal Condensing Flows in the Experimental Context of their Inlet Condition Sensitivities. Microgravity Science and Technology: 1-9.

- Koh JCY 1962. Film Condensation in a Forced-Convection Boundary-Layer Flow. *International Journal of Heat and Mass Transfer* 5: 941-954.
- Kulkarni S, Narain A and Mitra S 2010. Forced Flow of Vapor Condensing Over a Horizontal Plate (Problem of Cess and Koh): Steady and Unsteady Solutions of the Full 2D Problem. *Journal of Heat Transfer-Transactions of the Asme* 132(10).
- Kurita J, Kivisalu M, Mitra S, Naik R and Narain A 2011. Experimental results on gravity driven fully condensing flows in vertical tubes, their agreement with theory, and their differences with shear driven flows' boundary-condition sensitivities. *International Journal of Heat and Mass Transfer* 54(13-14): 2932-2951.
- Labuntsov DA 1957. Heat Transfer in Film Condensation of Pure Steam on Vertical Surfaces and Horizontal Tubes. *Teploenergetica* 4.
- Lasance CJM and Simons RE 2005 "Advances In High-Performance Cooling for Electronics." *Electronics Cooling* 11.
- Liang Q, Wang X and Narain A 2004. Effects of gravity, shear and surface tension in internal condensing flows: Results from direct computational simulations. *Journal of Heat Transfer-Transactions of the Asme* 126(5): 676-686.
- Lu Q and Suryanarayana NV 1995. CONDENSATION OF A VAPOR FLOWING INSIDE A HORIZONTAL RECTANGULAR DUCT. *Journal of Heat Transfer-Transactions of the Asme* 117(2): 418-424.
- Mitra S, Naik R and Narain A 2011. Numerical Simulation of Exact Two-Dimensional Governing Equations for Internal Condensing Flows. *COMSOL Conference 2010, Boston*.
- Mitra S, Narain A, Kulkarni S, Naik R and Kurita J 2009. Annular/Stratified Internal Condensing Flows in Millimeter to Micrometer Scale Ducts. *ASME Conference Proceedings 2009(43901)*: 155-170.
- Mitra S, Narain A, Naik R and Kulkarni SD 2011. A quasi one-dimensional method and results for steady annular/stratified shear and gravity driven condensing flows. *International Journal of Heat and Mass Transfer* 54(15-16): 3761-3776.
- Modeling_Guide Deformed Meshes. *COMSOL MULTIPHYSICS by COMSOL Inc. Chapter 14*: 392-432.
- Mukherjee A and Dhir VK 2004. Study of lateral merger of vapor during nucleate pool boiling. *Journal of Heat Transfer-Transactions of the Asme* 126(6): 1023-1039.
- Narain A 1996. Modeling of interfacial shear for gas liquid flows in annular film condensation. *Journal of Applied Mechanics-Transactions of the Asme* 63(2): 529-538.
- Narain A, Kulkarni S, Kivisalu M, Kurita JH and Mitra S 2008. New Experimental and Computational Results for Macro - and Micro-Scale Internal Condensing Flows. *ECI International Conference on Heat Transfer and Fluid Flow in Microscale*.
- Narain A, Kulkarni S, Mitra S, Kurita JH and Kivisalu MT 2009. Computational and Ground-Based Experimental Investigations of the Effects of Specified and Unspecified (Free) Pressure Conditions at the Condenser Exit for Condensing Flows in Terrestrial and Microgravity Environments. *Interdisciplinary Transport Phenomena: Fluid, Thermal, Biological, Materials, and Space Sciences*. S. S. Sadhal. Oxford, Blackwell Publishing. 1161: 321-360.

- Narain A, Kulkarni S, Mitra S, Kurita JH and Kivisalu MT 2009. Computational and Ground-Based Experimental Investigations of the Effects of Specified and Unspecified (Free) Pressure Conditions at the Condenser Exit for Condensing Flows in Terrestrial and Microgravity Environments. *Interdisciplinary Transport Phenomena: Fluid, Thermal, Biological, Materials, and Space Sciences* 1161: 321-360.
- Narain A, Kurita JH, Kivisalu M, Siemionko A, Kulkarni S, Ng TW, Kim N and Phan L 2007. Internal condensing flows inside a vertical pipe: Experimental/computational investigations of the effects of specified and unspecified (Free) conditions at exit. *Journal of Heat Transfer-Transactions of the Asme* 129(10): 1352-1372.
- Narain A, Liang Q, Yu G and Wang X 2004. Direct computational simulations for internal condensing flows and results on attainability/stability of steady solutions, their intrinsic waviness, and their noise sensitivity. *Journal of Applied Mechanics-Transactions of the Asme* 71(1): 69-88.
- Narain A, Phan LA, Wang XM, Kurita JH, Siemionko A, Ng TW and Kulkarni SD 2006. Direct computational simulations and experiments for film condensation inside tubes and channels. *Interdisciplinary Transport Phenomena in the Space Sciences* 1077: 471-507.
- Nook G 2011. The Length of the Annular Regime for Condensing Flows Inside a Horizontal Channel - the Experimental Determination of its Values and its Trends. *Mechanical Engineering and Engineering Mechanics*. Houghton, MI, Michigan Technological University. MS
- Nusselt W 1916. Die Oberflächenkondensation des Wasserdampfes. *Z. Ver. Dt. Ing.* 60(27): 541-546.
- Osher S and Fedkiw RP 2003. *Level set methods and dynamic implicit surfaces*. New York, Springer.
- Patankar SV 1980. *Numerical heat transfer and fluid flow*. Washington, New York, Hemisphere Pub. Corp. , McGraw-Hill.
- Phan L and Narain A 2007. Nonlinear stability of the classical Nusselt problem of film condensation and wave effects. *Journal of Applied Mechanics-Transactions of the Asme* 74(2): 279-290.
- Phan L, Wang X and Narain A 2006. Effects of exit-condition, gravity, and surface-tension on stability and noise-sensitivity issues for steady condensing flows inside tubes and channels. *International Journal of Heat and Mass Transfer* 49(13-14): 2058-2076.
- Plesset MS and Prosperetti A 1978. Contribution of Latent Heat-Transport in Subcooled Nucleate Boiling. *International Journal of Heat and Mass Transfer* 21(6): 725-734.
- Rohsenow WM 1956. Heat Transfer and Temperature Distribution in Laminar Film Condensation. *Transactions ASME* 78: 1645-1648.
- Rose JW 1998. *Condensation heat transfer fundamentals*. Chemical Engineering Research & Design 76(A2): 143-152.
- Schlichting H and Gersten K 2000. *Boundary-layer theory*. Berlin ; New York, Springer.

- Shah MM 1979. A General Correlation for Heat Transfer during Film Condensation inside Pipes. *International Journal of Heat and Mass Transfer* 22: 547-556.
- Shekrila.I and Mestviri.S 1973. High-Rate Condensation Process Theory of Vapor Flow inside a Vertical Cylinder. *International Journal of Heat and Mass Transfer* 16(4): 715-724.
- Son G and Dhir VK 1998. Numerical simulation of film boiling near critical pressures with a level set method. *Journal of Heat Transfer-Transactions of the Asme* 120(1): 183-192.
- Sparrow EM and Gregg JL 1959. A Boundary Layer Treatment of Laminar Film Condensation. *ASME Journal of. Heat Transfer* 81: 13-18.
- Sussman M, Smereka P and Osher S 1994. A Level Set Approach for Computing Solutions to Incompressible 2-Phase Flow. *Journal of Computational Physics* 114(1): 146-159.
- Wedekind GL, Beck BT, Bhatt BL and Roslund GL 1989. Uniqueness of System Response Time for Transient Condensing Flows. *Journal of Heat Transfer-Transactions of the Asme* 111(1-4): 1126-1129.
- Wedekind GL and Bhatt BL 1989. Modeling the Thermally Governed Transient Flow Surges in Multitube Condensing Flow Systems With Thermal and Flow Distribution Asymmetry. *Journal of Heat Transfer-Transactions of the Asme* 111(1-4): 786-791.
- Wilson JR 2009 "Electronics Cooling Depends on Innovative Approaches to Thermal Management." *Military & Aerospace Electronics*.

Appendix A1 - Definition of coefficients for 1-D internal condensing flow

Definition of coefficients for 1-D internal condensing flow inside a cylindrical tube:

The governing equations obtained for solving the internal condensing equations are given in Chapter 2. The governing equations for a condensing flow in a cylinder (shown in Fig. 2.2) are written in the following vector form of a coupled set of four first order non-linear ordinary differential equations:

$$\mathbf{A}_{[4 \times 4]} \frac{d\mathbf{y}}{dx} = \mathbf{g}(\mathbf{y}) \quad (\text{A.1})$$

where,

$$\mathbf{A} \equiv \begin{pmatrix} 0 & 0 & 1 & 0 \\ A_{11} & A_{12} & 0 & A_{14} \\ C_{11} & C_{12} & C_{13} & C_{14} \\ D_{11} & D_{12} & 0 & D_{14} \end{pmatrix}$$

$$\mathbf{y} \equiv \begin{pmatrix} u_m \\ \delta \\ \pi \\ \zeta \end{pmatrix} \quad \text{and} \quad \mathbf{g}(\mathbf{y}) \text{ is a known function}$$

Here,

$$\begin{aligned}
A_{11} &\equiv \frac{dI}{du_m} + \frac{\rho_2}{\rho_1} \frac{dI_1}{du_m} \\
A_{12} &\equiv \frac{dI}{d\delta} + \frac{\rho_2}{\rho_1} \frac{dI_1}{d\delta} \\
A_{14} &\equiv \frac{dI}{d\zeta} + \frac{\rho_2}{\rho_1} \frac{dI_1}{d\zeta}
\end{aligned} \tag{A.2}$$

A_{11} , A_{12} , and A_{14} arise from integral mass balance equation.

$$\begin{aligned}
C_{11} &\equiv \frac{dI_2}{du_m} \\
C_{12} &\equiv \frac{dI_2}{d\delta} \\
C_{13} &\equiv \frac{(1-2\delta)^2}{8} \\
C_{14} &\equiv \frac{dI_2}{d\zeta} \\
f_4 &\equiv \left(\frac{Fr_x^{-1}(1-2\delta)^2}{8} \right) - \left(\frac{1}{2} \frac{\mu_1}{\mu_2} \frac{1}{Re_{in}} \frac{\partial u_1}{\partial y} \Big|_i (1-2\delta) \right) - \left(\frac{1}{2} \frac{\rho_1}{\rho_2} (1-2\delta) \frac{Ja_1}{Re_1 Pr_1} \frac{u_f}{\delta} \right)
\end{aligned} \tag{A.3}$$

C_{11} , C_{12} , C_{13} , C_{14} and f_4 arise from vapor momentum balance equation.

$$\begin{aligned}
D_{11} &\equiv \frac{2}{(1-2\delta)} \frac{dI}{du_m} \\
D_{12} &\equiv \frac{2}{(1-2\delta)} \frac{dI}{d\delta} \\
D_{14} &\equiv \frac{2}{(1-2\delta)} \frac{dI}{d\zeta} \\
f_3 &\equiv \frac{Ja_1}{Re_1 Pr_1} \frac{1}{\delta}
\end{aligned} \tag{A.4}$$

D_{11} , D_{12} , D_{14} and f_3 arise from interfacial energy balance equation.

where, $I \equiv \int_{\frac{1-2\delta}{2}}^{\frac{1}{2}} u_1(x, \hat{r}) \hat{r} \cdot d\hat{r}$ and $I_2 \equiv \int_0^{\frac{1-2\delta}{2}} u_2 \hat{r} \cdot d\hat{r}$

Here, vapor velocity profile $u_2(x,y)$ is chosen as Eq. (2.25).

Definition of coefficients for 1-D internal condensing flow inside a cylindrical tube:

The governing equations for a condensing flow in a channel (shown in Fig. 2.1) are written in the following vector form of a coupled set of four first order non-linear ordinary differential equations:

$$\mathbf{A}_{[4 \times 4]} \frac{d\mathbf{y}}{dx} = \mathbf{g}(\mathbf{y}) \quad (\text{A.5})$$

where,

$$\mathbf{A} \equiv \begin{pmatrix} 0 & 0 & 1 & 0 \\ A_{11} & A_{12} & 0 & A_{14} \\ C_{11} & C_{12} & C_{13} & C_{14} \\ D_{11} & D_{12} & 0 & D_{14} \end{pmatrix}$$

$$\mathbf{y} \equiv \begin{pmatrix} u_f \\ \delta \\ \pi \\ \zeta \end{pmatrix} \quad \text{and} \quad \mathbf{g}(\mathbf{y}) \text{ is a known function}$$

The basic definition of the coefficients in Eqs. (A.2 – A.4) remain the same, except for the terms with (d/du_m) is replaced with (d/du_f) as u_m is replaced by u_f in the vector \mathbf{y} . Similar equations are obtained and solved for the condensing flow inside a channel. Depending on the choice of $u_2(x,y)$ profile given by Eq. (2.23) and Eq. (2.24), these coefficients change. Once these coefficients are available, they are solved using Mathematica and MATLAB.

Appendix A.2 – Copyright Permission

Copyright Permission was obtained for the following three journal papers with kind permission from Elsevier and Springer Science and Business Media

1. S. Mitra, A. Narain, R. Naik, and S. D. Kulkarni “A Quasi One-Dimensional Method and Results for Steady Annular/Stratified Shear and Gravity Driven Condensing Flows,” *International Journal of Heat and Mass Transfer*, 54, 3761-3776, 2011.
2. J. H. Kurita, M. Kivisalu, S. Mitra, A. Narain, “Experimental Results on Gravity Driven Condensing Flows in Vertical Tubes, their Agreement with Theory, and their Differences with Shear Driven Flows’ Boundary Condition Sensitivities,” *International Journal of Heat and Mass Transfer*, 54, 2932-2951, 2011.
3. M. Kivisalu, N. Gorgitrattanagul, S. Mitra, R. Naik, and A. Narain, “Prediction and Control of Internal Condensing Flows in the Experimental Context of their Sensitivities,” *Microgravity Science and Technology*, pp. 1-9, 2011.

The results reproduced from these papers in this dissertation are original contribution from the author (Soumya Mitra). The copyright permissions is obtained to reproduce excerpts of text and figures in this dissertation. The copyright permissions are available on request.

Some excerpts of text and figures have been used from the following paper submitted and presented at the COMSOL conference 2010, Boston, MA. This copyright for reproducing this work lies with the author (Soumya Mitra).

4. S. Mitra, R. R. Naik, and A. Narain, “Numerical Simulation of Exact Two-Dimensional Governing Equations for Internal Condensing Flows,” COMSOL conference 2010, October 7 – 9, Boston, 2010.

The copyright agreement between the author (Soumya Mitra) and COMSOL is as follows:

Copyright notice

By submitting abstracts, full length papers, presentations, movies, model files and other materials ("Contributed Materials") through this website to COMSOL, you hereby grant COMSOL a nonexclusive, royalty-free, perpetual, worldwide, and unrestricted license to use, copy, publicly display, publicly perform, and prepare derivative works of the Contributed Materials and to distribute the Contributed Materials and derivative works thereof as part of the COMSOL Conference materials and proceedings and otherwise. Such license includes the right to reproduce the Contributed Materials and derivative works thereof in hard copy or electronic form, to archive the Contributed Materials and derivative works thereof on a COMSOL website and to publicly distribute, publicly display, and publicly perform the Contributed Materials and derivative works thereof in any manner, by any means, and through any medium now existing or hereafter coming into existence. You shall retain all ownership rights to the copyrights in the Contributed

Materials and in view of the fact that the license granted to COMSOL is nonexclusive, there are no limits on your right to publish and distribute such Contributed Materials. COMSOL agrees that it will provide attribution for all Contributed Materials to the respective authors.

Appendix A-3 of the dissertation is quoted from “Direct Computational Simulations for Internal Condensing Flows and Results on Attainability/Stability of Steady Solutions, Their Intrinsic Waviness, and Their Noise Sensitivity,” by A. Narain, Q. Liang, G. Yu, and X. Wang, Journal of Applied Mechanics, Volume 71, Issue 1, 69, Page 87, 2004” by kind permission from ASME.

The following email from ASME provides the necessary reprinting permission to reproduce the appendix from the above paper.

Dear Mr. Mitra:

It is our pleasure to grant you permission to use an **Appendix** from "Direct Computational Simulations for Internal Condensing Flows and Results on Attainability/Stability of Steady Solutions, Their Intrinsic Waviness, and Their Noise Sensitivity," by A. Narain, Q. Liang, G. Yu, and X. Wang, Journal of Applied Mechanics, Volume 71, Issue 1, 69, Page 87, 2004, as cited in your letter for inclusion in a Doctoral Thesis entitled DEVELOPMENT OF ONE-DIMENSIONAL AND TWO-DIMENSIONAL COMPUTATIONAL TOOLS THAT SIMULATE STEADY INTERNAL CONDENSING FLOWS IN TERRESTRIAL AND ZERO-GRAVITY ENVIRONMENTS to be published by Michigan Technological University.

Permission is granted for the specific use as stated herein and does not permit further use of the materials without proper authorization. Proper attribution must be made to the author(s) of the materials, and no alterations of the materials is permitted in any material manner.

As is customary, we request that you ensure full acknowledgment of this material, the author(s), source and ASME as original publisher. Acknowledgment must be retained on all pages printed and distributed.

Many thanks for your interest in ASME publications.

Sincerely,

Beth Darchi

Permissions & Copyrights

ASME, 3 Park Avenue

New York, NY 10016

T: 212-591-7700

F: 212-591-7841

E: darchib@asme.org

Appendix A.3

The following Appendix (excerpt) is included in this dissertation from Narain et al. 2004. This section is quoted from the Appendix of the paper by kind permission from ASME.

The interface conditions that apply at $\phi(x, y, t) = y - \Delta(x, t) = 0$, involve values of flow variables at the interface that are denoted by a superscript 'i'. The unit normal at any point on the interface, directed from the liquid towards the vapor, is denoted by $\hat{\mathbf{n}}$ and is equal to $\nabla\phi / |\nabla\phi|$. The unit tangent at any point on the interface, directed towards increasing x , is denoted by $\hat{\mathbf{t}}$. Each phase is modeled as a viscous and incompressible Newtonian fluid with stress tensor $\mathbf{T} = -p\mathbf{1} + \mathbf{S}$ where

$\mathbf{S} = \mu_1 \{(\text{grad} \cdot \mathbf{v}_1) + (\text{grad} \cdot \mathbf{v}_1)^T\} / 2$ and $\mathbf{1}$ is the identity tensor.

- The surface velocity \mathbf{v}_s of a point on the interface ($\phi=0$) at time t is associated with this point's movement to a new mapped position on the interface at time $t + \Delta t$. All such mappings must be such that the normal component of this \mathbf{v}_s is given by:

$$\mathbf{v}_s \cdot \hat{\mathbf{n}} = -(\partial\phi / \partial t) / |\nabla\phi|. \quad (\text{A.1})$$

- The tangential component of the vapor and liquid velocities at the interface must be continuous, i.e.

$$\mathbf{v}_1^i \cdot \hat{\mathbf{t}} = \mathbf{v}_2^i \cdot \hat{\mathbf{t}}. \quad (\text{A.2})$$

- Allowing for variations in surface tension σ over the interface such that the vector $\nabla_s \sigma$ is in the tangent plane and ignoring the normal component of viscous stresses in comparison to interfacial pressures, the normal component of momentum balance at a point on the interface is given by:

$$\begin{aligned}
p_1^i &= p_2^i + \dot{m}^2 (1/\rho_2 - 1/\rho_1) + \sigma \nabla_s \bullet \hat{\mathbf{n}} - \nabla_s \sigma \bullet \hat{\mathbf{n}} + (\mathbf{S}_1^i - \mathbf{S}_2^i) \hat{\mathbf{n}} \bullet \hat{\mathbf{n}} \\
&\cong p_2^i + \dot{m}^2 (1/\rho_2 - 1/\rho_1) - (\sigma \Delta_{\mathcal{K}}) / [1 + \Delta_{\mathcal{K}}^2]^{2/3}.
\end{aligned} \tag{A.3}$$

The symbols for the vector $\nabla_s \sigma$ and the curvature $\nabla_s \bullet \hat{\mathbf{n}}$ in the first equality of the above equation respectively denote surface-gradient operator and surface-divergence operator and their meanings are well defined in suitable differential geometry textbooks (see, e.g., Weatherburn 1930).

- The tangential component of momentum balance at any point on the interface, which allows for surface variations in the surface tension σ , reduces to:

$$\mathbf{S}_1^i \hat{\mathbf{n}} \bullet \hat{\mathbf{t}} = \mathbf{S}_2^i \hat{\mathbf{n}} \bullet \hat{\mathbf{t}} + \nabla_s \sigma \bullet \hat{\mathbf{t}}. \tag{A.4}$$

- The mass-fluxes \dot{m}_{VK} and \dot{m}_{LK} as determined by the kinematic restrictions imposed by interfacial values of vapor and liquid velocities are:

$$\dot{m}_{\text{vk}} \equiv -\rho_2 (\mathbf{v}_2^i - \mathbf{v}_s) \bullet \hat{\mathbf{n}} \quad \text{and} \quad \dot{m}_{\text{Lk}} \equiv -\rho_1 (\mathbf{v}_1^i - \mathbf{v}_s) \bullet \hat{\mathbf{n}} \tag{A.5}$$

- The energy balance at a point on the interface, with energy fluxes being relative to the interface, imposes a restriction on the interfacial mass flux \dot{m}_{Energy} , and this restriction is given by:

$$\begin{aligned}
\dot{m}_{\text{Energy}} &= \frac{1}{h_{fg}} \left[\{ \kappa_1 \nabla \mathcal{T}_1 \bullet \hat{\mathbf{n}} - \kappa_2 \nabla \mathcal{T}_2 \bullet \hat{\mathbf{n}} \} + \frac{d\sigma}{dt} \right]_s + \frac{1}{2} \dot{m} \{ |\mathbf{v}_1^i - \mathbf{v}_s|^2 - |\mathbf{v}_2^i - \mathbf{v}_s|^2 \} \\
&\quad + \{ \mathbf{S}_1^i \hat{\mathbf{n}} \bullet (\mathbf{v}_1^i - \mathbf{v}_s) - \mathbf{S}_2^i \hat{\mathbf{n}} \bullet (\mathbf{v}_2^i - \mathbf{v}_s) \} \\
&\cong \frac{1}{h_{fg}} \left[\kappa_1 \frac{\partial \mathcal{T}_1}{\partial n} \Big|_s - \kappa_2 \frac{\partial \mathcal{T}_2}{\partial n} \Big|_s \right].
\end{aligned} \tag{A.6}$$

In deriving the first equality in Eq. (A.6) above, the equality of surface energy per unit area to surface tension force per unit length is assumed as per usual assumption regarding

equilibrium interfacial thermodynamics. The symbol $\left. \frac{d\sigma}{dt} \right|_s$ denotes rate of change of surface energy per unit area per unit time and equals $\frac{\partial \sigma}{\partial t} + \mathbf{v}_s \cdot \nabla_s \sigma$. This term along with interfacial kinetic energy exchanges and exchanges associated with the workings of the normal components of the viscous stresses are considered negligible to the net interfacial heat transfer.

- Mass Balance at any point on the interface requires a single-valued interfacial mass-flux. That is:

$$\dot{m}_{LK} = \dot{m}_{VK} = \dot{m}_{\text{Energy}} \equiv \dot{m}. \quad (\text{A.7})$$

- To account for the non-equilibrium thermodynamic effects of non-zero interfacial mass flux \dot{m} , the interfacial pressures p_1^i and p_2^i along with their difference $\Delta p^i \equiv p_1^i - p_2^i$ that appear in Eq. (A.3) are additionally considered to be controlled by non-equilibrium thermodynamics and are thought as $p_1^i \equiv p_{1 \text{ n-eq}}^i(\mathcal{T}_1^i)$ and $p_2^i \equiv p_{2 \text{ n-eq}}^i(\mathcal{T}_2^i)$, where \mathcal{T}_1^i is the liquid side interfacial temperature and \mathcal{T}_2^i is the vapor side interfacial temperature. In the limit of zero mass flux \dot{m} , these thermodynamic pressures reach their equilibrium thermodynamic values and are denoted as $p_1^i \equiv p_{\text{sat}}(\mathcal{T}_1^i)$ and $p_2^i \equiv p_{\text{sat}}(\mathcal{T}_2^i)$, where p_{sat} is the inverse function of the saturation temperature $\mathcal{T}_s(p)$. Here, the non-equilibrium and equilibrium values of the interfacial pressure differences are denoted as $(\Delta p^i)_{\text{n-eq}}$ and $(\Delta p^i)_{\text{sat}}$. To allow for a temperature discontinuity (i.e. interfacial thermal resistance) across the interface, one must set $(\Delta p^i)_{\text{n-eq}}$ equal to $\Delta p^i \equiv p_1^i - p_2^i$ as obtained from Eq. (A.3), and, in addition, one must provide an *explicit* or *implicit model* for a function f of the type $(\Delta p^i)_{\text{n-eq}} = f\{(\Delta p^i)_{\text{sat}}, \dot{m}\}$, where f allows the two pressure differences to become the same

for zero mass flux \dot{m} . It is common to *model* f by considerations that involve kinetic theory of gas for the vapor phase (see, e.g., section 4.5 of Carey 2008, Plesset et al. 1978, etc.). At all points away from $x \sim 0$, the assumption that use of either $(\Delta p^i)_{n-eq}$ or $(\Delta p^i)_{sat}$ as Δp^i in Eq. (A.3) do not significantly affect the *near zero* value of $\Delta \mathcal{T}^i \equiv \mathcal{T}_s(p_2^i + \Delta p^i) - \mathcal{T}_s(p_2^i)$ is well known and well justified in the present context where interfacial thermal resistances are overshadowed by significantly larger thermal resistance of the thin condensate (see section 4.5 of Carey 2008). Furthermore, the computations in this thesis also show: (i) that the solution further downstream is not affected by the nature of the singular solution at $x \sim 0$ (where non-equilibrium thermodynamics is important), and, (ii) that the computed downstream values of $\Delta \mathcal{T}^i \equiv \mathcal{T}_s(p_2^i + \Delta p^i) - \mathcal{T}_s(p_2^i)$, where Δp^i values are obtained from Eq. (A.3), satisfy $\Delta \mathcal{T}^i \cong 0$ in the sense that $\Delta \mathcal{T}^i \ll \Delta \mathcal{T}$, where $\Delta \mathcal{T}$ is the number defined for Eq. (1). Therefore, under negligible interfacial resistance approximation, the interfacial temperature values satisfy:

$$\mathcal{T}_1^i \cong \mathcal{T}_2^i = \mathcal{T}_s(p_2^i). \quad (\text{A.8})$$

• The term $[t]$ on the right side of Eq. (2.5) is given by:

$$[t] = \left\{ \frac{\mu_2}{\mu_1} \frac{\partial v_2}{\partial x} \bigg|_i - \frac{\partial v_1}{\partial x} \bigg|_i \right\} + \frac{2\delta_x}{[1-\delta_x^2]} \left\{ \frac{\partial u_1}{\partial x} \bigg|_i - \frac{\partial v_1}{\partial y} \bigg|_i \right\} - \frac{2\delta_x}{[1-\delta_x^2]} \frac{\mu_2}{\mu_1} \left\{ \frac{\partial u_2}{\partial x} \bigg|_i - \frac{\partial v_2}{\partial y} \bigg|_i \right\} \quad (\text{A.9})$$